Design, Optimization, Construction and Test of Rare-Earth Permanent-Magnet Electrical Machines with New Topology for Wind Energy Applications

Vorgelegt von
M.Sc. Mohammad S. Widyan

von der Fakultät IV –Elektrotechnik und Informatik
der Technischen Universität Berlin
zur Erlangung des akademischen Grades

Doktor der Ingenieur
(Dr.-Ing.)

genehmigte Dissertation

Promotionsausschuss:
Vorsitzender: Prof. Dr.-Ing. R. Orglmeister
Berichter: Prof. Dr.-Ing. R. Hanitsch
Berichter: Prof. Dr.-Ing. U. Schäfer
Berichter: Prof. Dr. R. Belmans (KU Leuven)

Tag der wissenschaftliche Aussprache: 03. Juli 2006

Berlin 2006
D83

Acknowledgments

First of all, all praise and thanks are to Allah, God the Almighty, most beneficent and most merciful.

Looking back over three years of studying and doing research, I find it difficult to capture the influence that the experience has had on me in few words. The duration of my studies here contained both instances of dependency as well as moments of great personal triumph. I find my self both sad that my stay here has finished and relieved that it is finally over.

Many people have contributed to my education. I consider myself exceedingly fortunate to have had Prof. Dr.-Ing. Habil. Rolf Hanitsch thesis advisor. The perspective valuable friendly discussions and approach he brings towards research have had a deep and beneficial influence on me. Special thanks go also for providing all the required facilities at the institute for carrying out the work of this thesis. Additionally, my deep thanks to all committee members, Prof. Dr.-Ing. Uwe Schäfer and Prof. Ronnie Belmans (Katholieke University-Leuven, Belgium). Many thanks also for Prof. Dr.-Ing. Reinhold Orglmeister for having chaired the examination session.

My special thanks go to the colleagues at the institute, Dr.-Ing. G. Korouji for the finite element package help, Dip.-Ing. M. Centner and Dip.-Ing. A. Hellemann for the technical help in the laboratories.

To the colleagues at the institute workshop and in particular Mr. Juergen Federspiel, I express my special thanks for the realization of my technical desires.

Particular acknowledgments to my sponsor the Hashemite University (Jordan) for the financial support.

Thanks also go to Dr. Weissensteiner and Mrs. Schwericke for providing us with their patented generator models.

Finally, I wish to thank my family. My sisiters and brothers were always heartening and encouraging. Most of all to my parents who introduced me to science, taught me the value of the hard work and gave endless support along the way.

Berlin, July 2006

Mohammad Widyan

Design, Optimization, Construction and Test of Rare-Earth Permanent-Magnet Electrical Machines with New Topology for Wind Energy Applications

Abstract

This thesis presents design, optimization, construction and test of radial-flux low-speed rare-earth high-energy permanent-magnet (PM) electrical machines with new topology. Two of the designed machines can be used as directly driven wind energy generators.

Due to absence of the field current and field winding, permanent magnet generators exhibit high efficiency in operation, simple and robust structure in construction and high power to weight ratio. The attractiveness of the permanent magnet generators is further enhanced by the availability of high-energy permanent magnet materials like NdFeB.

Based on the equivalent magnetic circuit approach and permanent magnet load line characteristics, iterative preliminary design for the proposed generator was firstly carried out. The aim of this simple linear pre-design tool was to have an initial geometry for the detailed investigations of the finite element technique (FET) where the electromagnetic behavior of the machine was optimized. The stator of the machine was slotted. Slotted configuration was chosen as it permits lower effective air gap length and therefore thin magnets can be used. This, in fact, largely decreases the cost of active material as it is dominated by that of the magnets. However, cogging torque comes as a consequence of slots. The cogging torque of the machine was estimated using the flux-MMF technique enhanced by the FET. Cogging torque is an oscillatory torque caused by the variation of the co-energy of the permanent magnets with respect to the rotor position, resulting from the variation of the magnetic circuit seen by the magnets. It is an inherent characteristic of slotted permanent magnet machines. It should be studied and minimized in the applications where minimizing torque ripple, vibration and noise are essential requirements. The configuration of the rotor corresponding to the lowest cogging torque was adopted.

The prototype machine was constructed using novel updated high-energy permanent magnets with a remanent of 1.41T. The stator laminations of the machine were cut using laser technology methods. The slots of the machine were flat and the windings were of toroidal type (torus) with short ends. This, in turn, reduced the cost and weight of active material and improved the efficiency. The permanent magnets were rectangular blocks of NdFeB with flux concentration arrangement and magnetized tangentially on the rotor support structure. Soft magnetic material is attached to both poles of the permanent magnets, which not only produced an easy path for the flux penetration but also reduced the leakage flux and therefore a typical 'rule of thumb' value for the leakage flux coefficient was achieved. The rotor support structure of the machine was manufactured from nonmagnetic light material (Aluminum). To further reduce the total weight of the machine, longitudinal holes were excavated inside the rotor support structure.

The constructed prototype machine was tested as variable low-speed generator with different loading conditions. Good agreement between the theoretically predicted and experimentally obtained results has been achieved. The inertia of the system together with the cogging torque necessitated a peak starting torque of 64% of the rated torque. To reduce this starting torque, the slot openings were filled up with bonded soft magnetic material with a relative permeability μ_r=10. The peak value of the starting torque has been reduced to 43% of the rated torque. The cogging torque of the machine was estimated again and the performance of the slot-filled machine was studied and compared with the previous case.

The manufactured prototype machine was single phase. Three-phase is also possible. The number of phases is usually determined based on the type of the load and the rated power demand. Finite element analysis and theoretical study were carried out on two three-phase machines of the same topology. The first one is a four-pole three-slot machine and the second one is ten-pole six-slot design.

Table of contents

List of figures

List of tables

List of symbols

Latin alphabets

a	area
A_c	Cross-sectional area of the stator conductors
A_g	Rotor iron area facing the stator
A_M	Magnetic pole area
A_p	Area of the protuberance
$A_z(x, y)$	Magnitude of the magnetic vector potential as function of x and y in the z direction
B	Magnetic flux density
B_g	Air gap flux density
$(BH)_{\max}$	Maximum energy product
B_K	Magnet flux density at the KNEE point
B_M	Magnet flux density
B_r	Remanent flux density
B_{rad}	Radial component of the magnetic flux density
B_t	Tooth flux density
$B_{\tan}$	Tangential component of the magnetic flux density
B_{yoke}	Stator yoke flux density
C_p	Conversion efficiency called Betz factor
$C_{p,\max}$	Maximum conversion efficiency
C_t	Total cost of active material
D	Electric field density
D_c	Diameter of the conductor
D_t	Total diameter of the machine
$\frac{\partial}{\partial t}$	Partial differential operator with respect to time t

$\frac{\partial}{\partial x}$	Partial differential operator with respect to x
$\frac{\partial}{\partial y}$	Partial differential operator with respect to y
$\frac{\partial}{\partial \theta}$	Partial differential operator with respect to the rotor position θ
E	Electric field strength
E_{pt}	EMF per turn
E_{rms}	rms value of the induced voltage
$E_{rms,L}$	Line-line rms value of the induced voltage
F	Magnitude of the centrifugal force
f	Frequency
F_a	Armature MMF
F_c	Coercive magnetizing force
f_{LKG}	Leakage flux coefficient
F_{lower}	Centrifugal force on the lower permanent magnet
F_M	Magnet MMF
F_{upper}	Centrifugal force on the upper permanent magnet
g	Physical air gap length
g'	Effective air gap length
H	Magnetic field strength
H_c	Actual coercivity
H_{ca}	Apparent coercivity
H_K	Magnet coercivity at the KNEE point
h_{lip}	Height of the lip
H_M	Magnet magnetic strength
h_M	Height of the permanent magnet

h_{slot}	Height of the slot
h_{yoke}	Height of the yoke
$I,\ i$	Stator current
I_{enc}	Enclosed current
J	Magnetic polarization
J_c	Stator conductor current density
J_{PM}	Magnitude of the equivalent current density at the magnet boundaries
k_c	Carter's coefficient
k_{ed}	Eddy current empirical loss factor
k_{edy}	Empirical eddy current loss factor of the yoke equals 1.8
k_{edt}	Empirical eddy current loss factor of the tooth equals 2.5
k_{Hy}	Hysteresis empirical loss factor
k_{Hys}	Empirical hysteresis loss factor of the yoke equals 2
k_{Hyt}	Empirical hysetersis loss factor of the tooth equals 1.2
K_{ts}	Ratio of tooth width to slot width
l	Unit length
l_c	Number of conductor layers
L	Integration contour
L_d	Direct axis inductance
l_M	Length of the magnet in the direction of magnetization
l_{mt}	Mean turn length
L_q	Quadrature axis inductance
l_{stk}	Stack or active length of the machine
m	Mass of the rotor
m_c	Number of conductors connected in parallel forming one turn

m_s	Stator yoke mass
m_t	Tooth mass
N	Total number of turns
n	Rotational speed of the rotor
n_c	Number of coils connected in series
P	Rated power of the machine
p	Number of poles
P_{ad}	Additional losses
P_{cu}	Copper losses
p_{ed}	Specific eddy current loss
P_{eds}	Eddy current loss in the stator yoke
P_{edt}	Eddy current loss in the teeth
p_{Hy}	Specific hysteresis loss
P_{Hys}	Hysteresis stator yoke loss
P_{Hyt}	Hysteresis tooth loss
P_{in}	Input power to the machine
P_{loss}	Total power loss
P_{out}	Output power of the machine
P_{PM}	Magnet loss
p_{PM}	Specific magnet losses assumed to be 300W/m^2
P_t	Wind turbine power
P_{wf}	Windage and friction losses
R	Resistance
r	Radius of the rotational path
R_g	Air-gap reluctance
r_g	Midway radius through the physical air gap
R_L	Leakage reluctance

r_o	Outer radius of the stator
R_P	Magnet reluctance
$R_{r,i}$	Rotor iron reluctance
R_s	Stator reluctance
r_s	Inner radius of the stator
R_t	Turbine radius blade
R_{20}	Resistance at room temperature
S_o	Slot opening
T	Operating temperature
T_c	Curie temperature
T_{cog}	Cogging torque
T_{in}	Input torque
$T_{\max}$	Maximum operating temperature
t_p	Pole pitch
$T(\theta)$	Electromagnetic torque as function of the rotor position θ
v	Tangential speed of the rotating body
V_{fl}	Full load terminal voltage
V_M	Magnet volume
V_{nl}	No-load induced voltage
VR	Voltage regulation
v_t	Turbine blade tip speed
v_W	Wind speed
$W_{air-gap}(\theta, i)$	Co-energy of the air gap as function of the rotor position θ and stator current i
W_g	Magnet energy stored in the air gap
$W_{r,i}$	Width of the rotor iron pieces
W_{slot}	Width of the slot

W_{tooth}	Width of the tooth
$W(\theta,i)$	Co-energy as function of the rotor position θ and stator current i
X_d	Direct axis synchronous reactance
X_q	Quadrature axis synchronous reactance
Z	Magnitude of the impedance

Greek Letters

α_{Br}	Reversible temperature coefficient
α_{20}	Temperature coefficient of copper resistance at room temperature
β	Power coefficient
β_{ir}	Arc length of the rotor iron facing the stator
$\beta_{\max}$	Maximum power coefficient
ε	Permittivity
ϕ	Stator yoke flux
$\phi_{d(or,q)}$	d or q-axis stator yoke flux
ϕ_g	Air gap flux
ϕ_L	Leakage flux
ϕ_M	Magnet flux
ϕ_m	Maximum value of the stator yoke flux
ϕ_r	Remanent flux
η	Efficiency
μ	Permeability
μ_o	Permeability of free space
μ_{rec}	Relative recoil permeability
θ	Rotor position
ρ_a	Air density

ρ_{cu}	Resistivity of copper
ρ_M	Density of the permanent magnets
ρ_{20}	Resistivity of copper at $20^o C$
σ	Conductivity
σ_M	Mechanical stress resulting from the magnets
ω	Angular rotational speed
ω_t	Turbine angular tip speed
ψ	Flux linkage in a coil

Abbreviations

IGBT	Integrated Gate Bipolar Transistor
MOSFET	Metal Oxide Semiconductor Field Effect Transistor
GTO	Gate Turn Off
DC	Direct Current
AC	Alternating Current
MMF	Magnetomotive Force
EMF	Electromotive Force
FET	Finite Element Technique
PM	Permanent Magnet
rpm	Revolution Per Minute
CW	Clock Wise
CCW	Counter Clock Wise
rms	Root Mean Square
N	North
S	South
SmCo	Samarium Cobalt
NdFeB	Neodymium Iron Boron
AlNiCo	Aluminum Nickel Cobalt
PC	Permeance Coefficient
2-D	Two-Dimensional
3-D	Three-Dimensional

Chapter 1

Introduction

During the last decades, great attention has been given to the pollution-free renewable energy to be an alternative source for oil, natural gas, Uranium and coal sources that will last no longer than another 100 years. Wind energy is considered as one of the most important types of renewable energy sources that have been widely used in electricity generation. The fact is that the cost of energy supplied by wind turbines is continuously decreasing. Nowadays, almost 17,000MW wind power capacity has been installed in Germany with a total number of wind energy systems greater than 15000 units. This thesis investigates design, optimization, construction and test of a single-phase 1kW prototype machine and theoretical design study for two three-phase machines. One of them is 1kW and the other is 175W.

For the time being, most wind energy converters are designed for speeds from 750rpm up to 1800rpm. The wind turbines are usually designed to operate in a speed range of 20rpm up to 250rpm. Therefore, a gear is used as an intermediate stage between the wind turbine and generator in conventional wind energy stations. Directly coupled (gearless) generators seem to be a powerful alternative based on economic and technical considerations. In gearless wind energy converters, both the turbine and generator rotate at the same speed. The advantages of such an arrangement are:

1) High overall system efficiency.
2) High reliability and low maintenance.
3) Low overall weight and volume.
4) Low cost of electricity generated.
5) Simple power plant.
6) The noise caused by the high-speed rotation can be reduced.

The output frequency is usually different from 50Hz. A frequency converter is normally connected to the terminals of the low-speed generator. The converter makes it possible to use the machines in variable speed operation. The speed can be variable over a relatively

wide range depending on the wind conditions where the wind turbine can extract the maximum power at different wind speeds. A variable-speed wind energy conversion system is shown schematically in Figure 1.1. The permanent-magnet generator is directly connected to the wind turbine and its output varies in frequency and voltage. The output is rectified to form a DC link and an inverter using MOSFET, IGBT or GTO converts the power to AC for the grid. A compensator is connected at the AC terminals of the thyristor inverter to compensate for the reactive power demand and harmonic distortion of the thyristor inverter.

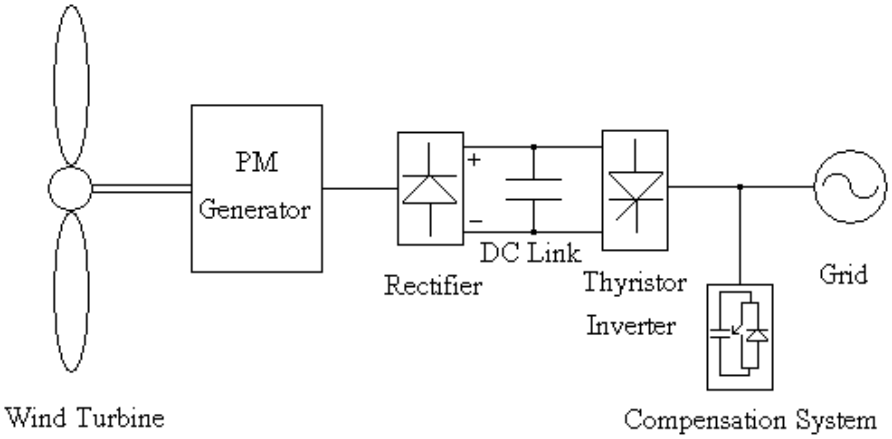

Figure 1.1: Schematic of variable-speed wind energy conversion system

Because the direct-driven generators are low speed, they are usually heavier and less efficient than conventional high-speed steam turbine generators. A special attention should be paid to reduce the weight and increase the efficiency of the generator. To decrease the weight of the rotor and stator yoke and to keep the end winding losses small, direct driven generators are usually designed with a small pole pitch. Exciting the generator by permanent magnets is another option for improving the efficiency as the field copper losses are eliminated.

1.1 Directly driven wind-energy converters

Several generator types can be used as directly driven wind-energy converters. Every generator is designed for different purposes and with different topologies and configurations. Conventional field-winding synchronous generator, permanent-magnet

synchronous generator and induction machine are three examples. Based on the direction of flux penetration, permanent-magnet generators existing now in the market are of radial-flux, axial-flux or transversal-flux machines. The axial-flux machines usually have slotless air-gap windings. This simplifies the winding design. The length of the axial-flux machine is short compared to the radial-flux machine. In radial-flux machines, the length of the stator and the air-gap diameter can be chosen independently. If necessary, the radial-flux machine can be made with a small diameter by using a long stator. Transversal-flux machine is rather different from the other machine types. The major difference between radial- or axial-flux machines and the transversal-flux machines is that the transversal-flux machines concept allows an increase in the space for the windings without decreasing the available space for the main flux, this allows for very low copper losses. The transversal-flux machine can also be made with a very small pole pitch compared with the other types. The electromagnetic structure is much more complicated than that of radial- and axial-flux machines, which makes it more expensive to manufacture.

1.1.1 Field-winding generators

Commercial direct-driven wind energy converters use field windings for the excitation of synchronous generators in combination with frequency converters. Very little detailed information is available about these generators. One of them has a power of 500kW and has a rated speed of 40rpm [1]. The air gap diameter is about 4m and the generator frequency is lower than 50Hz.

1.1.2 Permanent-magnet generators

Permanent magnet excited machines have a series of economic and technical advantages over the electrically excited type. Some of these advantages can be summarized as follows:

a) No additional power supply for the magnet field excitation.
b) Improvement in the efficiency and thermal characteristics of the motor due to absence of the field losses.
c) Higher reliability due to absence of mechanical components e.g. slip rings.

d) Higher power to weight ratio. A 3kW field-winding AC machine has a power to weight ratio of 75W/kg while a permanent magnet DC machine of the same power rating has 160W/kg [2].
e) Improvement in the dynamics of the drive due to the replacement of wound iron mover with high-energy permanent magnet.

Permanent-magnet machines allow a great deal of flexibility in their geometry. Based on the direction of flux penetration, permanent magnet machines can be classified as: radial-flux, axial-flux and transversal-flux machines.

1.1.2.1 Radial-flux permanent-magnet generators

The permanent magnets of radial-flux machines are radially oriented. Radial-flux permanent-magnet machines can be divided mainly into two types, surface-magnet and buried-magnet machines. The simple way of constructing the rotor with high number of poles is by gluing the permanent magnets on the rotor surface of the machine.

So many generators have been proposed in the literature as radial-flux generators. Spooner and Williamson (1996) have designed and constructed two small multi-pole radial-flux permanent-magnet test machines for use as a directly coupled generator in wind turbines. The first machine uses surface mounted NdFeB magnets to form a 16-pole rotor of 100mm diameter and has a stator with 36 slots housing two layers. The second machine also has a 16-pole rotor with 36 slots in the stator. The rotor is 150mm diameter and constructed with ferrite magnets and tapered pole pieces. The small magnets mounted beneath the pole pieces contribute to the total air gap flux and prevent flux leakage, which would occur in their absence. A lumped parameter magnet equivalent circuit for the structure is used for calculating the air gap flux density. For both machines, the terminal voltage is a good sine wave, whilst the voltage induced in individual coils contained significant harmonic components [3].

Grauers (1996) has investigated how a direct driven wind turbine generator should be designed and how small and efficient such a generator will be. Advantages and

disadvantages of various types of direct driven wind turbine generators are discussed and a radial flux permanent magnet generator connected to a forced commutated rectifier is chosen for detailed theoretical investigation. A design method is developed for the electromagnetic part of the chosen generator type. The generator is optimized with a simplified cost function, which includes the cost of the active generator parts, the cost of the structure and the cost of average losses. A method to calculate the average losses is derived. The design method is used to investigate the optimization of a 500kW generator. The size, efficiency and active weight of optimized generators from 30kW to 3MW are presented. The results show that the outer diameters of the direct-driven generators are only slightly larger than the width of conventional wind energy converter nacelles. It is also pointed out that the average efficiency of direct driven generators, including the losses in the frequency converters, is higher than that of conventional wind energy converter drive trains. Compared with other direct-driven generators, the proposed generator type is small, mainly because of the forced commutated rectifier and because the generator is not required to produce a pull-out torque higher than the rated [4].

Grauers *et al.* (1997) have built a 20kW 66-pole surface-mounted machine excited by high-energy NdFeB magnets. The system of the permanent magnet and the frequency converter showed good performance and high efficiency [5].

Spooner *et al.* (1996) have described the arrangement of multi-pole radial-flux permanent-magnet synchronous machines. Such machines may be used as direct-coupled generators in large grid-connected wind turbines with power ratings from below 100kW to more than 1MW and pole numbers of 100 to 300. Rotor and stator module designs and a modular structure have been presented suitable for the full range of power and pole number. The rotor modules use standard ferrite magnet blocks. The stator modules are simple E cores each carrying a single rectangular coil. A lumped-parameter magnetic model has been developed which permits rapid calculation of machine parameters. A laboratory machine has been used to demonstrate the main features of the proposed machine and has validated the theoretical magnetic model. It is concluded that the modular arrangement yields great advantages in assembly and avoids the need to bring

together two large components with large magnetic fields. It is pointed out that the absence of rotor damping circuits allows the machine to be modeled simply for steady state or transient operating conditions [6].

Papathanassiou *et al.* (1999) have designed gearless radial-flux buried and surface-mounted permanent magnet wind energy converters. A preliminary analytical design is firstly done and the finite element technique is then used to investigate the optimal electromagnetic behavior of 20kW and 50-pole machines. The results show that the torque ripple of the buried-magnet machine is higher than that of the surface-magnet machine [7].

Lampola (2000) has designed three three-phase radial-flux permanent magnet machines excited by high-energy NdFeB magnets with different types of stator windings. The first machine has a conventional three-phase diamond winding while the second machine has a three-phase unconventional single-coil winding consisting of coils which are placed in slots around every second tooth. The electromagnetic optimization of the machine is carried out by the finite element method and by a genetic algorithm combined with the finite element. The rated power of the machines optimized are 500kW, 10kW and 5.5kW. Two prototype machines are built and tested. The results show that both the cost of active materials and the pull-out torque per cost of active materials in the conventional machines are smaller than in the single-coil winding machine. The torque ripple can be reduced to a low level by choosing a suitable magnet and stator slot shape in both designs. The demagnetization of the permanent magnets can be avoided more easily in the single-coil winding machines. It is concluded that the conventional diamond-winding machine is a better choice for the design of directly driven wind turbine generator but the single-winding machine is also suitable because of its simplicity. It is pointed out that the wind power plant can be simplified by eliminating the gear and by using a low-speed permanent-magnet generator of which the rotor rotates at the same speed as the rotor of the turbine [8].

Chen *et al.* (2000) have presented the design of outer-rotor (the positions of the rotor and stator are exchanged) radial-flux permanent-magnet multi-pole low-speed directly coupled wind power converter for standalone applications. While the generator is running, the centrifugal force of the magnets applies pressure to the outer rotor core. Thus, the reliability of the glued points becomes higher. The equivalent magnetic circuit approach is used for initial design iteration and the finite element technique is then applied for the detailed characteristics and final adjustment. The prototype machine has been built with high-energy NdFeB magnets. It is verified that this machine with such a simple construction can operate with good and reliable performance over a wide range of speeds. The good agreement between theoretically predicted and experimentally tested results proves the correctness of the design principle and the effectiveness of the design methodology [9].

Hanitsch and Schulz (2003) have presented some aspects of the achievements resulting from the introduction of the 'Renewable Energy Law' in Germany. They expect that installed power capacities in 2010 will reach 110,000MW in all over the world and 25,000MW in Germany. It is pointed out that wind energy converters are a good option for the future from the environmental point of view as they contribute to the reduction of CO_2 emissions [10].

Ronghai and Thomas (2003) have proposed a dual rotor, radial-flux, toroidally wound permanent-magnet machines to substantially improve machine torque density and efficiency. The principles of operation, configurations, features, machine design, and optimization guidelines are given. A prototype machine has been designed, built and tested. The measured torque density is almost three times that of the induction machine with the same power and speed. The efficiency is still kept high and the cost of active material is kept low by using ferrite magnets. Three novel approaches are proposed to reduce the cogging torque whose validity is verified by finite element analysis and experimental measurements [11].

Hanitsch and Korouji (2004) have designed and optimized using finite element technique (FET) a rare-earth permanent-magnet radial-flux wind-energy generator with new topology. The generator is constructed from two rotors and one stator. The prototype is built and tested. The design permits short endwindings, which improves the performance of the machine by reducing the weight, increasing the efficiency and reducing the cost of active materials. The difference between the calculated and measured values is in the range of 7% [12].

Weissensteiner (2002) has proposed a radial-flux permanent-magnet electrical generator with a new topology. The design permits short endwindings, which contributes to high efficiency and high power to weight ratio. The generator has been recorded as a patent. The machine contains six poles and six flat slots. Good efficiency has been detected with low output power levels [13].

1.1.2.2 Axial-flux permanent-magnet generators

The magnetization of permanent magnets of axial-flux machines are axially oriented. Most axial-flux machines are slotless. A slotless axial machine has the advantages of easy construction, no torque ripple and rectangular permanent magnets can be easily implemented. However, large air gaps and therefore thick high-energy magnets are needed.

So many generators have been presented in the literature as axial-flux generators. Soederlund and Eriksson (1996) have examined a low-speed axial-flux multi-pole direct-coupled permanent-magnet wind-power synchronous generator mainly from the magnetic point of view. Both mechanical and electromagnetic designs are described as well as some test results of two generator models having a nominal power of 5kW and 10kW. It is concluded that this machine topology provides a compact and effective solution to wind industry applications [14].

Stiebler and Okla (1992) have presented design aspects of an axial-flux air-gap winding machine. An experimental 2.7kW 18-pole machine has been built and tested. Good agreement between theoretical and experimental results has been indicated [15].

Muljadi *et al.* (1999) designed, built and tested a modular axial-flux, permanent-magnet generator for directly coupled wind turbine applications. The windings are toroidal, like a torus, making it easy to assemble. The permanent magnets used are NdFeB or Ferrite with flux guide to focus flux density in the air gap. Each unit module of the generator may consist of one, two or more phases. Each generator can be expanded to two or more unit modules. Each unit module is built from simple modular poles. A one-unit module prototype is built and tested. With this modular concept, any failure in one unit can be replaced immediately or can be bypassed, thus minimizing turbine downtime. The geometry of the machine is not optimized as the attention of the designers has focused only on the proof of the concept [16].

The advantages of the axial-flux machines are: low cogging torque, low noise and vibration, and small length of the machine. The disadvantages are the need for a large outer diameter and large amount of magnet material in the slotless design, which makes it more costly.

1.1.2.3 Transversal-flux permanent-magnet generators

The transverse flux principle means that the path of the magnetic flux is perpendicular to the direction of the rotor rotation. The non-active part of the copper winding is to a considerable extent smaller than the corresponding parts in radial- or axial-flux machines. Weh (1995) has proposed a transversal-flux machine. The construction of the machine is very different from that of the radial- and axial-flux machines and the electromagnetic design is much more complicated. The weight of a low-speed transversal-flux machine is about half of the total weight of an asynchronous machine with a gearbox. The machine can be built for a single- or multi-phase connections. A 5.8kW prototype machine is built and 55kW machine is designed [17]. Analytical and numerical design, analysis and

performance characteristics of transversal flux machines can be found in [18], [19] and [20].

1.1.3 Induction generator

Gribnau and Kursten (1991) and Deleroi (1992) have proposed a direct-driven induction generator for direct-grid connection. The generator is an axial-flux generator with a sector only on a segment of the circumference. It has a large diameter in order to achieve a high air-gap speed. Because it is an induction generator with a high slip, the damping of the generator is not a problem for the design even though it is a direct-grid connection. Only a very little data are available about its design. The efficiency of the 500kW 40rpm generator is estimated to be about 80-85% with a rated slip of about 10-15%. The efficiency of a 150kW induction prototype machine at a rated slip of about 20% is only 65% [21] and [22].

1.2 Design tools of permanent-magnet electrical machines

In order to be able to design and dimension an electromechanical system properly, a comprehensive knowledge of the quantitative interrelation of the magnetic fields in every part of the magnetic system is required. Of particular importance is the field distribution in the air gap region where the energy conversion takes place.

In general, Maxwell equations serve for the description of magnetic field problems. For the calculation of the quasi-static fields that occur in electromechanical energy converters, the assumption of a negligible displacement current density is acceptable. The Maxwell's equations are usually supplemented with material equations. With these equations, the electromagnetic fields for a given distribution of charges and/or current can be calculated. The Maxwell's equations that are relevant for the calculations of the electromagnetic fields in electrical machines in their integral forms as well as the material equations, are given below:

$$\oint_l \vec{H} \,.\, \vec{dl} \;=\; \int_a \vec{J} \,.\, \vec{da} \;=\; I_{enc} \qquad \text{(Ampere's law)} \qquad (1.1)$$

$$\oint_l \vec{E} \cdot \vec{dl} = -\int_s \frac{\partial \vec{B}}{\partial t} \cdot \vec{ds} \qquad \text{(Farady's law)} \qquad (1.2)$$

$$\oint_s \vec{B} \cdot \vec{ds} = 0 \qquad \text{(Gauss's law)} \qquad (1.3)$$

$$\vec{B} = \mu \vec{H},\ \vec{D} = \varepsilon \vec{E},\ \vec{J} = \sigma \vec{E} \qquad \text{(material equations)} \qquad (1.4)$$

where μ is the permeability, ε is the permittivity and σ is the conductivity.

The following tools can be used in the magnetic field calculations of permanent magnet electrical machines: equivalent magnetic circuit approach, permanent magnet load line method, finite difference method, finite element technique and hybrid method. Every method has its own characteristics like high processing speed, high precision, universality and ease of adjustability or changeability of the system parameters with regard of optimization.

1.2.1 Equivalent magnetic circuit approach

The basic idea of this analytical method is the use of the analogy between magnetic and electric fields. With this method, the simulation problem reduces to analysis of a network consisting of admittances, current and/or voltage sources. In order to construct this network, the electromagnetic system and its surrounding space is partitioned into geometrically simple elements. Under the ideal assumption that the flux of the field in an element is constant and can only flow in two directions. The admittance depends on the geometry of the element and the material parameter. The permanent magnet and the coil are modeled with a current and/or a voltage source. Through logical connection of these elements, an equivalent magnetic network emerged. The topology of the network is determined by the direction of the flux lines in the system and the geometrical material succession of the field elements. Nonlinear admittances are well represented by their characteristic flux density versus field strength curves. The resulting nonlinear network analysis leads to a fast and for technical purposes sufficiently accurate simulation method. The accuracy of the method depends mainly on good calculations of the

admittances of the geometry. Detailed presentation of this method is given in the next chapter.

1.2.2 Permanent magnet load line method

Two of the Maxwell's equations, Ampere's law and Gauss's law, are used in the derivation of this analytical method. Leakage flux is accounted for by a leakage flux coefficient, f_{LKG}. A permanent magnet is represented with its demagnetization curve. The results of the calculation are the load line of the magnetic system and its intersection with the demagnetization curve of the permanent magnet, the operating point of the permanent magnet and the air-gap flux density.

The approach gives no insight into the saturation level of the soft magnetic material. As a result, it serves best as a pre-design tool for complex systems. The accuracy of the predicted values depends mainly on good estimation of the leakage flux coefficient f_{LKG}. Typical values for f_{LKG} lie in the range of 0.8 to 0.9. Detailed investigation of this method is given in the next chapter.

1.2.3 Finite difference method

This is the oldest known numerical method of calculating magnetic fields. A network of rectangular meshes is drawn on the area to be calculated. The Maxwell's differential equations for the magnetic potentials at the nodes are replaced with a system of difference equations. This system of linear equations is solved iteratively until convergence occurred. The results are the magnetic potential at the various nodes. Due to the high meshing involved, the resulting system of equations is large. This method is gradually being replaced by new methods because of its inflexibility in the handling of complex geometry and relative inefficiency.

1.2.4 Finite element technique

This is the most popular method used today. The system to be calculated is partitioned or meshed into a number of simple and flexible elements like triangles, quadrangles, tetrahedrons…etc. This flexibility in the geometry of the element is exploited in the

adaptive mesh generating function and represents the major advantage of this method over the finite difference method. In each of these finite elements, an initial or starting function is chosen. The coefficient matrix of the resulting system of equations is very large, sparse, symmetric and positive definite and therefore are easily amenable to efficient solution methods. A detailed investigation and application of this method is presented in next chapters.

1.3 Wind energy turbine power equations

The nominal speed of the permanent-magnet generator, which largely determines the overall size of the generator, can be determined from the wind energy assessment equation. A wind turbine can develop the following power P_t:

$$P_t = \frac{1}{2} C_p \rho_a \pi . R_t^2 v_w^3 \qquad (1.5)$$

where:

C_p: conversion efficiency called Betz factor with a typical average value of 0.45 or below (modern turbines reach almost 0.5).

ρ_a: air density, 1.184 kg/m^3 for 25 ^oC at sea level.

R_t: radius of the turbine blade.

v_w: wind speed.

A power coefficient can be defined as the ratio of the turbine's blade tip speed to the wind speed given below:

$$\beta = \frac{v_t}{v_w} = \frac{\omega_t R_t}{v_w} \qquad (1.6)$$

where:

v_t: blade tip speed.

ω_t: turbine shaft angular tip speed.

Detailed analysis shows that a single maximum $C_{p,\max}$ occurs when β takes a particular value $\beta_{\max}$. Obviously, if the turbine is to extract maximum power from the wind, the shaft speed should vary accordingly to the wind speed. When the turbine is running at $\beta_{\max}$, the output power from the turbine is:

$$P_t = (\frac{1}{2}\rho_a \pi . C_{p,\max} R_t^2) v_w^3 \qquad (1.7)$$

The terms in the bracket are considered constant for a given wind turbines, and hence, the output power varies as the cube of the wind speed. P_t can be alternatively expressed in terms of ω_t as

$$P_t = (\frac{1}{2}\rho_a \pi . C_{p,\max} \frac{R_t^5}{\beta_{\max}^3}) \omega_t^3 \qquad (1.8)$$

1.4 Objectives and scope of the thesis

In this thesis, detailed design, optimization, construction and test of radial-flux low-speed rare-earth high-energy permanent-magnet electrical machines with new topology are investigated. The main objectives of this work are therefore to study the characteristics of this new topology, the validity of the design methodology and the closeness of the practical results to the theoretically predicted.

The main contribution of the thesis is the new topology of the proposed machines, which shows relatively high efficiency, low active material cost and a typical 'rule of thumb' value for the leakage flux coefficient.

This thesis is organized as follows: Chapter 2 gives a brief description for the permanent magnet materials and the magnetic circuit design. The iterative preliminary design of the machine and the results of the optimization process are presented in Chapter 3. The FET results including cogging torque analysis are given in Chapter 4. The focus of Chapter 5 is on the machine construction, used material and technology. Chapter 6 outlines the experimental investigations and some comparison between the theoretical and practical results. The effect of slot filling on the cogging torque and performance of the machine is

summarized in Chapter 7. Finite element design of two three-phase machines is presented in Chapter 8. Finally, some conclusions together with suggestions for future work are drawn in Chapter 9.

Chapter 2

Permanent Magnet Materials and Magnetic Circuit Design

The flux in permanent-magnet machines is established by the magnets. Both the internal generated voltage of the generator and the electromagnetic torque of the motor are proportional to the established flux of the machine. The flux is clearly one of the most important parameters in the design process. The flux is intended to link the coils of the phase windings on the stator, these coils are located as close as possible to the magnets to minimize the amount of magnet flux that leaks from the N-pole to the S-pole without linking any turns of the windings. The laminated ferromagnetic core of the stator acts as a flux guide. The high permeability steel teeth draw the flux radially across the narrow air gap while the yoke returns it from the N-pole to the S-pole with very little expenditure of magnetomotive force (MMF) or magnetic potential drop. The rotor soft magnetic areas perform a similar function inside the rotor. Because the soft magnetic stator and rotor absorbs very little MMF, most of the magnet's MMF is available to drive flux across the air gap.

The slotting is an ingenious way to achieve a narrow air gap length while keeping the winding conductors close to the magnet. Additionally, the slotted structure provides a rigid housing for the windings and increases the surface contact area between the windings and the steel, providing a path of low thermal resistance, which is important in keeping the windings cool.

The soft magnetic material does not have unlimited capacity for carrying the flux. If the flux density exceeds approximately 1.6-1.7T, the permeability decreases rapidly. At a flux density of about 2.1T, the incremental permeability of the soft magnetic material is practically the same as that of air. The magnetic design should insure that the flux densities in the soft magnetic material are kept below these levels, otherwise the magnet MMF will be wasted in driving flux through the soft magnetic material or the amount of magnet material required to establish a given flux would be greatly increased.

Another reason for limiting the flux density in the soft magnetic material, especially in the stator, is that the core losses increase rapidly at high flux density. Core losses are caused by **hysteresis** and **eddy currents**. The eddy current component can be reduced by stamping the laminations from thinner-gauge sheet, or by using high Silicon steels. Both of theses measures add costs to the manufacturing process but reduce the iron losses.

2.1 Permanent magnets and magnetic circuits, [23]

A permanent magnet can be regarded as a flux source, and the magnetic field can be calculated by means of the magnetic circuit, which is analogous to a simple electric circuit. The correspondence between the variables is given in Table 2.1.

Table 2.1: Magnetic/Electric circuit analogy

Magnetic Circuit Parameter		**Electric Circuit Parameter**	
Flux	(Wb or Vs)	Current	(A)
MMF	(A)	Voltage	(V)
Reluctance	(A/Wb)	Resistance	(Ω)

Electric circuit analysis employs ideal current and voltage sources, and real sources of current and voltage can be represented by their Thevenin or Norton equivalent circuits, i.e. a voltage source in series with an internal resistance, or a current source in parallel with an internal conductance. Similarly, in magnetic circuits a permanent magnet can be represented by a Thevenin equivalent circuit, which comprises an MMF source in series with an internal reluctance R_P, or by a Norton equivalent circuit comprising a flux source in parallel with an internal permeance $(1/R_P)$.

The Thevenin and Norton equivalent circuits are exactly equivalent and cannot be distinguished from each other by measurements at the terminals since they both represent the same thing. Which one to use is a matter of convenience. For example, in the Norton equivalent circuit the internal leakage permeance represents flux that circulates inside the

magnet and does not emerge from the pole faces. Figure 2.1 shows the Thevenin and Norton equivalent magnetic circuits.

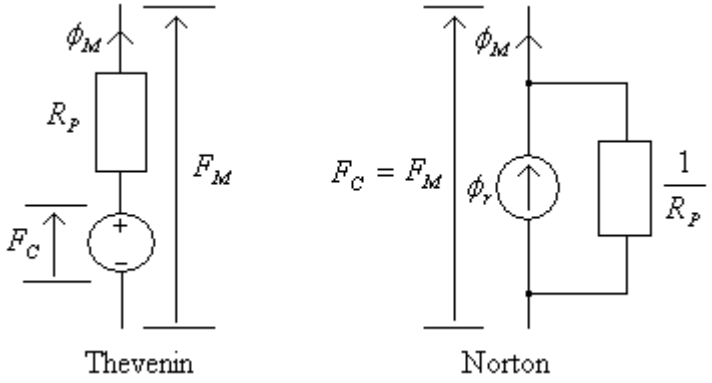

Figure 2.1: Thevenin and Norton equivalent magnetic circuit

The characteristics of a permanent magnet can be expressed graphically in terms of the Flux/MMF relationship at the terminals or pole faces as shown in Figure 2.2. This is analogous to the voltage/current relationship of an electrical source at its terminals. The magnet can be short circuited by connecting a soft iron keeper across its poles. This ensures that the MMF across the terminals is zero and the magnet is operating at the short circuit point. The open circuit condition, on the other hand, requires that the flux leaving the magnet poles is zero. In order to achieve this, an external demagnetizing MMF must be applied to suppress the flux. The external MMF must exactly balance the internal MMF of the magnet when the flux emerging from the poles is zero. It is only possible to do this in a magnetizing fixture with a separate DC coil, which provides the external MMF. The terminal MMF is negative because it opposes the internal MMF F_c of the magnet, and is exactly equal to it. F_c is called the coercive MMF because it is the MMF required to coerce the magnet to produce zero flux. It directly expresses the resistance of the magnet to demagnetization.

The amount of flux ϕ_r that can be produced into an infinitely permeable keeper expresses the maximum available flux from the magnet. ϕ_r is called the remanent flux. This term describes how much flux remains in the magnet after it has been magnetized. It should be

interpreted carefully, because the ability of a magnet to retain flux in a magnetic circuit depends on F_c as much as it does on ϕ_r. It is better to think of ϕ_r as the flux retained by a keeper in the magnetic short circuit condition.

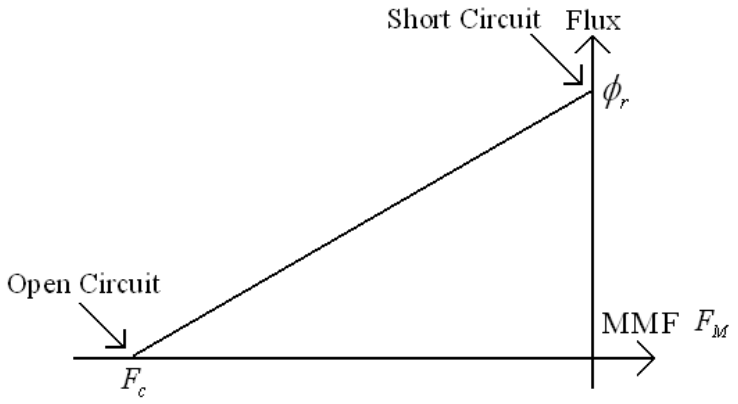

Figure 2.2: Schematic diagram of MMF/Flux characteristics of a permanent magnet

In normal operation there is no keeper, and the magnet operates at a flux below ϕ_r. This is because the MMF drop across the air gap appears as a negative demagnetizing MMF as seen from the magnet terminals. In addition, the phase currents produce an additional demagnetizing MMF, which drives the operating point further down the characteristics.

It is clear from this that magnets require two parameters F_c and ϕ_r to characterize them properly. Moreover, the slop of the magnet characteristic relates F_c and ϕ_r. For a given remanent flux ϕ_r, it is desirable to have the flattest possible slope since this is associated with a high value of F_c and a high resistance to demagnetization.

The remanent flux ϕ_r and the coercive MMF F_c depend not only on the material properties but also on the dimensions of the magnet, and this makes matters a little more complicated than the simple magnetic equivalent circuit. The material property associated with ϕ_r is the remanent flux density B_r, and this is related to ϕ_r by the equation:

$$\phi_r = B_r A_M \qquad (2.1)$$

where A_M is the magnet pole area. The material property associated with F_c is the coercive magnetizing force of coercivity H_c, and this is related to F_c by the equation

$$F_c = H_c l_M \qquad (2.2)$$

where l_M is the length of the magnet in the direction of magnetization. From these equations, it is clear that if the vertical axis of Figure 2.2 is scaled by $1/A_M$ and the horizontal axis by $1/l_M$, the result will be a relationship between B_M and H_M, the flux density and magnetic strength of the magnet respectively. These in turn are related to the magnetic flux ϕ_M and the MMF drop F_M at the operating point:

$$\phi_M = B_M A_M \quad \text{and} \quad F_M = H_M l_M \qquad (2.3)$$

The graph of B_M vs. H_M is shown in Figure 2.3, and this is, in fact, the second quadrant of the B/H loop or hysteresis loop of the magnetic material.

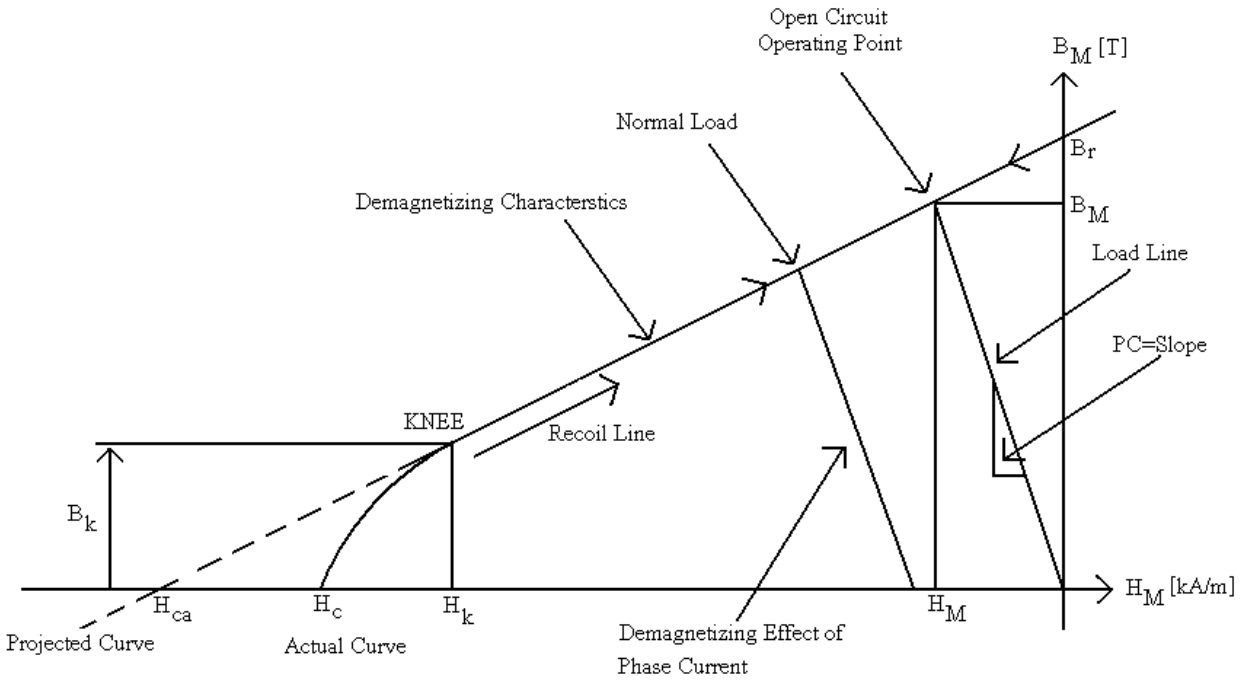

Figure 2.3: Schematic diagram of B/H characteristics of permanent magnet material

The magnet's operating point generally moves reversibly up and down on the straight part of the characteristics shown in Figure 2.3. This characteristic is called the **demagnetizing characteristic**. The slope is the **recoil permeability**.

The unit of the horizontal axis is A/m while of the vertical axis is T. So, the slope of the demagnetizing characteristic equals to the **relative recoil permeability** μ_{rec}. Hard permanent magnets have relative recoil permeability in the range 1.05-1.15, close to that of air.

We have already seen that the air gap applies a static demagnetizing field to the magnet, causing it to operate below its remanent flux density. With no current in the phase windings, the operating point is typically at the point labeled Open-Circuit Operating Point in Figure 2.3, with B_M of the order of 0.7-0.95 of B_r. The line from the origin to the Open-Circuit Operating Point is called the **load line**.

The magnet characteristics are often plotted with a horizontal axis $\mu_o H$ instead of H. The slop of the load line is the **permeance coefficient** PC. With the horizontal axis plotted as $\mu_o H$ instead of H, the permeance coefficient is typically in the range 5-15.

When current flows in the stator windings, the additional field may drive the operating point still further down the demagnetization characteristic, depressing the air gap flux density as well as the magnet flux density below the open circuit or no load value. When this current is removed, the operating point recovers to the open circuit point, and the recovery is complete and reversible provided that the excursion of the operating point has not left the straight part of the demagnetization characteristic. The straight part, over which the magnet normally operates, is called the **recoil line**.

In Figure 2.3, the intersection of the recoil line with the negative H_M axis is labeled H_{ca}, the **apparent coercivity**. This is usually used in the magnetic circuit calculation. The **actual coercivity** is labeled H_c.

The best grades of hard permanent magnets have demagnetization curves that remain straight throughout the second quadrant and in some cases well into the third quadrant (negative B_M as well as negative H_M). These magnets can withstand a demagnetizing field that is sufficient actually to reverse the flux in the magnet, and still recover with no permanent loss of magnetism.

Other materials have a knee in the second quadrant, as in Figure 2.3. If the operating point is forced below the knee by severe demagnetizing force, then the magnet recovers along a lower recoil line when it is removed. Figure 2.4 shows an example in which the demagnetizing field is just sufficient to reduce B_M to zero. The magnet recoils along the depressed recoil line, but it has lost 20% of its remanent flux. This loss is irreversible.

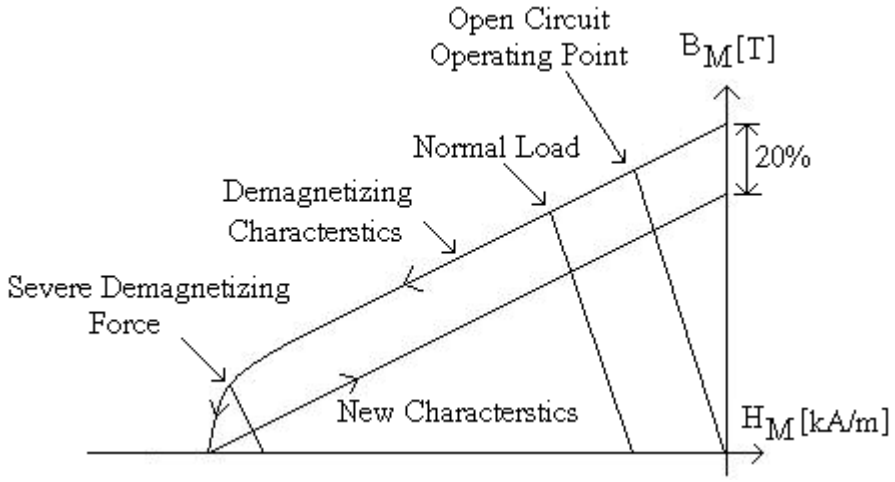

Figure 2.4: Schematic diagram shows the effect of severe demagnetizing force

A material which has a straight demagnetization characteristics at room temperature may develop a knee in the second quadrant at higher temperatures (this is the characteristic of some grades of *SmCo* and *NdFeB*), or at lower temperatures (This is the characteristic of Ferrite magnets).

Generally, the remanent flux density B_r decreases with temperature as shown in Figure 2.5. This effect is usually specified in terms of the **reversible temperature coefficient** of

B_r, quoted in % per degree C. If this coefficient is given the symbol α_{Br}, then the remanent flux density at temperature $T\ ^oC$ is given by

$$B_r(T) = B_r(20) \times (1 + \alpha_{Br}(T - 20)/100) \qquad (2.4)$$

where $B_r(20)$ is the value of B_r at 20 ^oC.

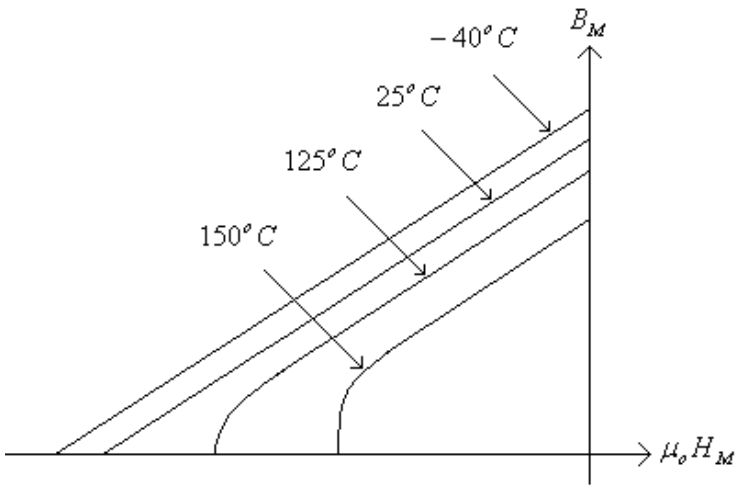

Figure 2.5: Schematic diagram of the magnet characteristics as function of temperature

The design procedure in this thesis begins by assuming a straight demagnetization characteristic. At the end of the magnetic circuit calculation, the magnetic flux density B_M should be checked to be greater than B_K by referring to the actual magnetization curves of the material at the appropriate temperature as shown in Figure 2.3. This procedure is safe and simple [23].

There are many different types of permanent magnets with varying properties and applications. One class of permanent magnets is known as Ferrites, which are now commonly used because they are relatively inexpensive to make. *AlNiCo* (Aluminum-Nickel-Cobalt) is another type of permanent magnets. Permanent magnets can be ranked according to their energy product $(BH)_{\max}$, which is the density of the useful magnetic energy that can be stored in a magnet. Both Ferrites and *AlNiCo* have a relatively low energy product. *SmCo* (Samarium-Cobalt) permanent magnets have an energy product

greater than Ferrites and $AlNiCo$. $SmCo$ can hold large magnetic fields at high temperature. On the other hand, $SmCo$ are most often only used in military and space applications because of their expense. $SmCo$ was discovered in 1966. This discovery of the class of magnets known as rare-earth permanent magnets prompted a renaissance in research into new magnet materials. $NdFeB$ (Neodymium-Iron-Boron) compounds have an advantage over the $SmCo$ compounds in that the elements are less scare and higher energy products can be created. However, some of these compounds are not as suitable for high temperature applications as they tend to lose their magnetic properties at high temperatures and are more susceptible to corrosion. $NdFeB$ was announced in 1983 [24].

$NdFeB$ permanent magnets come in either the sintered or bonded forms from the commercial suppliers. Sintered $NdFeB$ magnets offer excellent magnet properties including high $(BH)_{\max}$ values that are more than 30% greater than those of $SmCo$ materials. Furthermore, sintered $Nd_2Fe_{14}B$ alloys are significantly stronger than $SmCo_5$ alloys, allowing the design engineer more flexibility in the design of the magnetic material in new designs. Bonded $NdFeB$ are also quite widely available. Their energy product is only about 20% of that of the sintered magnets. Bonded $NdFeB$ magnets are of interest wherever operation temperatures are not excessive [2]. Table 2.2 shows the typical values of some magnetic and mechanical properties of selected permanent magnets. Apart from $AlNiCo$ permanent magnets, the relative permeability or recoil permeability of most permanent magnets is very close to that of air or free space. The $NdFeB$ magnets are obviously superior to $SmCo$ at least at room temperature.

Table 2.2: Magnetic- and characteristic- properties of typical permanent magnets

Parameter	Unit	Sintered *NdFeB*	Sintered Sm_2Co_{17}	*Bonded NdFeB*	*Bonded* Sm_2Co_{17}	*AlNiCo*	Ferrite
B_r	T	0.7-1.41	0.95-1.15	0.45-0.68	0.55-0.59	1.15	0.365
H_c	kA/m	800-1500	690-820	310-460	360-416	48	175
$(BH)_{\max}$	kJ/m^3	220-385	180-225	35-80	56-64	36	25.5
μ_{rec}	-	1.07	1.02-1.04	1.25	1.05-1.1	5.0	1.35
$(1/B_r)(\partial B_r/\partial T)$	$\%/C$	-0.10	-0.04	-0.1	-0.04	-0.02	-0.2
$(1/H_c)(\partial H_c/\partial T)$	$\%/C$	-0.6	-0.2	-0.6	-0.04	0.03	0.3
T_c	^oC	310	725-800	340	725	860	450
$T_{\max}$	^oC	100-180	250-300	150	80	450	200
H_M	kA/m	2500	3600	2500	3600	280	1000
Density	kg/m^3	7400	8300-8400	6000	5100	7400	5000

The values of $(1/X)(\partial X/\partial T)$, where X stands for the remanence or the coercivity, give the reversible temperature coefficient of the remanent flux density and the coercivity. It is to be noted that there are two principle classes of temperature characteristics. Generally, all permanent magnets lose some of its remanent flux density with increasing temperature as shown in Figure 2.5. On the other hand, with respect to the behavior of the coercivity under the influence of temperature, differences emerged. While *AlNiCo* and ferrite magnets register an increase of the coercivity with increasing temperature, the high-energy rare-earth permanent magnets, *NdFeB* and *SmCo* contrarily lose coercivity. From the values of these coefficients, it is clear that of the two high-energy rare-earth permanent magnets, *NdFeB* is more temperature sensitive than *SmCo*. Among the conventional permanent magnets, *AlNiCo* is the most stable under the influence of

temperature. This is justified by its lowest values of $(1/B_r)(\partial B_r/\partial T)$ and $(1/H_c)(\partial H_c/\partial T)$.

2.2 Approximate calculations of flux

The first task is to identify the main flux paths and assign reluctances and permeances to the various branches. Figure 2.6 shows a schematic diagram of the main flux paths, reluctances and MMFs of the magnetic circuit. The main flux or the **air gap flux** ϕ_g crosses the air gap and links the coils of the phase windings. The **magnet flux** ϕ_M is the flux actually passing through the magnet. The **leakage flux** ϕ_L is that part of the magnet flux which fails to link the phase windings. These fluxes are all defined on a per pole basis and their unit is Weber (Wb). The **leakage coefficient** f_{LKG} is defined as the ratio of air gap flux to magnet flux:

$$f_{LKG} = \frac{\phi_g}{\phi_M} = \frac{\phi_g}{\phi_g + \phi_L} \tag{2.5}$$

The leakage coefficient is less than 1. Its value depends on the configuration of the motor. A typical 'rule of thumb' value for most motor types is 0.9.

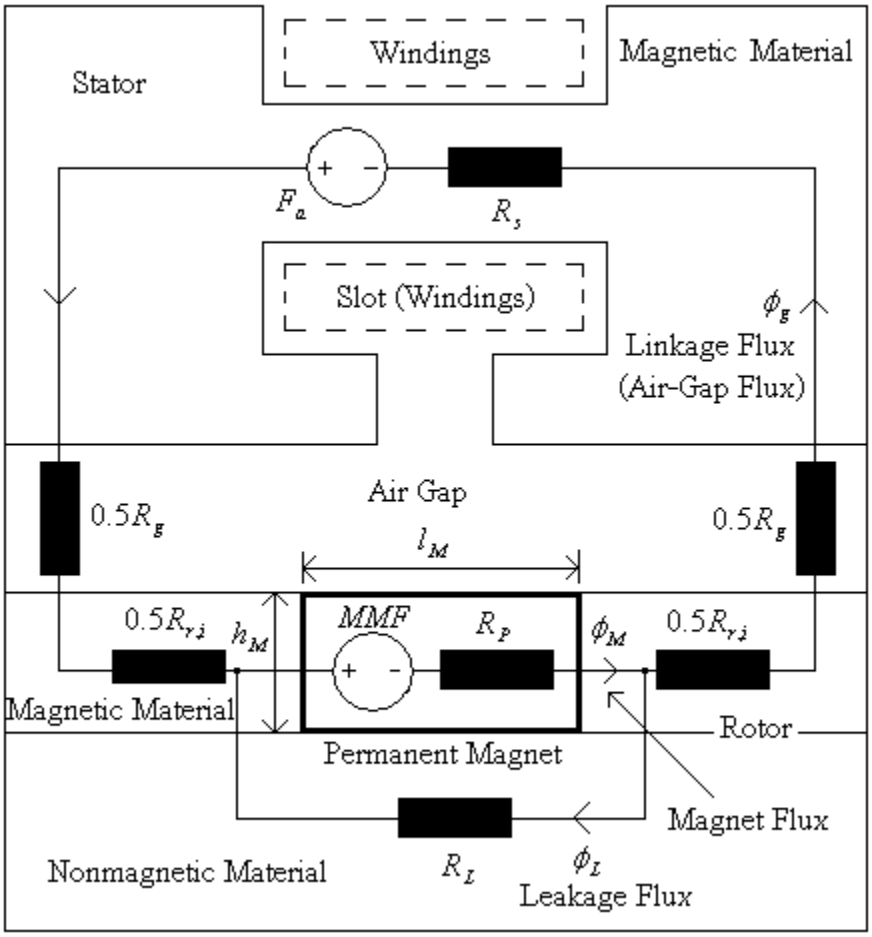

Figure 2.6: Schematic diagram of the main flux paths, reluctances and MMFs of the new prototype

Figure 2.7 shows the magnetic equivalent circuit of one pole pitch concluded from the schematic diagram of Figure 2.6. The leakage reluctance R_L is in parallel with the air gap reluctance R_g. The armature MMF F_a due to phase current is assumed initially zero (open electrical-circuit conditions) and the reluctances of the stator R_s and rotor iron $R_{r,i}$ are omitted as they are assumed infinitely permeable. Assuming a straight demagnetization characteristic as well as uniform properties and magnetization throughout the magnet, the magnet reluctance R_p will be:

$$R_P = \frac{l_M}{\mu_o \mu_{rec} A_M} = \frac{l_M}{\mu_o \mu_{rec} h_M l_{stk}} \qquad (2.6)$$

where l_M : length of the permanent magnet in the direction of magnetization.

A_M : pole magnet area.

l_{stk} : stack or active length of the machine.

h_M : height of the permanent magnet.

The air gap reluctance R_g is given by:

$$R_g = \frac{g'}{\mu_o A_g} = \frac{k_c g}{\mu_o \beta_{ir} r_g l_{stk}} \tag{2.7}$$

where g': the effective air gap length determined by the use of the Carter's coefficient k_c, (see Appendix A).

g : the physical air gap length.

r_g : midway radius through the physical air gap.

β_{ir} : arc angle of the rotor iron facing the stator (mechanical radians).

A_g : rotor iron area facing the stator equals $r_g \beta_{ir} l_{stk}$.

The MMF of the permanent magnet is concluded from the Norton equivalent circuit shown in Figure 2.1 as:

$$MMF = \phi_r R_P \tag{2.8}$$

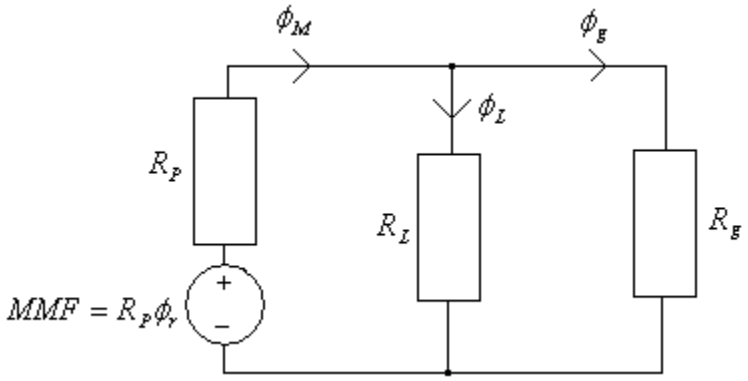

Figure 2.7: Magnetic equivalent circuit of one pole pitch

From the circuit shown in Figure 2.7, the relation between ϕ_g and ϕ_M is:

$$\phi_g = \phi_M \frac{R_L}{R_L + R_g} \tag{2.9}$$

The relation between ϕ_M and ϕ_r is:

$$\phi_M = \frac{MMF}{R_P + \frac{R_L R_g}{R_L + R_g}} = \phi_r \frac{R_P}{R_P + \frac{R_L R_g}{R_L + R_g}} \tag{2.10}$$

From Eq. (2.9),

$$\phi_M = \phi_g \frac{R_L + R_g}{R_L} \tag{2.11}$$

Substituting Eq. (2.11) in Eq. (2.10), gives

$$\phi_g = \phi_r \frac{R_P}{R_P + \frac{R_L R_g}{R_L + R_g}} \frac{R_L}{R_L + R_g} \tag{2.12}$$

Keeping in mind that Eq. (2.5) can be written as:

$$f_{LKG} = \frac{\phi_g}{\phi_M} = \frac{R_L}{R_L + R_g} \tag{2.13}$$

Then, Eq. (2.12) can be simplified to:

$$\phi_g = \frac{f_{LKG}}{1 + f_{LKG}(R_g / R_P)} \phi_r \tag{2.14}$$

In terms of the respective flux densities, since $\phi_r = B_r A_M$ and $\phi_g = B_g A_g$, we can get the following expression for the open circuit air gap flux density:

$$B_g = \frac{f_{LKG} \frac{A_M}{A_g}}{1 + \mu_{rec} f_{LKG} \frac{A_M}{A_g} \frac{g'}{l_M}} B_r \tag{2.15}$$

Having $f_{LKG} < 1$ means that the air-gap flux density is reduced compared to the value it would have if there were no leakage. The corresponding flux density B_M can be determined as:

$$B_M = B_g \frac{1}{f_{LKG}} \frac{A_g}{A_M} = \frac{\phi_g}{f_{LKG} A_M} \tag{2.16}$$

A convenient formula for the permeance coefficient PC is:

$$PC = \frac{1}{f_{LKG}} \frac{l_M}{g'} \frac{A_g}{A_M} \tag{2.17}$$

Another useful relationship for the permeance coefficient is (Hendershot & Miller, 1994):

$$B_M = \frac{PC}{PC + \mu_{rec}} B_r \tag{2.18}$$

The operating point of the magnet can now be determined either graphically, from Figure 2.3, or by calculating H_M from the equation that describes the demagnetization characteristics:

$$B_M = \mu_{rec} \mu_o H_M + B_r \quad \text{implies that } B_M > B_k . \tag{2.19}$$

The inequality $B_M > B_k$ expresses the need to check that the operating point is above the knee point.

Since μ_{rec} is close to unity for most hard magnets used in PM machines, a high permeance coefficient ensures that the magnet operates close to its remanent point. A value of 5 would be typical, giving $B_M = 0.83 B_r$ with $\mu_{rec} = 1$. If the permeance coefficient is as low as 1, then with $\mu_{rec} = 1$ $B_M = 0.5 B_r$, which corresponds to the maximum energy product $(BH)_{\max}$.

It can be seen from these design equations that, with a given magnet material, the need for a high flux density is satisfied by increasing the length of the magnet in the direction of magnetization as much as possible in relation to the air gap length, while the need for a large flux per pole is satisfied by increasing the magnet pole area. For the open circuit condition the magnet volume per pole can be shown to satisfy the equation

$$V_M = \frac{2W_g}{|B_M H_M|} \tag{2.20}$$

where W_g is the magnet energy per pole stored in the air gap, equal to $0.5B_g H_g A_g g$. This energy is determined by the volume of the air gap and the flux density B_g, so in order to minimize the volume of magnet material required, it appears that the magnet should be operated with the maximum energy product $\left|B_M H_M\right|$. If the demagnetization characteristic is straight, then the maximum energy product occurs when $B_M = 0.5B_r$, with a permeance coefficient approximately equals to 1, i.e., the operating point is halfway down the demagnetization characteristic. However, this theoretical result is seldom applied in practical machine design. The reasons are: the allowances needed for the demagnetizing MMF of the phase currents and temperature effects. Nevertheless, it is still meaningful to talk about a magnet material as having a high maximum energy product $(BH)_{\max}$, because this is a single number representing the fact that both the remanent flux density and the coercivity are high. In common parlance, the $(BH)_{\max}$ figure is widely used to express the strength of various magnet grades.

2.3 Armature reaction and demagnetization

Current flowing in the stator tends to distort the magnetic field set up by the permanent magnet. The larger the stator current, the larger the distortion of the field. In DC machines, this effect is known as **armature reaction**. In permanent magnet machines where the magnets are of surface type, the effect is weak because the magnets present a low permeability to the MMF of the stator current.

The most important effect of armature reaction in permanent magnet machines is the possibility of partially or totally demagnetizing the magnets. The effect of armature reaction or the loading effect should be studied at least with the worst loading conditions and the design must be changed if the effect is severe.

2.4 Cogging torque

Cogging torque is an oscillatory torque caused by the tendency of the rotor to line up with the stator in a particular direction where the reluctance of the magnetic circuit seen by the magnets is maximized. Cogging torque exists even when there is no stator current. When

the motor is running, additional oscillatory torque components can result from the interaction of the magnet with space harmonics of the winding layout and with current harmonics in the drive current. These additional oscillatory torque components are electromagnetic and are generally referred to as **torque ripple**, while the term **cogging** is often reserved for the zero-current condition. In a well designed machine, the torque ripple and the cogging should both be negligible, but it is possible for the torque ripple to exceed the cogging torque by a large amount if the motor has an inappropriate combination of winding layout, drive current and internal geometry.

With a large number of slots per pole the cogging torque is inherently reduced by the fact that the relative reluctance variation seen by the magnets is reduced as it successively covers and uncovers the slots one at a time. In fact, the reluctance variation can be thought of as being concentrated at the edges of the magnet. A small amount of skew is then usually sufficient to eliminate most of the cogging. When the number of slots per pole is closer to 1, the slot geometry becomes more important and the widths of the teeth in particular can be adjusted to minimize the cogging effect.

2.4.1 Cogging torque calculation approaches

Cogging torque calculations techniques fall into two primary categories: analytical and numerical [25]. Analytical approaches typically begin with calculation of the air gap magnetic flux density distribution [26], [27], [28] and others. These calculations invariably require a series of simplifying approximations in order to make the problem more tractable, such as assumptions of infinite iron permeability and/or zero flux density under the stator slots. Cogging torque is then derived from the flux density distribution either by taking the derivative of the associated co-energy or by summing the lateral magnetic force along the sides of the stator teeth.

Finite element analysis is the most popular approach for numerical calculation of the cogging torque [29], [30], [31] and others. However, closer examination indicates that there are many variations in how finite element analysis is used. Although the majority of reported studies have used well-established 2-dimensional (2-D) finite element analysis,

more recent work has applied 3-dimensional (3-D) formulations in efforts to model the influence of machine end effects and structure skewing more accurately. Torque is typically extracted from the finite element analysis using one of two approaches:

1) the energy method by which the torque is calculated from differences in the magnetic vector potential at incremental angular positions.
2) more direct torque calculation by integrating the resulting Maxwell stress tensor over the machine's air gap surface.

Reported results suggest that no one of these cogging torque calculation methods can be judged superior to the others under all conditions. Although the finite element analysis techniques offer opportunities for more precise field calculations than the analytical approaches based on simplifying assumptions, the finite element results are also subjected to errors introduced by mesh generation problems or inadequate models of the iron and magnetic characteristics. Given the complicated machine geometries and associated nonlinearities in material properties, there is a general trade-off between calculation complexity and required torque prediction accuracy, which must be judged on a case-by-case basis.

2.4.2 Cogging torque minimization techniques

An extensive variety of techniques for minimizing cogging torque is documented in the literature for both sinusoidal and trapezoidal permanent magnet machines. The majority of this work has been carried out during the last decade coincident with the growing interest in brushless permanent magnet machines for high performance applications [25].

One of the most effective and familiar technique for cogging torque minimization is stator slot skewing. Several studies have demonstrated that skewing the stator slots by one stator tooth pitch can reduce the cogging torque to very low levels [32], [33] and [34]. If stator skewing poses unacceptable manufacturability problems, the alternative approach of skewing the rotor magnetic field distribution via either skewing rotor magnet magnetization or skewing the discrete magnet segments on the rotor.

Because the air gap magnetic permeance variations caused by stator slots are such an important factor in cogging torque generation, a variety of additional techniques have been suggested for minimizing these variations or at least favorably modifying their harmonic spectra. One of the more obvious of these approaches is minimization of the stator slot openings [35] and [36]. Taking this approach a step further, slotless stator configurations have been adopted in applications where total elimination of cogging torque is required.

Other techniques seek to reduce cogging torque production by pushing the harmonic components in the spatial air gap permeance distribution to higher frequencies by either adding dummy slots or dummy teeth to the stator laminations. Alternatively, this frequency spectrum can be beneficially modified to reduce cogging torque either by shifting the angular positions of individual stator slots or by adopting a fractional number of slots per pole.

Alternative approaches for reducing cogging torque have been investigated with unskewed stators. For example, optimal ratios of magnet arc width to pole pitch have been identified, combined with a strategy of shifting alternate magnet arcs by one-half stator slot pitch in multi-pole designs [29], [33] and [37]. However, the effectiveness of these techniques is dependent on maintaining accurate mechanical tolerances on the physical dimensions and magnetization of the rotor magnets. Other rotor-based techniques, which have been proposed for reducing cogging torque, include shaping of the rotor magnet segments and addition of thin magnet retaining ring. In this thesis, it is shown that slot opening filling with bonded soft magnetic material of relative permeability higher than that of air is another possible approach to reduce the cogging torque.

Chapter 3

Preliminary Design and Parameter Optimization

As previously mentioned, the equivalent magnetic circuit approach and permanent magnet load line characteristics are used for the preliminary design and parameter optimization. In this chapter, the basic design equations, the optimization alogarithm and results are presented.

3.1 Design parameters

The Root-Mean-Square (rms) value of the induced voltage E_{rms} of the generator of this topology, assuming a sinusoidal air gap flux density distribution, is:

$$E_{rms} = \frac{2\pi}{\sqrt{2}} N f \phi_m = 4.44 N f \phi_m \qquad (3.1)$$

where N : total number of turns per phase.

f : frequency of the induced voltage.

ϕ_m :maximum value of the stator yoke flux density.

The flux ϕ_m can be expressed in terms of the flux output from the permanent magnets ϕ_M at the operating point as:

$$\phi_m = \phi_M f_{LKG} \qquad (3.2)$$

where ϕ_M is the permanent magnet flux and can be written in terms of the flux density of the permanent magnets B_M at the operating point as:

$$\phi_M = B_M A_M \qquad (3.3)$$

where A_M is the magnet pole area. It can be written in terms of the dimensions of the permanent magnet as shown in Figure 3.1 as:

$$A_M = h_M l_{stk} \qquad (3.4)$$

where h_M is the height of the permanent magnet and l_{stk} is the active length of the machine.

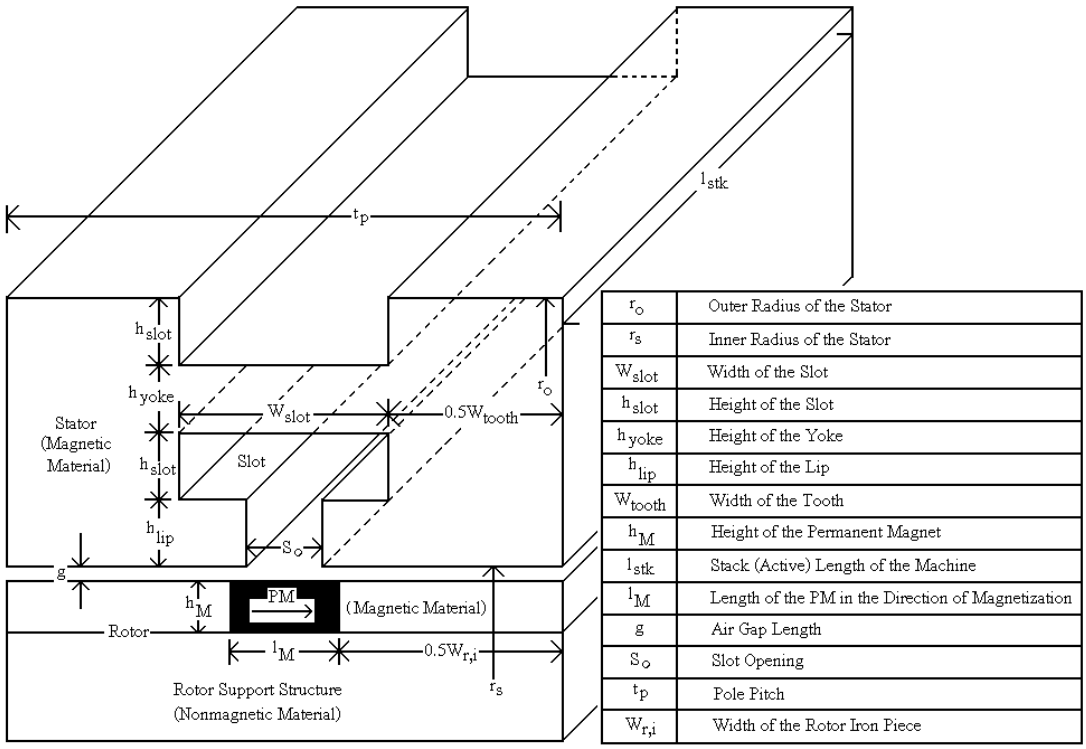

r_o	Outer Radius of the Stator
r_s	Inner Radius of the Stator
W_{slot}	Width of the Slot
h_{slot}	Height of the Slot
h_{yoke}	Height of the Yoke
h_{lip}	Height of the Lip
W_{tooth}	Width of the Tooth
h_M	Height of the Permanent Magnet
l_{stk}	Stack (Active) Length of the Machine
l_M	Length of the PM in the Direction of Magnetization
g	Air Gap Length
S_o	Slot Opening
t_p	Pole Pitch
$W_{r,i}$	Width of the Rotor Iron Piece

Figure 3.1: Main dimensions of one pole pitch

Substituting for ϕ_m in the voltage equation (3.1) gives

$$E_{rms} = 4.44 N f B_M h_M l_{stk} f_{LKG} \tag{3.5}$$

where f_{LKG} is the leakage flux coefficient.

With the typical value of the permeance coefficient PC of 5 and the recoil permeability μ_{rec} close to unity (see Eq. (2.18)), B_M equals $0.83 B_r$. A typical 'rule of thumb' value for the leakage coefficient f_{LKG} is 0.9. A value of 0.85 is acceptable for preliminary design purposes.

The frequency f of the voltage is calculated from the speed n using the following equation:

$$f = \frac{np}{120} \tag{3.6}$$

where n : rotational speed of the rotor in rpm.

p : number of poles.

The total number of turns of the stator windings N is calculated by assuming a proper value for the EMF per turn E_{pt}. In the design of this machine, it has been iteratively determined. The value of the best performance is selected. The total number of turns will be:

$$N = \frac{E_{rms}}{E_{pt}} \tag{3.7}$$

The number of turns per slot and the cross sectional area of the used conductor are needed to determine the area of the slot. The detailed dimensions of the slot, the width W_{slot} and the length L_{slot}, can be determined if the value of the slot conductor layers is known. The optimal value of the slot conductor layers corresponding to the best machine performance is found iteratively.

The width of the tooth W_{tooth} can be assumed to equal to the width of the slot W_{slot} multiplied by a certain factor K_{ts} as follows:

$$W_{tooth} = K_{ts} W_{slot} \tag{3.8}$$

where K_{ts}: the ratio between the width of the tooth to that of the slot. K_{ts} is considered as an iterative incremental variable. The value of this factor that gives the best performance of the machine is taken keeping in mind that the tooth flux density B_t must not saturate, i.e. it should be lower than 1.8T. The inner radius of the stator r_s will be (see Figure 3.1):

$$r_s = \frac{p(W_{slot} + W_{tooth})}{2\pi} - h_{lip} - h_{slot} \tag{3.9}$$

The length of the permanent magnet in the direction of magnetization l_M can be preliminarily determined using Eq. (2.17). The nearest standard permanent magnet dimensions available on the market should be chosen.

The height of the stator yoke h_{yoke} is determined by assuming a suitable value for the stator yoke flux density B_{yoke}. As the stator yoke flux density increases, the height of the stator decreases. Lower stator yoke height means shorter endwindings, which results into higher efficiency and lower cost and weight. On the other hand, as the stator yoke flux density increases, the iron losses (hysteresis and eddy current losses) increase and the efficiency decreases. Therefore, the stator yoke flux density is treated as an iterative incremental variable and the value of the best performance is selected under the constraint of a flux density lower than 1.8T.

Once the height of the stator yoke is determined, the outer radius of the machine r_o can be calculated from the following equation:

$$r_o = r_s + h_{lip} + h_{yoke} + 2h_{slot} \tag{3.10}$$

The slot opening S_o has two contradictory effects. As the slot opening increases, the loading effect decreases as the reluctance seen by the MMF of the load current increases. However, higher slot opening increases the cogging torque as the variation of the co-energy of the permanent magnets with respect to the rotor position increases [38], [39], [40] and [23]. The value of the slot opening that gives a reasonable performance for both of the cogging torque and loading effect should be selected

The cross sectional area of the conductor is determined by assuming a suitable current density J_c. The cross sectional area of the conductor is reduced by choosing a higher current density, which results into saving of copper material, thus resulting in a cheaper design and lighter machine. However, with higher current density the resistance of the windings will be comparatively higher, resulting into increased copper losses, thus reducing the efficiency and increasing the temperature rise of the machine. A reasonable current density J_c might be in the range of 4 up to $8A/mm^2$. The nearest standard cross sectional area of the conductor available on the market should be adopted.

To reduce the eddy current losses in the conductors and to reduce the resistance of each turn and thus to increase the efficiency of the machine, it is recommended to have each turn made from more than one conductor connected in parallel. The total cross sectional area of the conductor must be divided by the number of parallel pathes. So, every turn might have 2,3,4… conductors connected in parallel. The cross sectional area of the conductor A_c will be:

$$A_c = \frac{I}{m_c J_c} \tag{3.11}$$

where I : stator current.

m_c : number of conductors connected in parallel forming one turn.

J_c : current density of the stator conductors.

The active length of the machine l_{stk} is determined from the voltage equation Eq.(3.5) after rearranging:

$$l_{stk} = \frac{E_{rms}}{4.44 N B_M h_M f_{LKG}} \tag{3.12}$$

3.2 Losses calculations

Losses in permanent magnet machine include copper losses in the stator windings, iron losses in the stator, iron losses in the permanent magnets and rotor iron, additional or stray load losses and mechanical losses.

3.2.1 Copper losses

The copper losses P_{cu} of the machine can be calculated from the following equation:

$$P_{cu} = I^2 R \tag{3.13}$$

The resistance R is the resistance of the mean turn length l_{mt} multiplied by the number of turns N as follows:

$$R = N \frac{\rho_{cu} l_{mt}}{m_c A_c} \tag{3.14}$$

where ρ_{cu}: resistivity of copper. The resistivity of copper at $20^{O}C$ is $\rho_{20} = 1.724\times10^{-8}$ Ω.m. The resistivity at temperature T is:

$$\rho_T = \rho_{20}(1+\alpha_{20}(T-20)) \qquad (3.15)$$

where α_{20} is the copper temperature coefficient of resistivity at $20^{O}C$:

$\alpha_{20} = 3.8\times10^{-3}\ K^{-1}$.

The mean turn length l_{mt} equals:

$$l_{mt} = l_{stk} + l_c D_c \qquad (3.16)$$

where l_c: number of conductor layers in each slot.

D_c: diameter of the conductor.

3.2.2 Iron losses, [41]

The iron losses are of two types, eddy current and hysteresis losses. The iron losses can be calculated from the iron loss data provided by the manufacturer only if the losses are multiplied by empirical loss factors of the hysteresis and eddy current losses, k_{Hy} and k_{ed}, respectively. These empirical factors depend on the difference between the test conditions and the conditions in a real machine and they have different values for the yoke and the teeth. With a lamination thickness of 0.5mm, the approximate specific hysteresis and eddy current losses of the yoke are, respectively at 50 Hz and 1.5T:

$$p_{Hy} = 2.04 \text{ W/kg} \qquad (3.17)$$

$$p_{ed} = 0.76 \text{ W/kg} \qquad (3.18)$$

The core losses in the stator yoke at different frequencies and flux densities are:

$$P_{Hys} = k_{Hy} m_s p_{Hy} \left(\frac{f}{50Hz}\right)\left(\frac{B_{yoke}}{1.5T}\right)^2 \qquad (3.19)$$

where P_{Hys}: hysteresis yoke loss.

k_{Hy}: empirical hysteresis loss factor of the yoke equals 2.

m_s : stator yoke mass.

B_{yoke} : stator yoke flux density.

$$P_{eds} = k_{ed} m_s p_{ed} \left(\frac{f}{50Hz} \right)^2 \left(\frac{B_{yoke}}{1.5T} \right)^2 \qquad (3.20)$$

where P_{eds} : eddy current loss in the yoke.

k_{ed} : empirical eddy current loss factor of the yoke equals 1.8.

The core losses in the teeth at different frequencies and flux densities are:

$$P_{Hyt} = k_{Hyt} m_t p_{Hy} \left(\frac{f}{50Hz} \right) \left(\frac{B_t}{1.5T} \right)^2 \qquad (3.21)$$

where P_{Hyt} : hysteresis tooth loss.

k_{Hyt} : empirical hysteresis loss factor of the tooth equals 1.2.

m_t : tooth mass.

B_t : tooth flux density.

$$P_{edt} = k_{edt} m_t p_{ed} \left(\frac{f}{50Hz} \right)^2 \left(\frac{B_t}{1.5T} \right)^2 \qquad (3.22)$$

where P_{edt} : eddy current tooth loss.

k_{edt} : empirical eddy current loss factor of the tooth equals 2.5.

3.2.3 Magnet losses, [8]

The major rotor losses are the eddy current losses in the magnets due to flux harmonics. The flux harmonics originate from both the no load flux harmonics caused by the stator slots and the flux harmonics caused by the armature currents. The magnet losses can be expressed as:

$$P_{PM} = p_{PM} p h_M l_{stk} \qquad (3.23)$$

where P_{PM} : magnet losses.

p_{PM}: magnet specific losses assumed to be 300 W/m^2 for solid sintered permanent magnets. However, it should be lower for segmented magnets.

3.2.4 Additional losses, [4]

Additional losses (stray load losses) consist mainly of losses due to slot leakage flux and losses due to end leakage flux. They can be estimated to be 20% of the total iron losses as shown in the following equation:

$$P_{ad} = 0.2(P_{Hys} + P_{eds} + P_{Hyt} + P_{edt}) \qquad (3.24)$$

where P_{ad}: additional losses.

The windage and friction losses are assumed to be:

$$P_{wf} = 0.005P \qquad (3.25)$$

where P_{wf}: windage and friction losses.

P: rated power of the machine.

3.2.5 Efficiency

The efficiency η of the machine can be calculated from the following equation:

$$\eta = \frac{P_{out}}{P_{in}} = \frac{P_{out}}{P_{out} + P_{loss}} \qquad (3.26)$$

where P_{out}: output power of the machine, P_{in}: input power to the machine and P_{loss}: total losses of the machine.

3.2.6 Cost of active materials

The active materials of the machine are iron, copper and NdFeB permanent magnets. Their costs are given in Table 3.1 as a cost per unit weight. The cost of active material is dominated by that of the magnet.

Table 3.1: Cost of active material per unit weight

Material	Cost (EUR/kg)
NdFeB permanent magnets (sintered)	500
Copper	6
Iron	3

The cost of permanent magnets appearing in Table 3.1 is that of fully processed, corrosion coated with specific dimensions and already magnetized permanent magnets for the developed prototype (not mass production).

3.3 Preliminary design

The preliminary design is carried out using the previously mentioned analytical procedure to the single-phase electrical machine of the following specifications:

1) $1\,kW$ and 230V at 180rpm.
2) NdFeB permanent magnets with a remanent flux density $B_r = 1.41\,T$, coercivity H_c of about –700kA/m and maximum energy $(BH)_{\max}$ product of about 370kJ/m^3 at $60\,^oC$.
3) Number of slots = number of poles = 20.

The optimization process is done based on the following four variables:

1) The ratio between the width of the tooth to that of the slot K_{ts}.
2) The EMF per turn E_{pt} and thus the number of turns N.
3) The number of stator slot conductor layers l_c.
4) The stator yoke flux density B_{yoke}.

The aim of the optimization process is to specify the optimal values of these four variables that give:

1) Lower cost.
2) Higher efficiency.
3) Smaller size.

With the constraint of not exceeding a maximum flux density of about 1.8T in both the tooth and yoke of the stator.

The permeance coefficient PC is set to the typical value of 5. The leakage flux coefficient f_{LKG} is assumed to be 0.85. The current density J_c of the windings is approximated to 5 A/mm^2. The number of strands equals 2. Every variable of the four-mentioned optimizing variables are dealt separately and iteratively with the other three variables set to a constant value. The flow chart of Figure 3.2 demonstrates the optimization process. In the first trial, EMF per turn E_{pt} is taken as the optimizing variable, l_c is set to 2 layers, K_{ts} is set to 0.5 and B_{yoke} is set to 1.5T. Figure 3.3 shows the efficiency, cost of active material, tooth flux density and total machine diameter as function of E_{pt}. It can be concluded that 0.2V/turn gives the highest efficiency of about 83.1%, active material cost of about 1180€, tooth flux density of about 0.92T and a total machine diameter of about 0.565m.

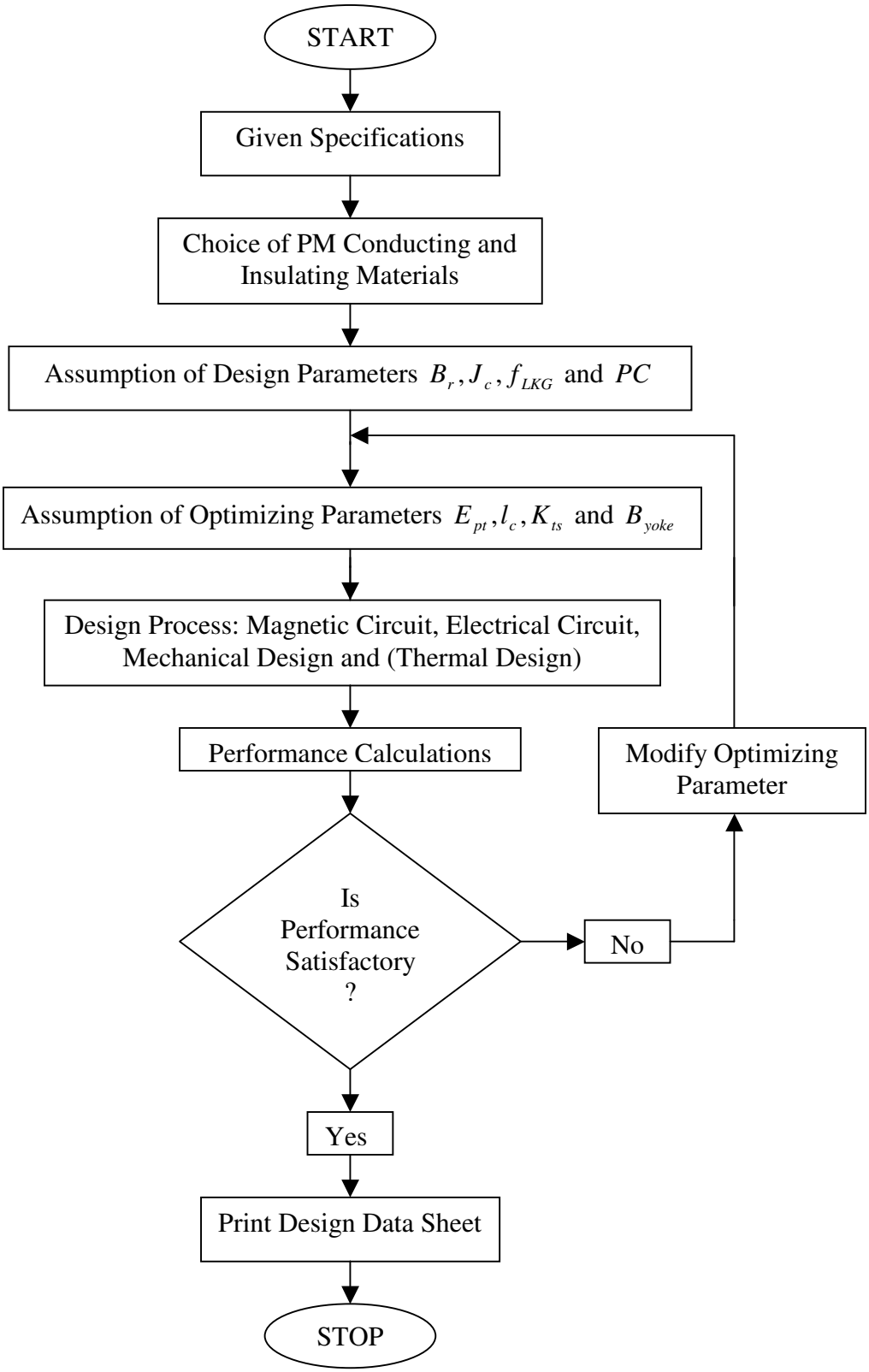

Figure 3.2: Optimization design flow chart

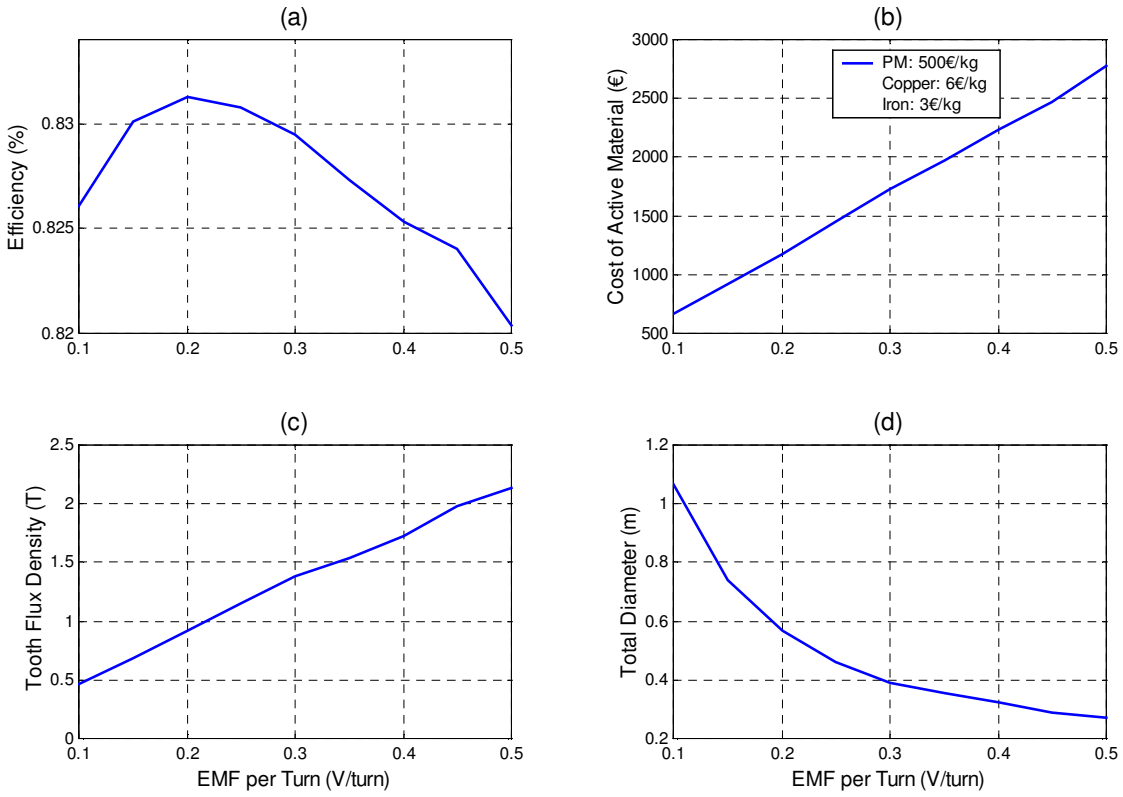

Figure 3.3: (a)Efficiency, (b)cost of active material, (c)tooth flux density and (d)total diameter as function of the EMF per turn E_{pt} with l_c =2 layers, K_{ts} =0.5 and B_{yoke} =1.5T

With E_{pt} set to its optimal value of 0.2V/turn the optimizing parameter, for the second trial, is the slot conductor layers l_c, with no changes on K_{ts} and B_{yoke}. Figure 3.4 shows the efficiency, cost of active material, tooth flux density and total diameter of the machine as function of l_c. It can be noted that 5 conductor layers per slot give the highest efficiency of about 83.8%, cost of active material of about 1161€, tooth flux density of about 2.13T (will be treated by the iteration of the next parameter) and a total diameter of about 0.28m.

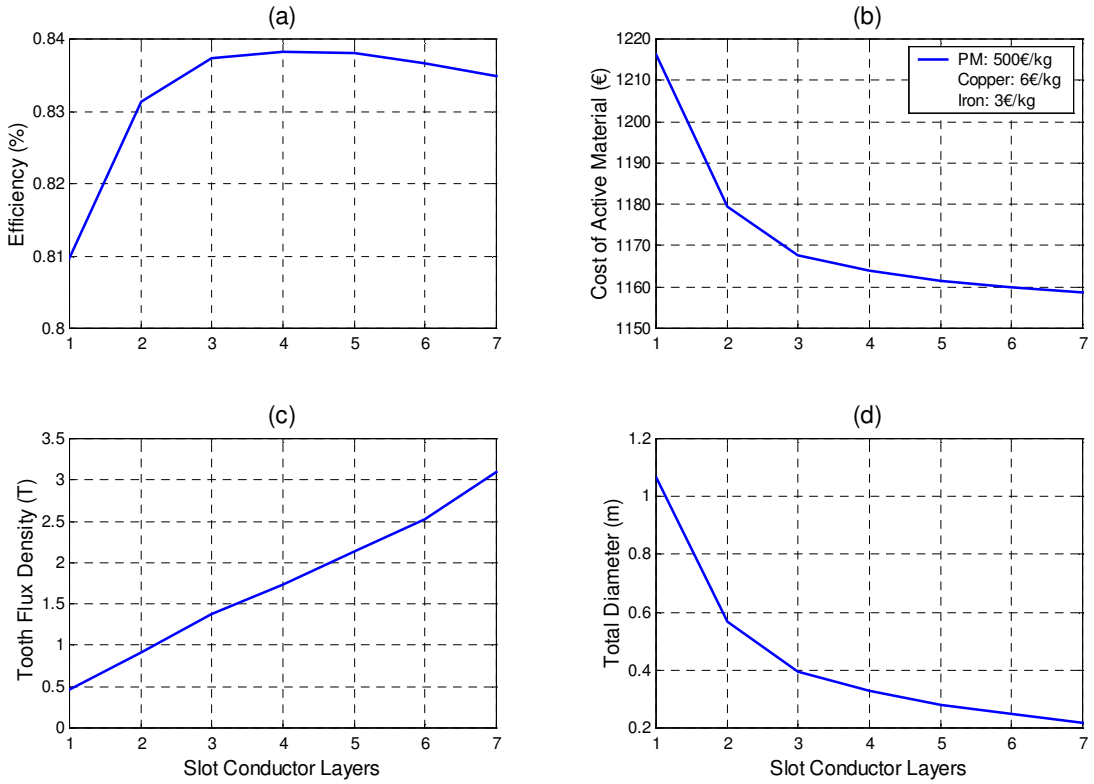

Figure 3.4: (a)Efficiency, (b)cost of active material, (c)tooth flux density and (d)total diameter as function of slot conductor layers l_c with E_{pt}=0.2V/turn, K_{ts}=0.5 and B_{yoke}=1.5T

In the third trial, the ratio between the width of the tooth to that of the slot K_{ts} is the optimizing parameter. It might vary from 0.1 up to 1. Figure 3.5 shows the efficiency, cost of active material, tooth flux density and the total diameter of the machine as function of the ratio between the width of the tooth to that of the slot. The value of the highest efficiency should not be chosen as the stator tooth flux density is saturated with 2T. A value of K_{ts}=0.6 gives an efficiency of about 83.7%, cost of active material of about 1163€, tooth flux density of about 1.78T and a total diameter of about 0.296m.

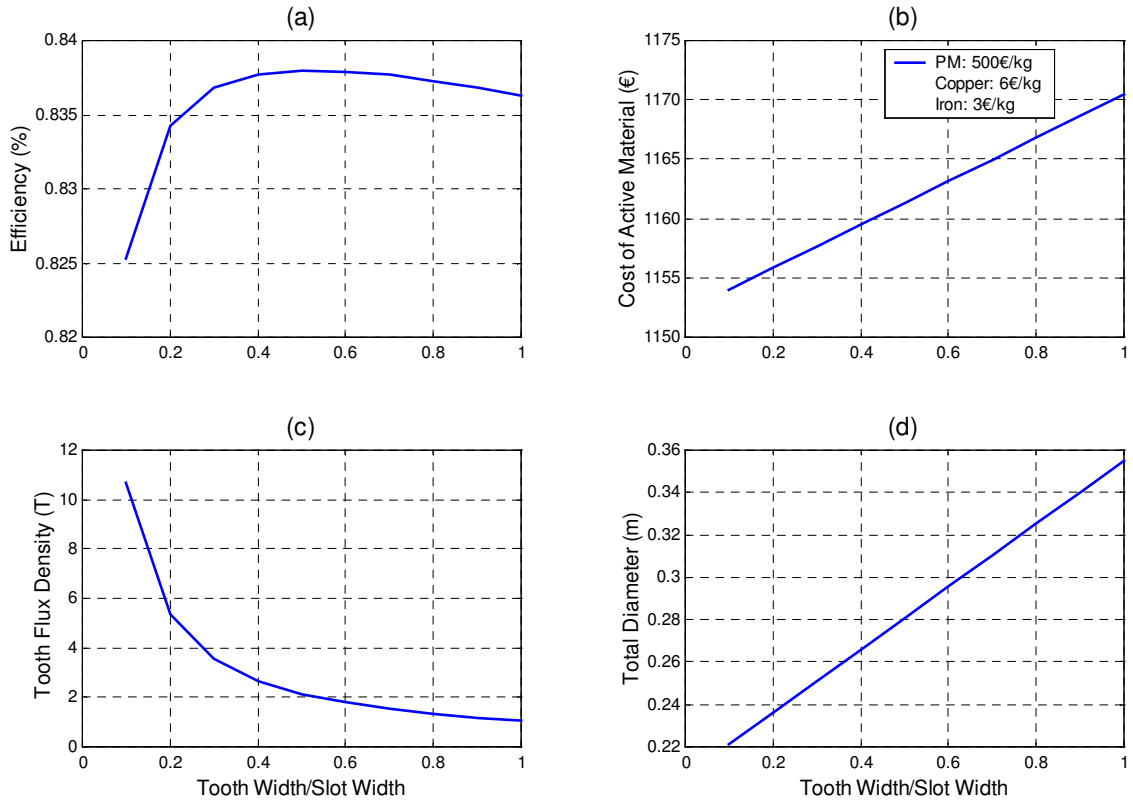

Figure 3.5: (a)Efficiency, (b)cost of active material, (c)tooth flux density and (d)total diameter as function of the ratio between the width of the tooth to that of the slot K_{ts} with E_{pt} =0.2V/turn, l_c =5 layers and B_{yoke} =1.5T

The variable parameter, in the fourth trial, is the stator yoke flux density B_{yoke} with the previously treated three parameters are set to the fixed optimizing values of E_{pt} =0.2V/turn, l_c =5 layers and K_{ts} =0.6. Figure 3.6 shows the efficiency, cost of active material, tooth flux density and the total diameter of the machine as function of the stator yoke flux density. A stator yoke flux density of about 1.5T yields an efficiency of about 83.7%, cost of active material of about 1163€, a constant tooth flux density of about 1.78T and a total diameter of about 0.296m.

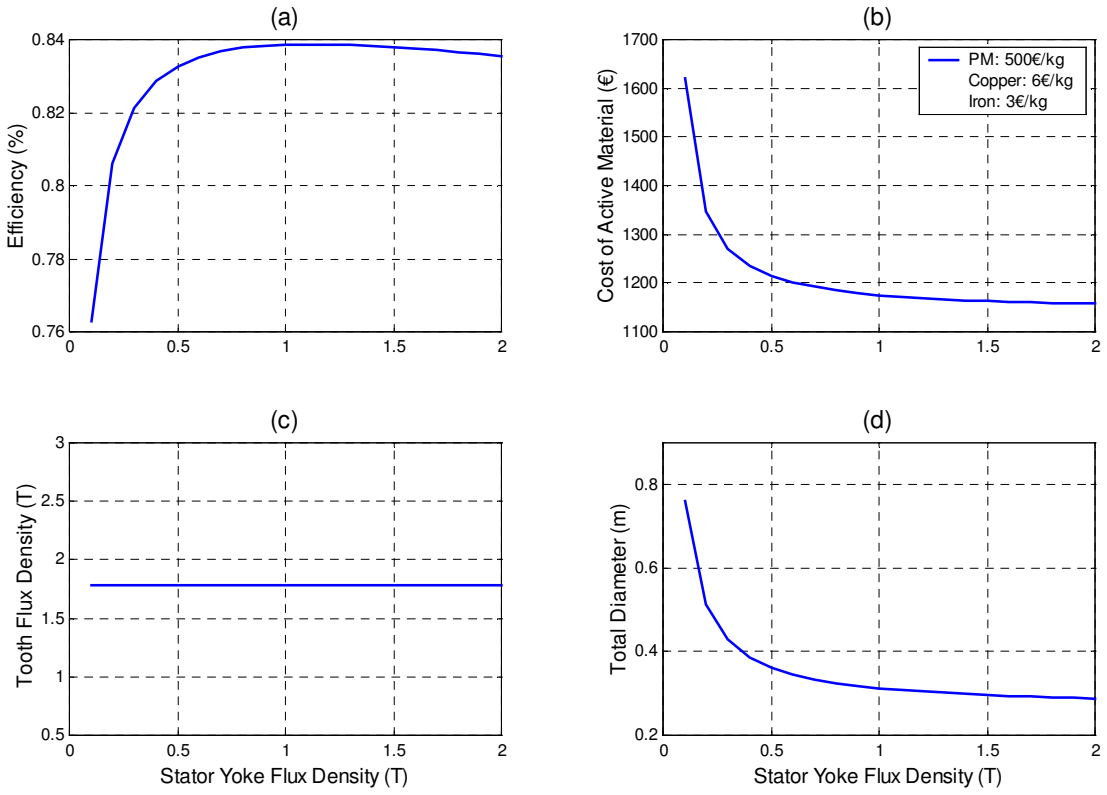

Figure 3.6: (a)Efficiency, (b)cost of active material, (c)tooth flux density and (d)total diameter as function of the stator yoke flux density B_{yoke} with E_{pt}=0.2V/turn, l_c=5 layers and K_{ts}=0.6

The optimal design parameters of the machine resulted from the preliminary design that will be the input parameters to the finite element package:

Inner radius of the stator $r_s = 119.1\,mm$.

Width of the slot W_{slot}=23.5 mm.

Height of the slot h_{slot}=6.1 mm.

Width of the tooth W_{tooth}=14.1 mm.

Height of the stator yoke h_{yoke}=8.3 mm.

Length of the permanent magnets in the direction of magnetization l_M=10 mm .

Height of the permanent magnet $h_M = 6\,mm$, (2 are used).

Active length of the machine $l_{stk} = 120\,mm$.

Air gap length $g = 1\,mm$.

Outer radius of the machine $r_o = 148\,mm$.

Table 3.2 shows the variation of the efficiency, cost of active material, tooth flux density and total diameter of the machine with the four successive trials.

Table 3.2: Efficiency η, cost of active material C_t, tooth flux density B_t and total diameter of the machine D_t resulting from the four successive trials

Trial No. **(Optimizing variables)**	**T1** **(E_{pt}=0.2, l_c=2, K_{ts}=0.5, B_{yoke}=1.5)**	**T2** **(E_{pt}=0.2, l_c=5, K_{ts}=0.5, B_{yoke}=1.5)**	**T3** **(E_{pt}=0.2, l_c=5, K_{ts}=0.6, B_{yoke}=1.5)**	**T4** **(E_{pt}=0.2, l_c=5, K_{ts}=0.6, B_{yoke}=1.5)**
η	0.831	0.838	0.837	0.837
C_t **(€)**	1180	1161	1163	1163
B_t **(T)**	0.92	2.13	1.78	1.78
D_t **(m)**	0.565	0.28	0.296	0.296

Chapter 4

Finite Element Analysis

In the forgoing design and linear analysis of the previous chapter, the prototype main dimensions are determined and its major performance is predicted. However, the permeability of the iron core is considered infinite or reluctance neglected and the main and leakage flux paths or permeance are assumed to only be affected by the geometry, not the MMF level of the magnets and armature [9]. Additionally, the teeth and yoke flux density variations are assumed constant and only the average value is estimated. To predict the performance of the machine accurately, finite element analysis is applied to the preliminary design obtained by the equivalent magnetic circuit linear approach. The major focus in the finite element design are magnetic flux distribution, linkage and leakage fluxes, the induced EMF, cogging torque and the possibility of demagnetizing the permanent magnet under abnormal conditions like short circuiting the electrical circuit. A software package developed at the Institute of Electrical Machines of TU-Berlin was used.

4.1 Introduction, [23]

The finite element technique is a numerical method for solving electromagnetic field problems, which are too complex to be solved using analytical techniques, especially those involving nonlinear material characteristics. The method basically involves the discretization of the machine cross-section (or volume in the case of 3-D analysis) into smaller areas/volumes called finite elements. The spatial variation of magnetic potential throughout the machine is described by a nonlinear partial differential equation derived from the Maxwell's equation. In its linear form this equation is Laplace's equation, Poisson's equation or the Helmholtz equation, depending on the type of problem being solved.

Usually the partial differential equation is written in terms of the magnetic vector potential $\vec{A}$, because of the economy with which important field quantities such as flux

density, flux,…etc can be subsequently determined. Accordingly the partial differential equation is solved, after discretization, in terms of the magnetic vector potential. Other output quantities are calculated from the nodal values of $\vec{A}$ in the postprocessing phase. The two-dimensional nonlinear magnetic vector potential equation used is:

$$\frac{\partial}{\partial x}\left(\frac{1}{\mu}\frac{\partial A_z(x,y)}{\partial x}\right)+\frac{\partial}{\partial y}\left(\frac{1}{\mu}\frac{\partial A_z(x,y)}{\partial y}\right)=-J_c-J_{PM} \qquad (4.1)$$

where A_z : magnetic vector potential in z-direction.

J_c : current density.

J_{PM} : magnitude of the equivalent current density at the magnet boundaries.

μ : permeability of the medium.

Within one element, the vector potential is assumed to vary accordingly to a simple shape function, which may be a linear, quadratic or higher order function of the three sets of node coordinates for the vertices of the triangular element. Linear elements give the fastest solution but the least smoothness in the field variation.

Application of the finite element method to machine design involves three stages:

1. Preprocessing.
2. Field solution.
3. Postprocessing.

4.1.1 Preprocessing

In most cases, this is the most user-intensive part of finite element analysis. Three tasks must be performed:

1. Mesh generation.
2. Material definition.
3. Problem definition.

Mesh generation involves division of the machine cross section into a set of triangular elements (2-D solution) or division of the machine volume into bricks (3-D solution). In

mesh generation, the coordinates required to define the machine geometry is calculated. The cross section is usually split up into regions representing different materials such as current carrying conductors, air, iron and magnets. Each region may define a different component used in the construction of the machine, for example, the shaft, rotor core, magnets, stator lamination, air gap…etc.

Material definition involves curve fitting of the nonlinear BH curve characteristics of the soft and hard magnetic materials used in the construction of the machine. Many finite element programs include databases of material data for the convenience of the user.

Problem definition involves the application of the correct boundary conditions, imposing the correct current densities in the appropriate winding elements and the definition of the direction of magnetization of the magnets. Periodic boundary conditions should be used if possible as they make it possible to model only a fraction of the cross section.

4.1.2 Field solution

The solution of the discretized partial differential equation uses specialized mathematical algorithms developed over many years. The algorithm is often based on the minimization of energy function, which is a mathematical function related to the stored potential energy in the field.

The discretization transforms the partial differential equation into a large number of simultaneous nonlinear algebraic equations containing the unknown node potentials. Iteration is essential and the Newton-Raphson and conjugate-gradient procedures are widely used. With linear elements, the potential is assumed to vary linearly between nodes and the flux density is constant within each element. Current density is also assumed to be constant within each element associated with a winding.

4.1.3 Post processing

The field solution is in terms of magnetic vector or scalar potential, but the design engineer needs quantities such as flux, flux density, force, torque, and magnetizing strength or may be co-energy. The extracting of these quantities from the potential solution is called post processing. A good interactive graphics facility is important so as the essential information and parameters can be extracted from the large number of node potentials effectively and quickly. Finite element analysis can be used to generate the following output:

a) Flux plots: these are especially useful for forming a picture of the flux. They can also be used for estimating leakage flux and calculating leakage permeances.
b) Flux calculation: the flux between two points of interest is calculated from the difference in vector potential at the two points, multiplied by the axial length. This calculation can be extended to obtain flux linkage, and hence inductance of windings.
c) Graphs of flux density variation: the required flux density component (radial or axial) can be plotted along a pre-determined path. For example, the variation in radial component of air gap flux density can be plotted around the rotor or may be around the internal surface of the stator to check the values of flux density in all points so as to be sure that local saturation does not exist.
d) Permanent magnet working point: The BH working point within each magnet element can be superimposed on the major BH curve of the magnet. This is useful for visualizing the effect of demagnetization.
e) Back EMF: finite element analysis can be performed for incremental rotor positions from which the variation of flux and flux linkage against rotor position can be obtained. This can be used to calculate the back EMF by differentiation with respect to the time.
f) Force and torque: force and torque are commonly calculated using the following three methods; Lorentz force, Maxwell stress and virtual work. All three methods are prone to errors. The best method depends upon the type of problem and the user's preferences.

For a two-dimensional model, the electromagnetic torque as function of the rotational angle $T(\theta)$ can be calculated using the Maxwell stress tensor method via the following equation:

$$T(\theta) = \frac{1}{\mu}\left[\int_{L} r.B_{rad}.B_{\tan} dL\right] \times l_{stk} \qquad (4.2)$$

where μ : permeability of the medium, L : integration contour, r : radius, B_{rad} : radial flux density, $B_{\tan}$: tangential flux density and l_{stk} : active or stack length of the machine.

Moreover, the electromagnetic torque can be calculated by the principle of virtual work using the following equation:

$$T(\theta) = \frac{\partial W(\theta, i)}{\partial \theta}\Big|_{i=const.} \approx \frac{\partial W_{air-gap}(\theta, i)}{\partial \theta}\Big|_{i=const.} \qquad (4.3)$$

where W is the magnetostatic co-energy, θ is the rotational angle, i is the stator current and $W_{air-gap}$ is the magnetostatic air gap co-energy. Most of the co-energy change occurs in the air gap as the co-energy change in permanent magnets and iron is negligible.

4.2 Finite element analysis

Finite element program is written with the output of the preliminary design as input parameters. Some small modifications are carried out to overcome the inaccuracy of the assumed variables. Table 4.1 presents the design results obtained from the preliminary and FET investigations. The changes are very small in terms of few millimeters.

Table 4.1: Preliminary and FET results

	Preliminary Design	FET Design
r_s **(mm)**	119.1	130.0
W_{slot} **(mm)**	23.5	20.5
h_{slot} **(mm)**	6.1	7.0
W_{tooth} **(mm)**	14.1	14.3
h_{yoke} **(mm)**	8.3	8.0
l_M **(mm)**	10.0	10.0
h_M **(mm)**	12.0	12.0
l_{stk} **(mm)**	119.3	130.0
g **(mm)**	1.0	0.80
r_o **(mm)**	148	160.0

Figure 4.1 shows the arrangement of permanent magnets, stator and rotor iron, rotor support structure and windings of the prototype. Generally, all sharp points should be slightly smoothed by curving, because otherwise the high flux concentration of the permanent magnets might saturate them.

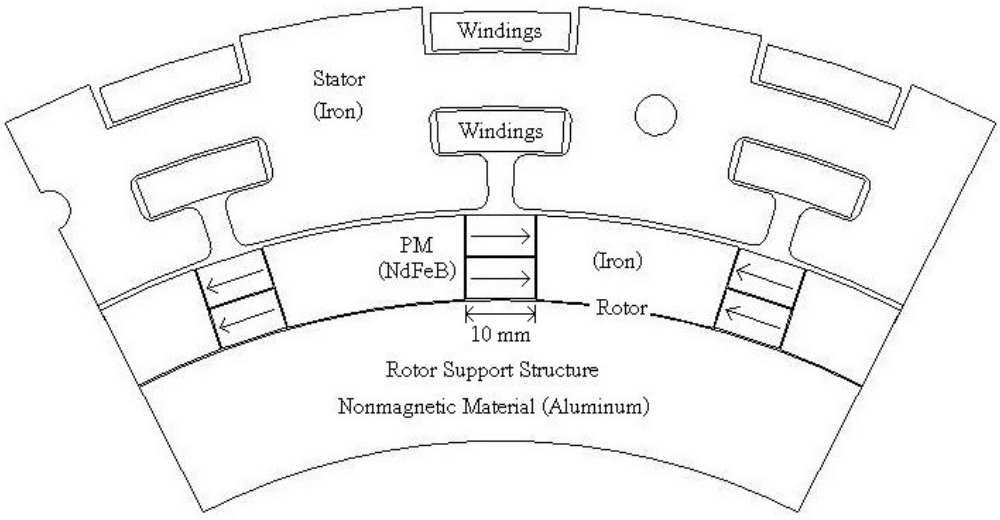

Figure 4.1: Arrangement of the active materials

The finite element mesh generated for three pole pitches is shown in Figure 4.2. The total number of elements is 10,000 with 5076 nodes. It is clear that the concentration of the elements and nodes is dense in the surfaces of the material changes. The flux lines distributions of the machine at no-load and full-load are shown in Figure 4.3 (a) and (b), respectively. As can be seen, in the no-load condition, the flux distribution is largely symmetric and the flux concentrations in the stator yoke, tooth and rotor iron is not too high. Leakage flux between the magnet poles is negligibly small. However, once the machine is loaded with a full load current, the flux slightly distorts and the leakage flux increases. Interestingly, there is no leakage flux across the slots.

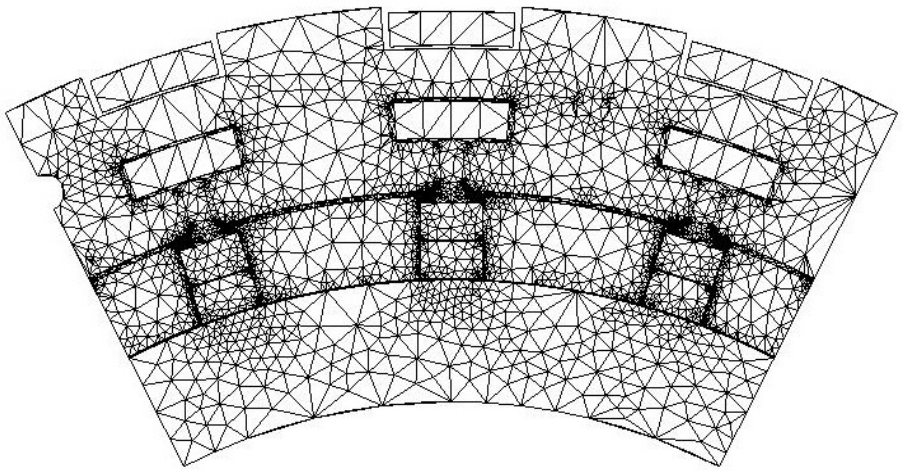

Figure 4.2: Finite element mesh for three pole pitches

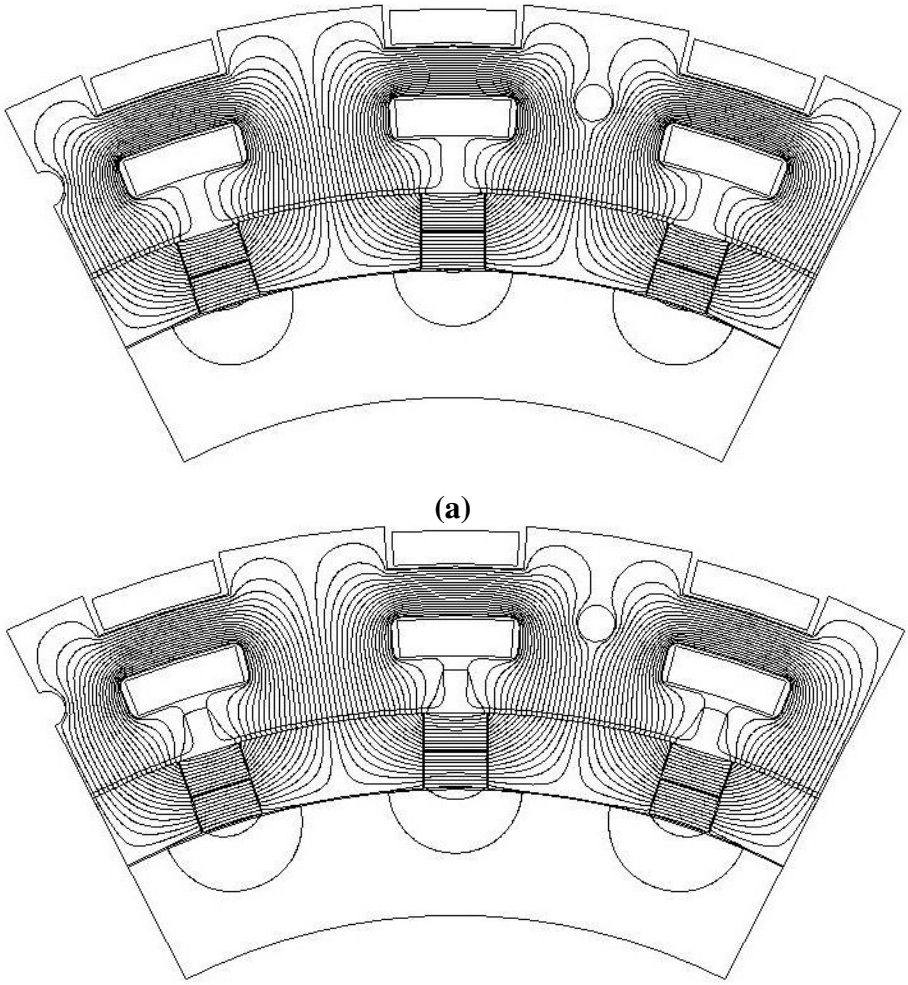

(a)

(b)

Figure 4.3: Flux lines distribution for three pole pitches (a) no load and (b) full load

Figure 4.4 shows the stator yoke flux density at no load. It varies linearly with the stator yoke height. The average flux density is about 1.55T. The optimal value obtained from the preliminary design was 1.5T. To take into account the effect of armature reaction, it is recommended to slightly increase the no-load yoke flux density. The maximum value of the flux ϕ_m will be:

$$\phi_m = B_{yoke} h_{yoke} l_{stk} = 1.55 * 8 \times 10^{-3} * 130 \times 10^{-3} = 1.61 \times 10^{-3} = 1.61 mWb.$$

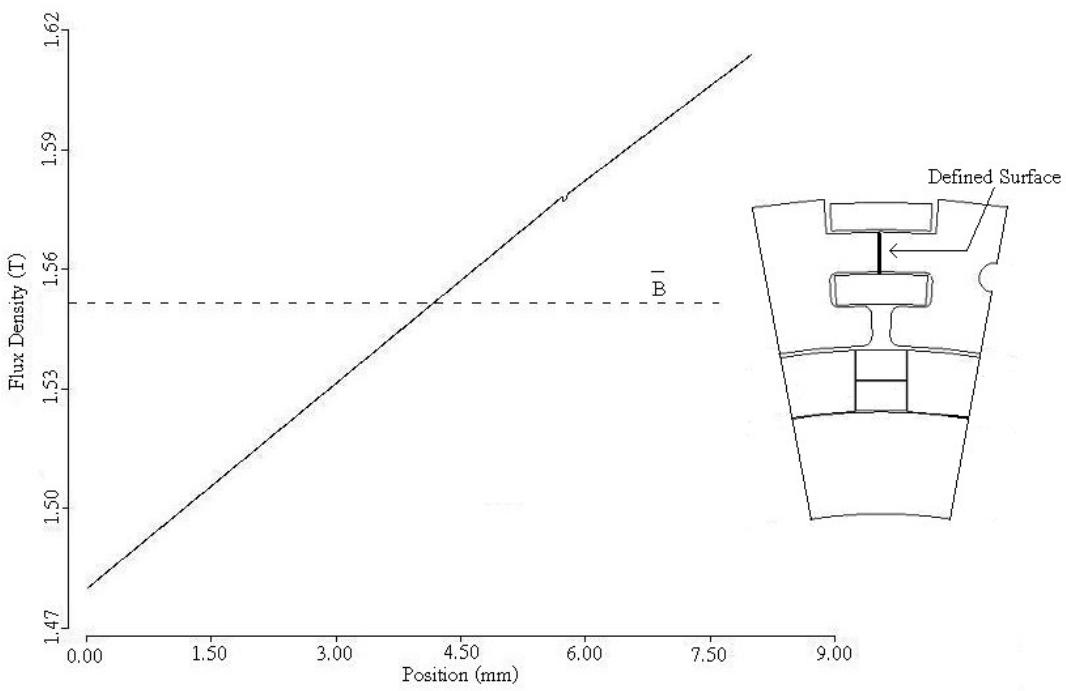

Figure 4.4: No-load stator yoke flux density

The stator yoke flux ϕ_m represents the linkage flux that penetrates from the permanent magnets through the air gap linking the stator windings. This part of the flux is the useful flux responsible for producing the voltage in case of generating mode of operation and torque in case of motor operational mode.

The leakage flux ϕ_l can be calculated as the difference between the permanent magnet flux ϕ_M and the linkage flux ϕ_m:

$$\phi_l = \phi_M - \phi_m$$

The permanent magnet flux ϕ_M can be calculated if the flux densities of the permanent magnets themselves are known. Figure 4.5 shows the flux density across a surface defined at the middle point of the upper and lower permanent magnets. The average flux densities of both magnets are about 1.14T. The total flux ϕ_M equals the sum of the two fluxes:

$\phi_{M-upper} = \phi_{M-lower} = 1.14 \times 6 \times 10^{-3} \times 130 \times 10^{-3} = 0.89 mWb.$

$$\phi_M = \phi_{M-upper} + \phi_{M-lower} = 0.89mWb + 0.89mWb = 1.78mWb$$

So, the leakage flux ϕ_l is:

$$\phi_l = \phi_M - \phi_m = 1.78mWb - 1.61mWb = 0.17mWb$$

and the leakage flux coefficient f_{LKG} will be:

$$f_{LKG} = \frac{\phi_m}{\phi_M} = \frac{1.61}{1.78} = 0.90 .$$

The rms value of the fundamental component of the no-load induced voltage E_{rms} at a speed of 180rpm will be:

$$E_{rms} = 4.44Nf\phi_m = 4.44 * 1200 * 30 * 1.61 \times 10^{-3} = 257.34V .$$

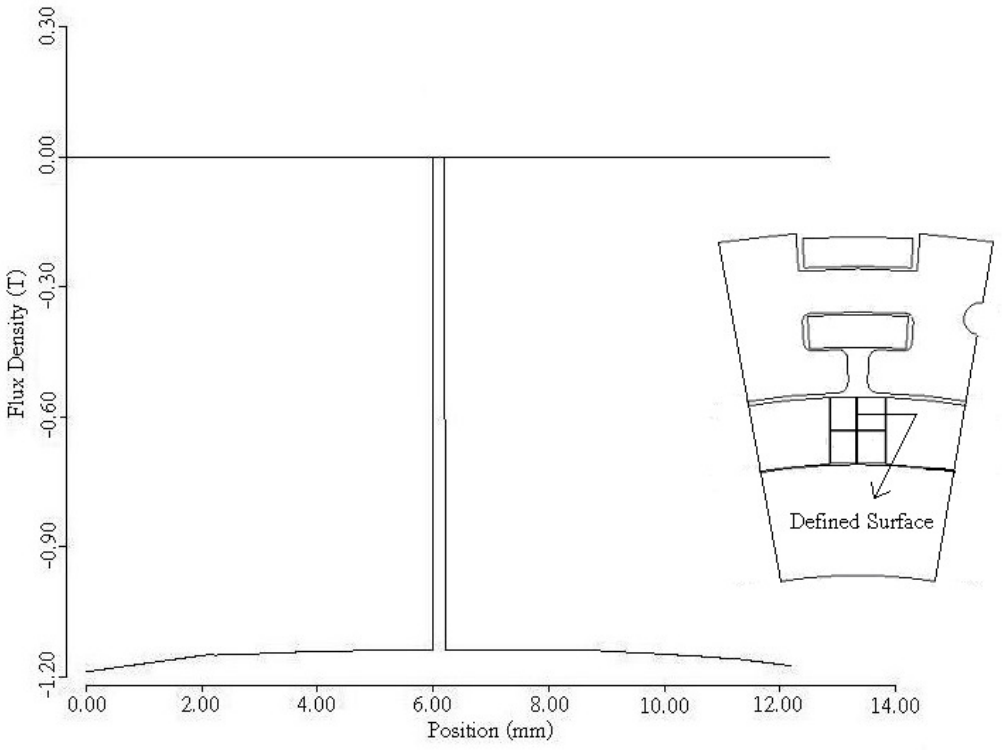

Figure 4.5: Flux density of the upper and lower permanent magnets on a surface defined vertically across their middle

Figure 4.6 shows the no-load air gap flux density distribution. The maximum value is about 0.73T. The air gap flux density must be chosen in such a way that there is no saturation in any part of the magnetic circuit. The value of operating flux density in the teeth and yoke increases with increased value of air gap flux density. Normally, flux densities of the teeth and yoke should not exceed 1.8T. Hysteresis and eddy current losses occurring in teeth and yoke are function of their flux densities. However, with higher value of air gap flux density size and cost of the machine are reduced for the same output.

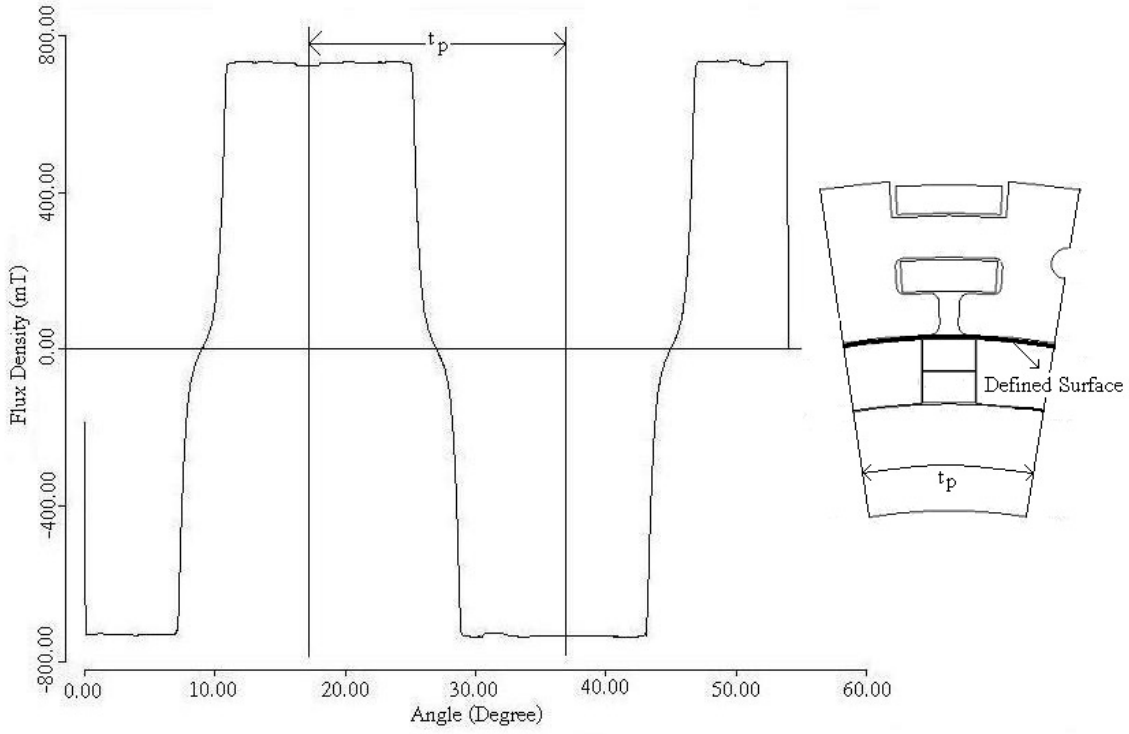

Figure 4.6: No-load air gap flux density distribution

The variations of the flux density across the inner surface of the slots, the outer surface of the slots and across a surface defined in the middle height of the slots are shown in Figures 4.7, 4.8 and 4.9, respectively. In all cases the maximum flux density takes place at the edges of the slots. Because the maximum value at each point is lower than the saturated value of 1.8T, the design is acceptable.

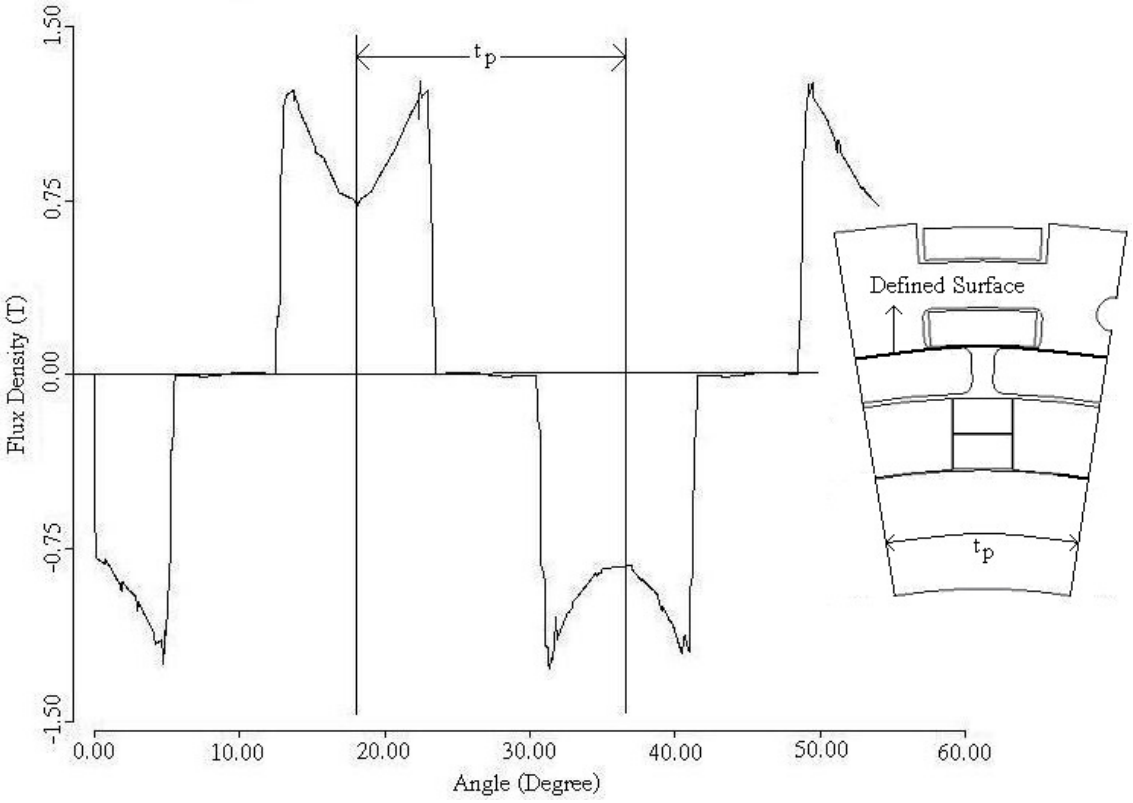

Figure 4.7: Flux density distribution across the inner surface of the slots

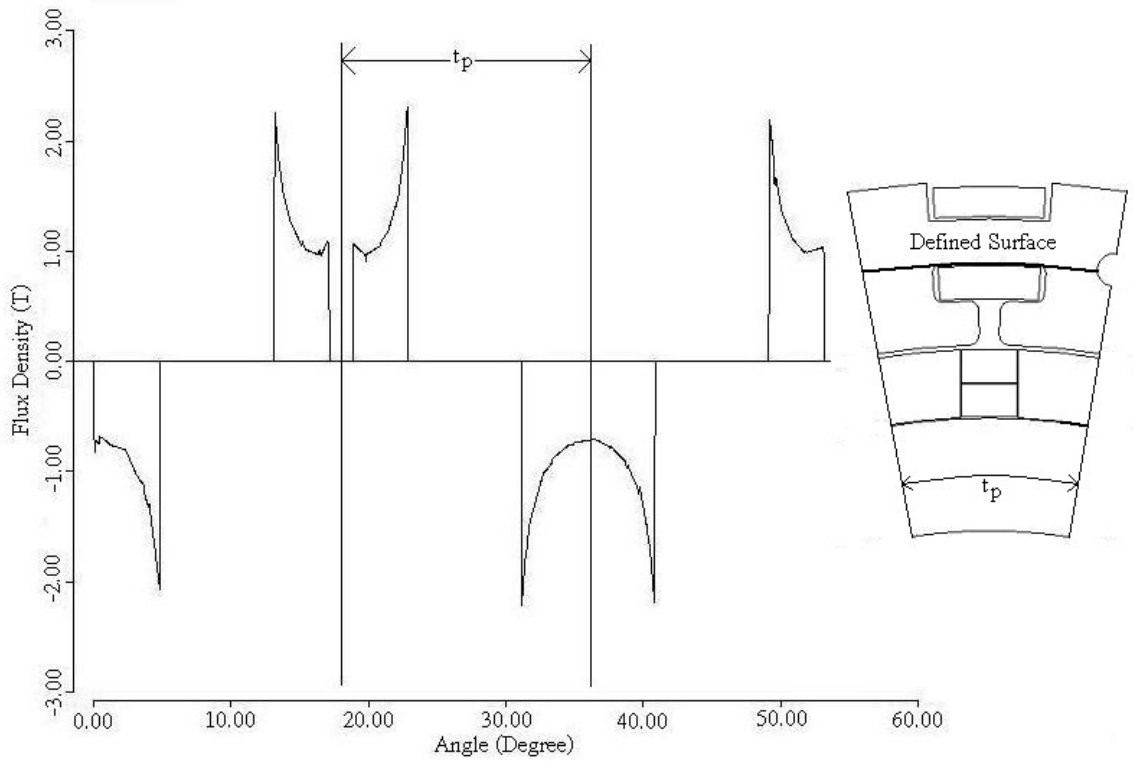

Figure 4.8: Flux density distribution across the outer surface of the slots

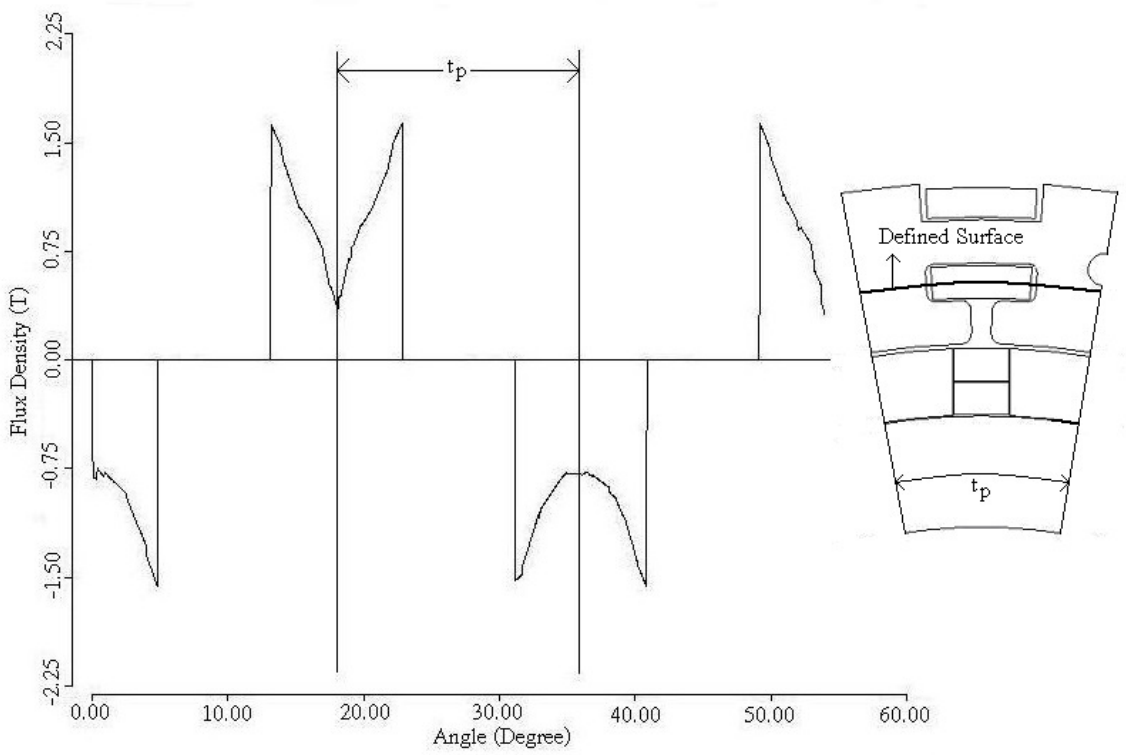

Figure 4.9: Flux density distribution across a surface defined in the middle of the slots

4.3 Cogging torque

4.3.1 The flux-MMF diagram, [25]

The cogging torque of the machine is predicted using the flux-MMF diagram. It is a generalized version of the flux-linkage versus current diagram used commonly for analyzing switched reluctance motors and relays. It plots the variation of instantaneous effective flux linking a particular phase against the instantaneous MMF in that phase. Both quantities are functions of the rotor position and the flux-MMF diagram is a closed trajectory over electrical cycle. Instantaneous as well as average torque at any given current can be calculated from the flux-MMF diagram by applying the principle of virtual work (see equation 4.3).

The total area enclosed by a flux-MMF diagram is fixed by its particular shape, and this area indicates the average torque produced over one electrical cycle for any one phase. The total area consists of a number of incremental areas bounded by the magnetization

curves at successive rotor positions and each of these areas indicates the instantaneous torque at a particular rotor position for any one phase. This makes it possible to calculate torque ripple at any given current.

Figure 4.10 shows a typical flux-MMF diagram for permanent magnet, which is constructed using a combination of flux-MMF data obtained from the finite element analysis and the demagnetization characteristics. Just as in the case of conventional flux-MMF diagram, finite element solutions are generated at incremental rotor positions over one cogging torque cycle. Using these solutions, values of total flux penetrating from the permanent magnet ϕ_M for any one pole are obtained at each rotor position. The corresponding permanent magnet MMF values are obtained using the demagnetization curve as in:

$$MMF = \frac{l_M}{\mu_o \mu_{rec}} \left(\frac{\phi_M}{A_M} - B_r \right) \tag{4.4}$$

where MMF : mmf of the permanent magnet.

l_M : length of the permanent magnet in the direction of magnetization.

ϕ_M : permanent magnet flux.

B_r : remanent flux density of the permanent magnet.

A_M : area of the magnet pole.

μ_o : permeability of free space.

μ_{rec} : recoil permeability of the permanent magnet.

Variation of flux is then plotted against the variation of MMF over one cogging torque cycle. This represents the flux-MMF diagram for a permanent magnet corresponding to any one pole, the triangle ABC in Figure 4.10. The load lines (the dashed lines inside the triangle ABC) are assumed to be linear. This is adequate in most cases except when there is high saturation in stator tooth tips or when the magnet working point is pushed beyond the knee point due to extremely high demagnetizing load currents, in which case, the load lines may be nonlinear.

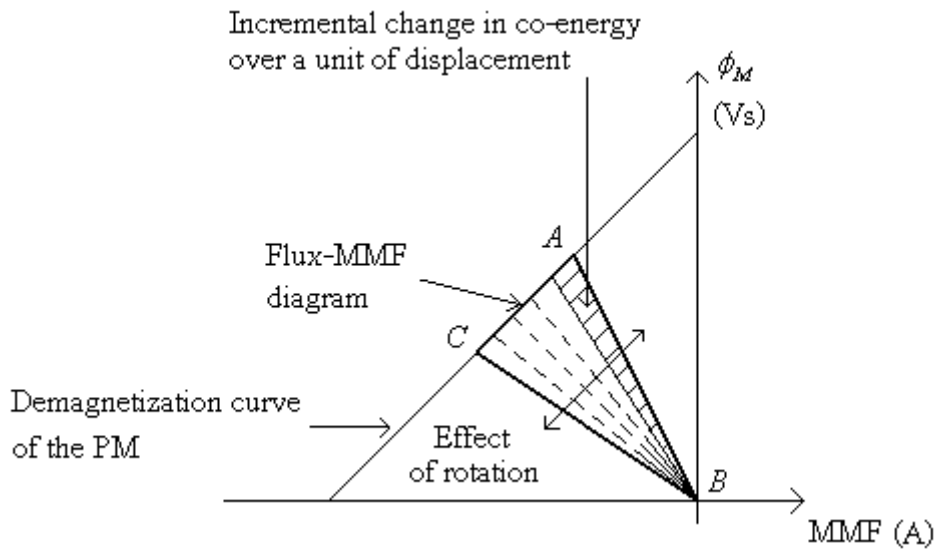

Figure 4.10: Schematic of the flux-MMF diagram of a permanent magnet

Once the flux-MMF diagram for any one pole is obtained, prediction of the cogging torque becomes an easy matter of calculating instantaneous torque for every incremental rotor position using the rate of change of co-energy with displacement as in Eq. (4.3). Even when no current is flowing, Eq. (4.3) can still be applied by replacing the current i with the MMF of the permanent magnet. Finally, total cogging torque is obtained simply by adding together the cogging torque of the individual poles.

4.3.2 Cogging torque study and optimization results

In this case, the rotor of the machine has the possibility of changing its position incrementally. The air gap has been divided into two equal parts. One of them is fixed to the stator and the other rotates with the rotor. The rotor can make a half pole pitch rotation. The second half pole pitch is concluded as the mirror image of the first one. All of the study is carried out at no load i.e. the stator current equals zero. The co-energy of the two permanent magnets is calculated from the finite element package itself for every incremental rotor position. The closest polynomial function representing the co-energy variation is found. The cogging torque is then calculated by differentiating this polynomial with respect to the angular displacement.

The effect of the width of the rotor iron pieces $W_{r,i}$ (see Figure 3.1) on the cogging torque is studied. The simulations are carried out three times with the rotor iron pieces widths equal to 0.5, 0.65 and 0.75 (maximum allowed width) of the pole pitch. The rotor iron pieces width that gives the lowest cogging torque is selected.

Figures 4.11, 4.12 and 4.13 show the no-load flux lines distribution of the machine at rotor rotational angles of 0, 3, 6 and 9 mechanical degrees with the ratio between the rotor iron pieces width and the pole pitch equals 0.5, 0.65 and 0.75, respectively. The co-energies of the permanent magnets that have been calculated by the finite element program are shown as function of the rotational angle in Figure 4.14(a) and the nearest polynomial function representing the co-energy variation is found. The corresponding cogging torque which is the differentiation of the co-energy function is shown in Figure 4.14(b). It is seen that the rotor iron width of 0.75 of the pole pitch (maximum allowed width) gives the lowest cogging torque with a peak value of about 2% of the rated torque of the machine. Interesting to be mentioned that this is easier from the assembling point of view.

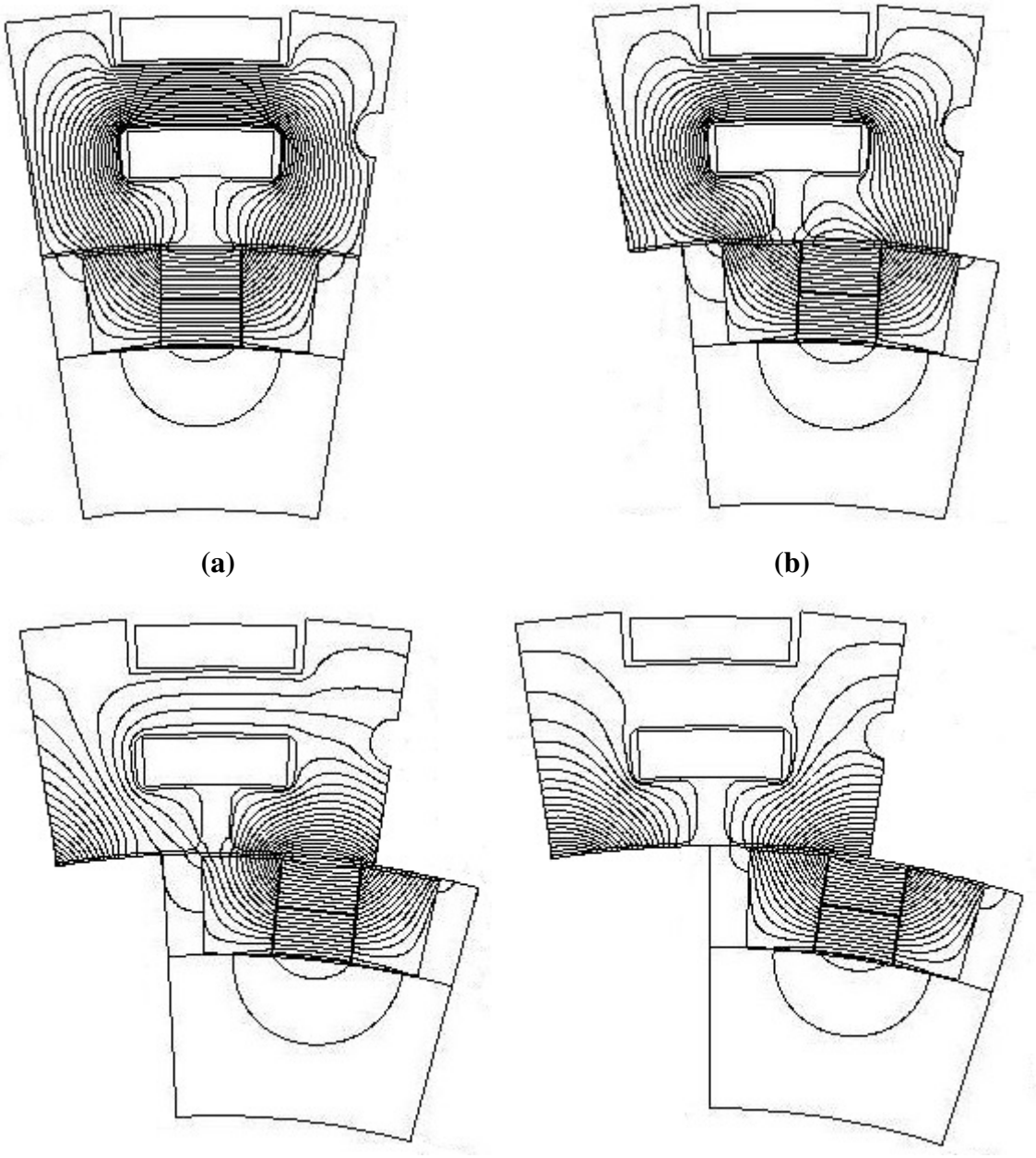

(a) **(b)**

(c) **(d)**

Figure 4.11: Flux lines distribution at no load with, (a) 0, (b) 3, (c) 6 and (d) 9 mechanical degrees rotor angles with the rotor iron pieces width equals 0.5 of the pole pitch

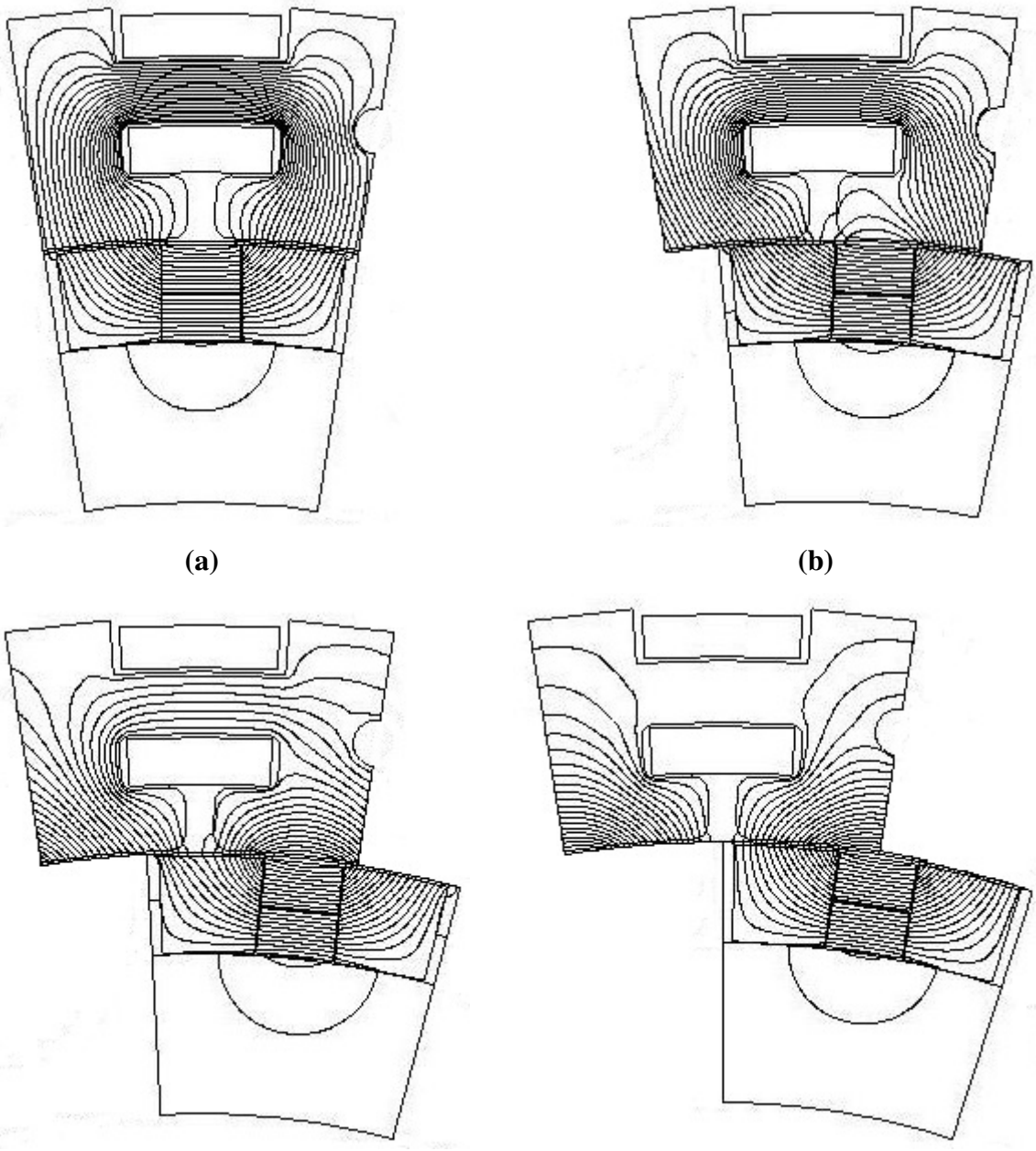

(a) **(b)**

(c) **(d)**

Figure 4.12: Flux lines distribution at no load with, (a) 0, (b) 3, (c) 6 and (d) 9 mechanical degrees rotor angles with the rotor iron pieces width equals 0.65 of the pole pitch

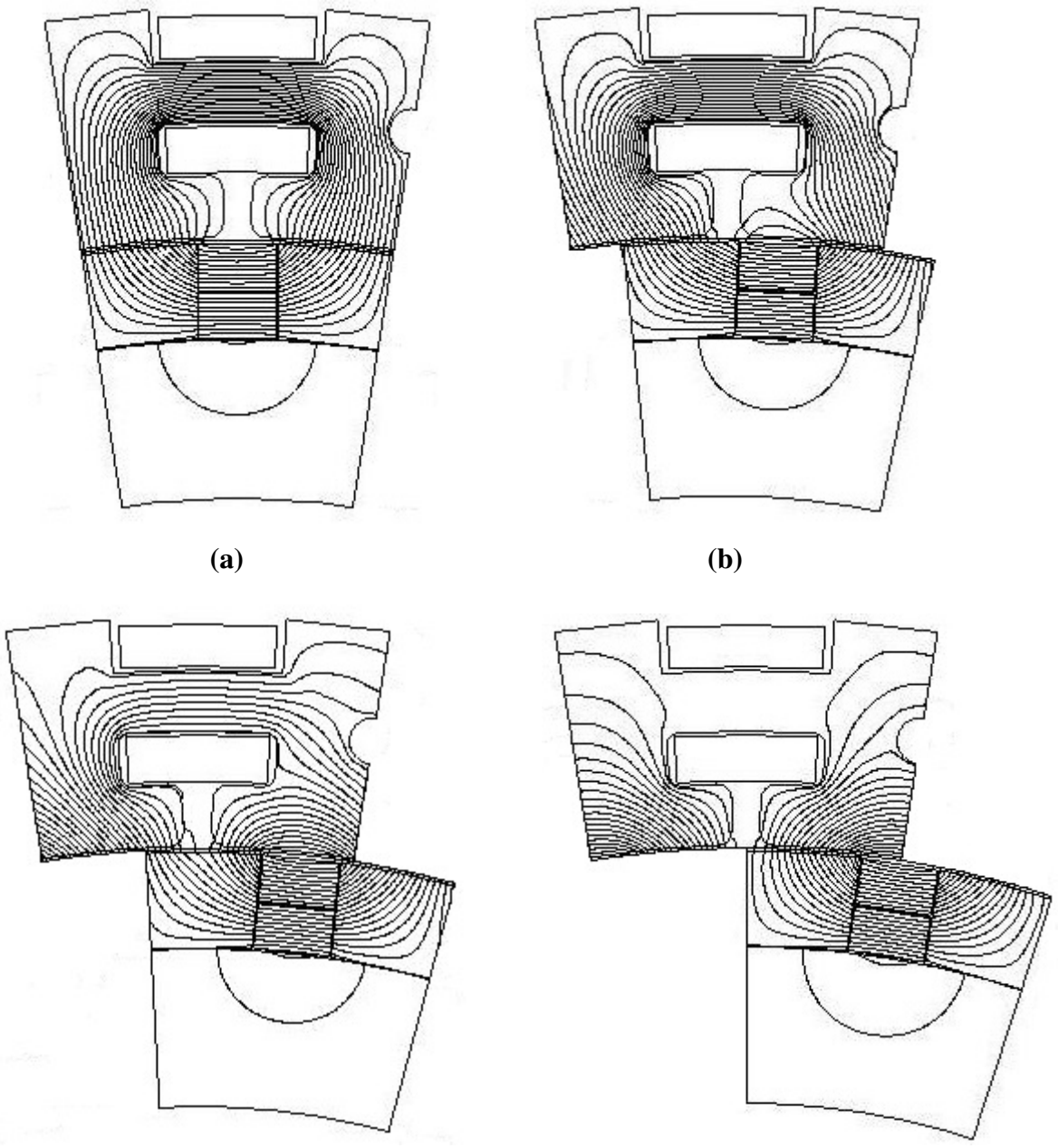

(a) **(b)**

(c) **(d)**

Figure 4.13: Flux lines distribution at no load with, (a) 0, (b) 3, (c) 6 and (d) 9 mechanical degrees rotor angles with the rotor iron pieces width equals 0.75 of the pole pitch (maximum possible length)

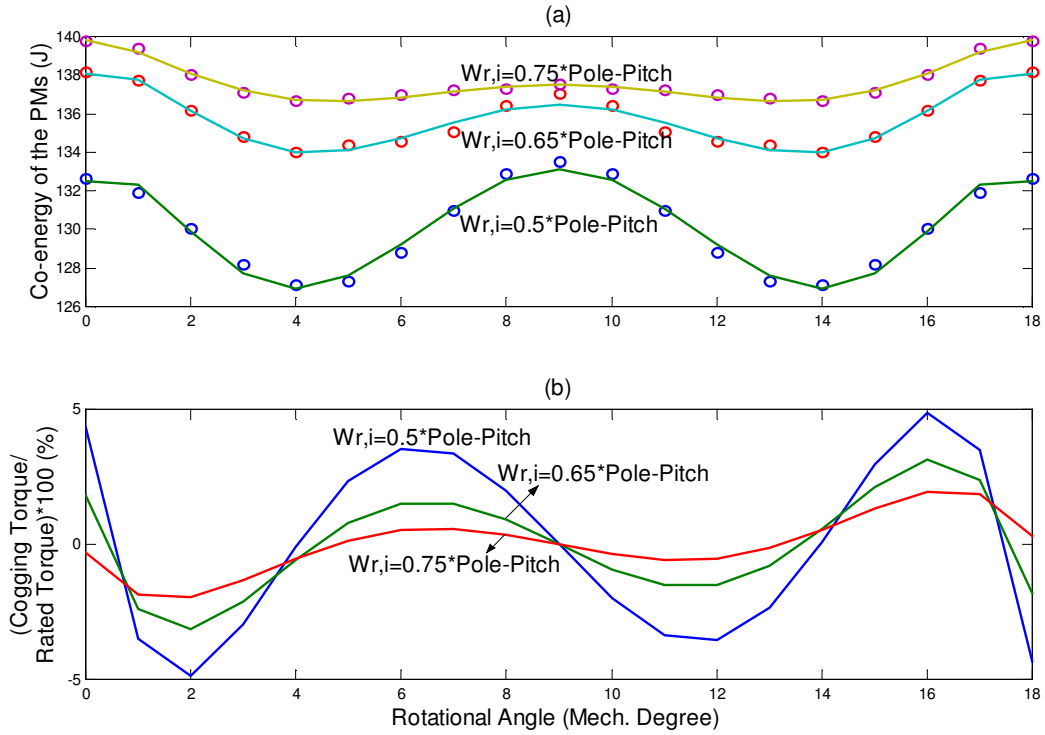

Figure 4.14: (a) Co-energy of the PMs of one pole pitch for three different rotor iron pieces widths at no load and (b) the corresponding cogging torque

4.4 Some mechanical considerations

The permanent magnets and the rotor iron pieces are glued on the surface of the rotor support structure. To increase the ruggedness of the rotor structure, screws are radially implemented to fix the iron pieces on the rotor support structure material. Additionally, a small protuberance of $1\times1\,mm$ is left on the upper face of the permanent magnets to completely diminish the probability of changing their position under the effect of centrifugal force. This new construction of the machine with the protuberance is shown in Figure 4.15 and the no-load flux lines distribution of the machine is shown in Figure 4.16. Apparently, this slight modification has not affected the electromagnetic design of the machine.

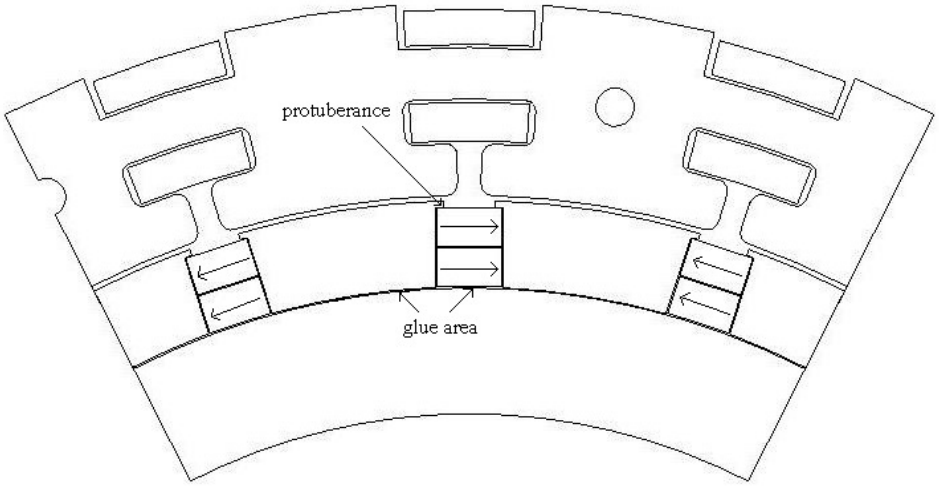

Figure 4.15: Construction of the machine with the protuberance over the permanent magnets

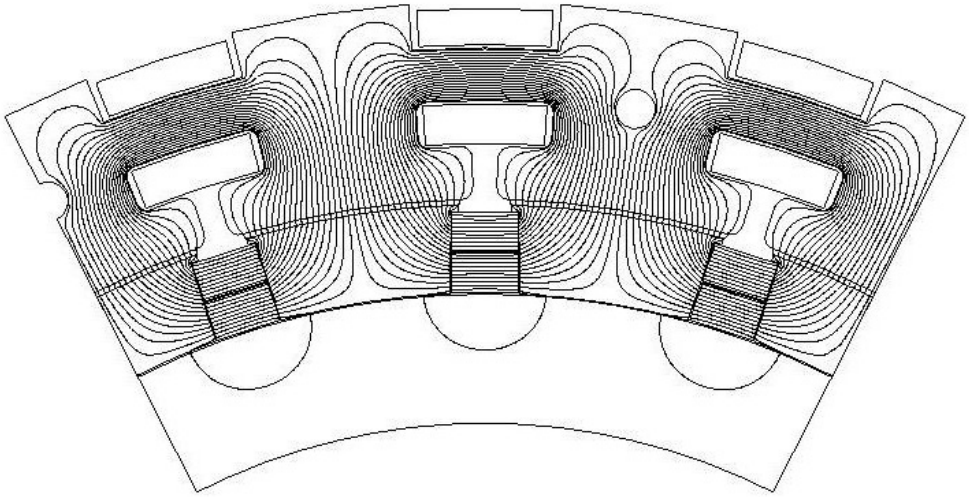

Figure 4.16: No-load flux lines distribution of the machine with the protuberance over the permanent magnets

Mathematically, the magnitude of the centrifugal force F is:

$$F = \frac{mv^2}{r} \qquad (4.5)$$

where m : mass of the rotating body.

v : tangential speed of the rotating body.

r : radius of the rotational path.

The tangential speed v can be expressed in terms of the angular rotational speed ω as:

$$v = r\omega \tag{4.6}$$

Substituting Eq. (4.6) in Eq. (4.5) yields,

$$F = mr\omega^2 \tag{4.7}$$

What is required is to calculate the centrifugal force acting on the permanent magnets and the shearing stress introduced on the protuberances. For a safe design, the shearing stress of the iron protuberance must be much higher than the mechanical stress caused by the magnets.

Eq. (4.7) can be written as:

$$F = \rho_M V_M r\left(\frac{2.\pi.n}{60}\right)^2 \tag{4.8}$$

where ρ_M: density of the permanent magnets, V_M: volume of the permanent magnets and n: rotational speed in rpm.

The volume of the permanent magnets can be straight forwardly expressed in terms of their dimensions. Therefore, Eq. (4.8) can be rewritten as:

$$F = \rho_M l_M h_M l_{stk} r\left(\frac{2.\pi.n}{60}\right)^2 \tag{4.9}$$

Numerically, ρ_M =7200-7500kg/m^3 [2], l_M =10mm, h_M =6mm, l_{stk} = 130mm, r_{upper} =126mm, r_{lower} =120mm. With a rotational speed of 500rpm (the rated speed is 180rpm), the centrifugal force on the upper permanent magnet is F_{upper} = 19.8N and the centrifugal force on the lower permanent magnet is F_{lower} = 18.8N. Therefore, the total force will be F =38.6N. Thus, the mechanical stress of the permanent magnets σ_M acting on each protuberance is:

$$\sigma_M = \frac{F}{2A_p} \tag{4.10}$$

where σ_M : mechanical stress caused by the permanent magnets.

A_p : area of the protuberance.

The value of σ_M at a speed of 500rpm will be $0.03\times10^7\ \mathrm{N}/m^2$. The shearing stress of the iron is $12\times10^7\ N/m^2$ [43]. It is about 400 times the stress caused by the magnets.

4.5 Loading effect

The stator current produces a magnetic flux in the stator yoke that may weaken or enhance the magnetic flux produced originally by the permanent magnets. As a result, the internal generated voltage of the machine changes. This is, in fact, similar to what is called "armature reaction" in DC machines. As a matter of fact, the value of the magnetic flux produced by the stator current depends on the reluctance of the magnetic circuit seen by the MMF of the stator currents, while the direction of the flux depends on the power factor of the load. It is known that unity and lagging power factor loads produce fluxes that weaken the main flux, while leading power factor loads enhance the main flux. One possible way to reduce the loading effect is by increasing the slot opening. However, higher slot opening increases the cogging torque as the magnetic reluctance variations seen by the permanent magnets as function of the rotor position increase. The flux lines distribution of the machine with the rated stator current acting alone (i.e. the permanent magnets remanent flux density is set to zero) is shown in Figure 4.17 and the corresponding stator yoke flux density is shown in Figure 4.18. It can be noticed that the average flux density of the stator yoke due to the rated stator current acting alone is about 0.136T which is 8.8% of the no load stator yoke flux density caused by the magnets alone.

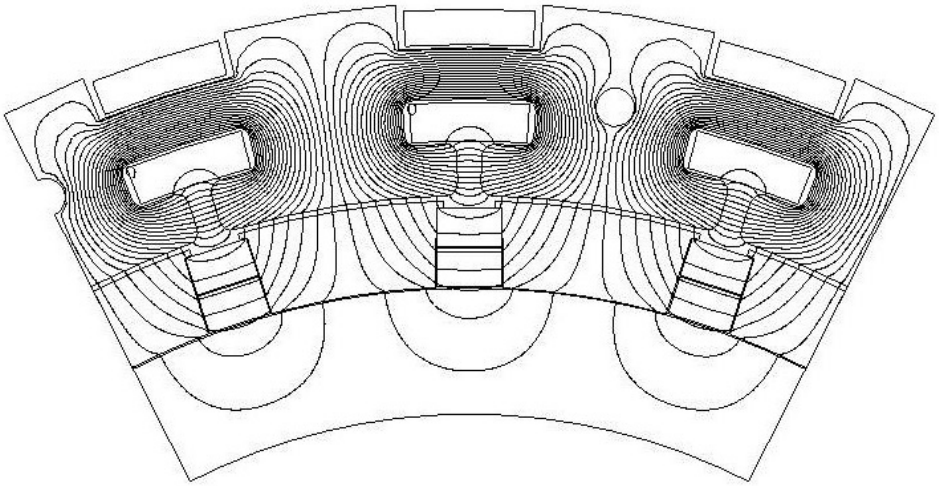

Figure 4.17: Flux lines distribution with the rated stator current MMF acting alone (remanent flux density B_r =0)

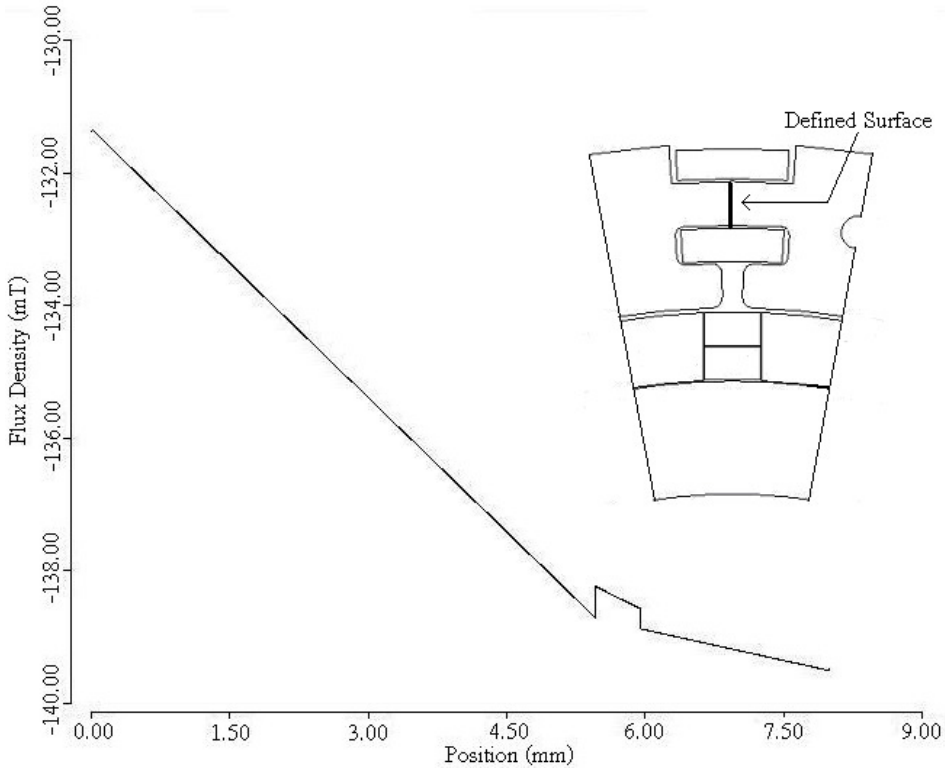

Figure 4.18: Stator yoke flux density with the rated stator MMF acting alone

The prime interest issue in the loading effect in permanent magnet machines is the possibility of partially or totally demagnetizing the magnets. In normal operating

conditions the magnet thickness and coercivity are sufficiently large and there should be no risk of demagnetization. However, abnormal operating conditions, like short circuit current, that has a value many times larger than the rated current should be studied. It is important to estimate the worst demagnetizing case in the magnet. Figure 4.19 shows the flux lines distribution with a stator current equals six times the rated current while Figures 4.20 and 4.21 show the magnetic field strength inside the upper and lower permanent magnets, respectively. It can be noticed that the demagnetizing strength of the upper permanent magnet varies from about 98kA/m up to 147kA/m and for the lower permanent magnet from about 82kA/m up to 99kA/m. Obviously, they are much lower than the coercivity of the magnets, which is 1100kA/m at a temperature of $20^{o}C$ and 700kA/m at a temperature of $60^{o}C$.

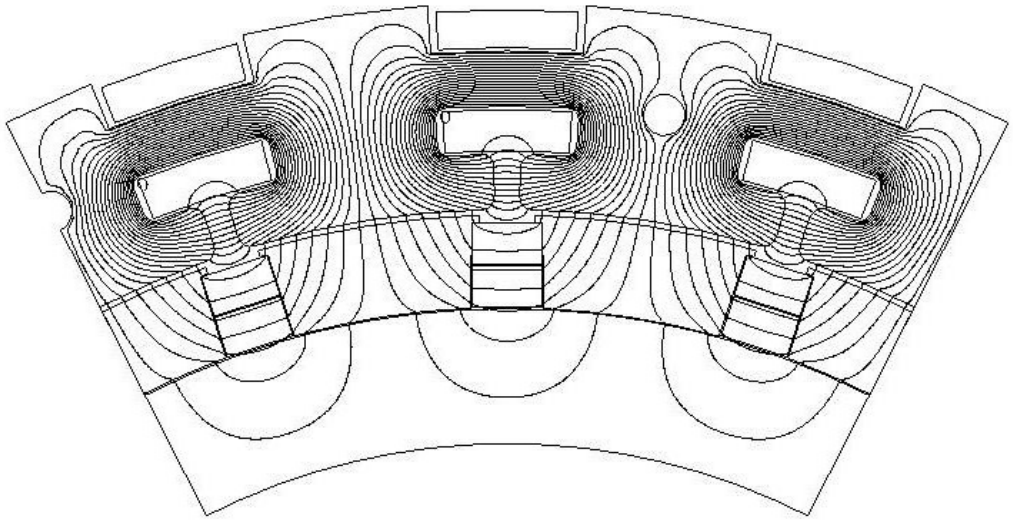

Figure 4.19: Flux lines distribution with a stator current equals six times the rated current

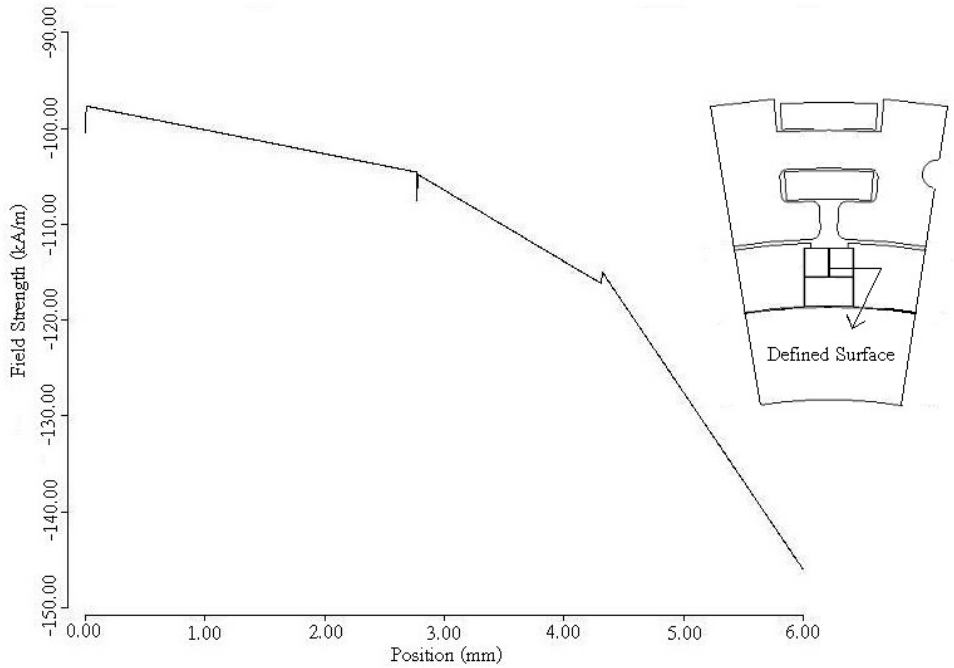

Figure 4.20: Magnetic field strength inside the upper permanent magnet with a stator current equals six times the rated current

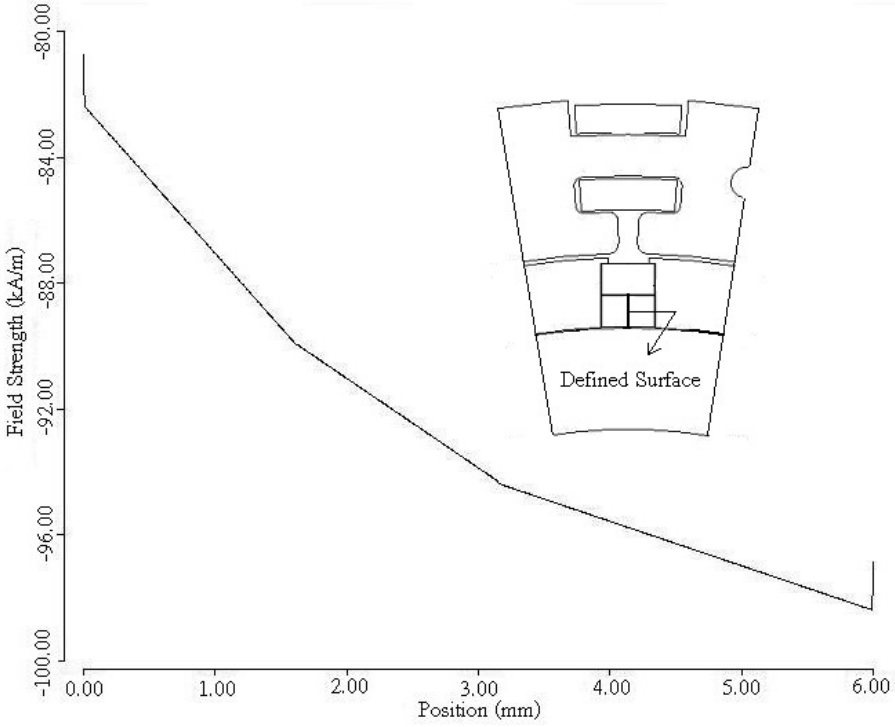

Figure 4.21: Magnetic field strength inside the lower permanent magnet with a stator current equals six times the rated current

Chapter 5

Construction, Material and Technology

The prototype machine was manufactured at the Institute of Energy and Automation Technology. The stator and rotor were fixed by two end parallel shields and one base Aluminum plates. A shaft with proper dimensions was fabricated. The stator consists of slotted iron laminations. The windings are toroidal (torus) and mounted inside flat slots. The rotor consists of permanent magnets, iron pieces attached to both poles of the magnets, rotor support structure made from light material that must be nonmagnetic and a shaft. The following sections of this chapter investigate the prototype construction, material, technology and their specifications.

5.1 Stator

The stator consists mainly of laminations and windings. The laminations were cut using laser technology with an accuracy of ± 0.01mm. Each lamination has a thickness of 0.66mm and a weight of 104g. A picture of a lamination is shown in Figure 5.1. The windings are of toroidal (torus) type. Toroidal type is chosen due to its simplicity, compactness, ease of arrangement and above all their shortends that reduce the resistance and hence improve the efficiency of the machine, reduce the weight of active material and as a result improve the power to weight ratio and reduce the cost of active material. To further reduce the total winding resistance and hence to improve the efficiency of the machine, every winding has been made from two separate coils connected in parallel. All windings are connected in series such that their induced EMFs are added. Their arrangement is shown in Figure 5.2 where the beginning of the i^{th} winding is connected to the beginning of the $i^{th}+1$ winding and similarly for the ends. Figure 5.3 shows the stator fixed on one Aluminum end shield together with the windings.

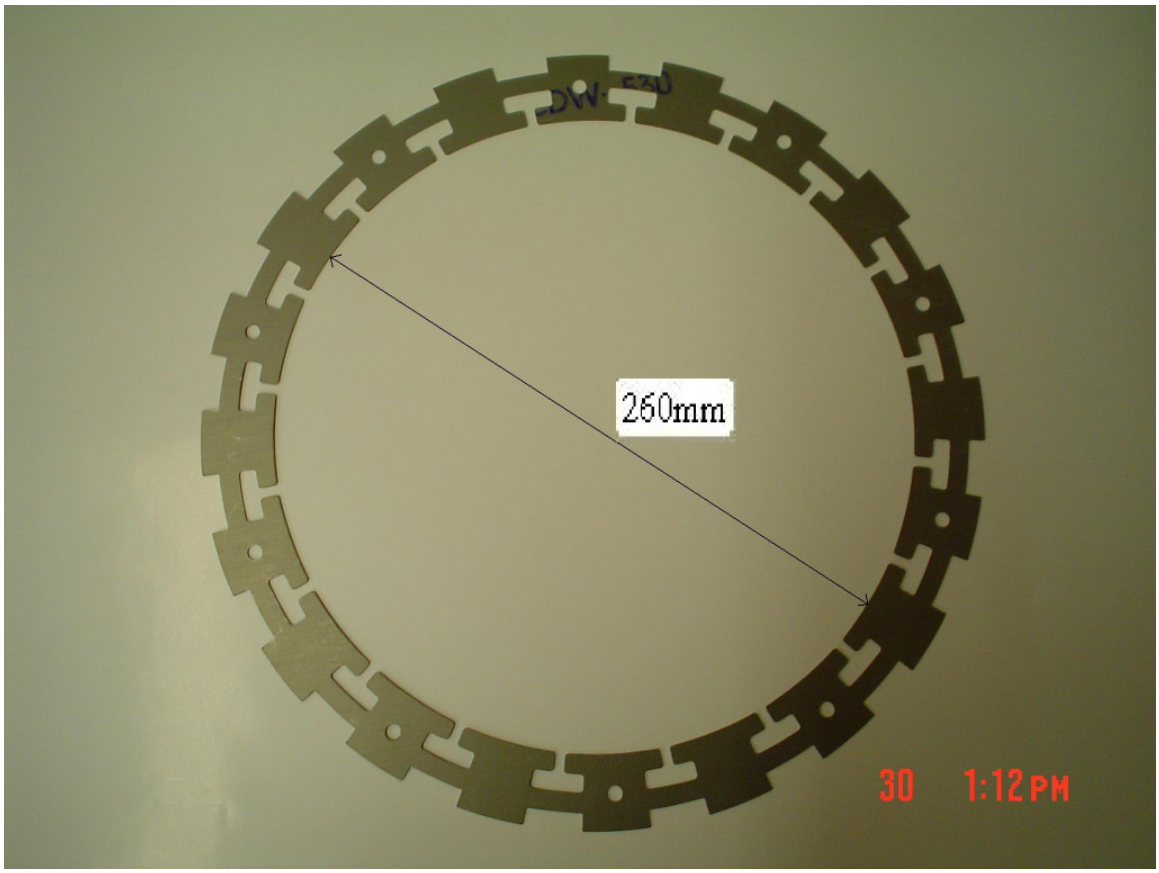

Figure 5.1: Stator lamination of the prototype

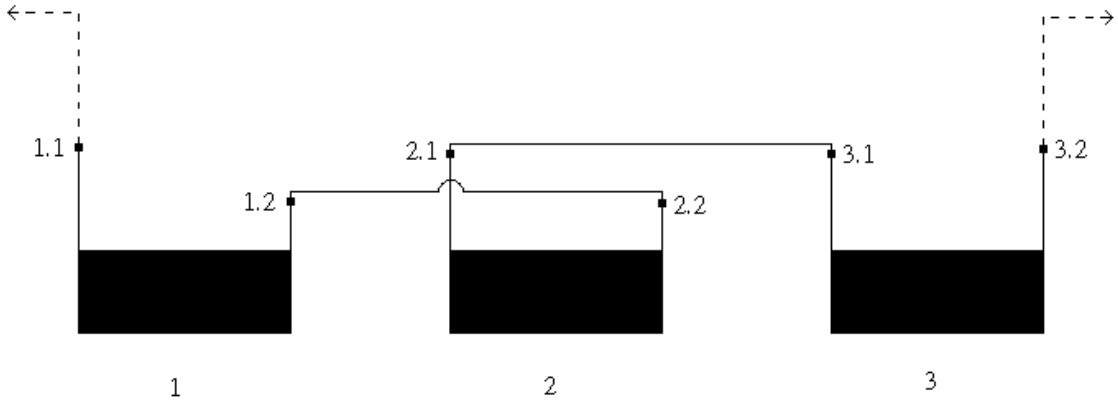

Figure 5.2: Winding arrangement (two parallel coils for every winding)

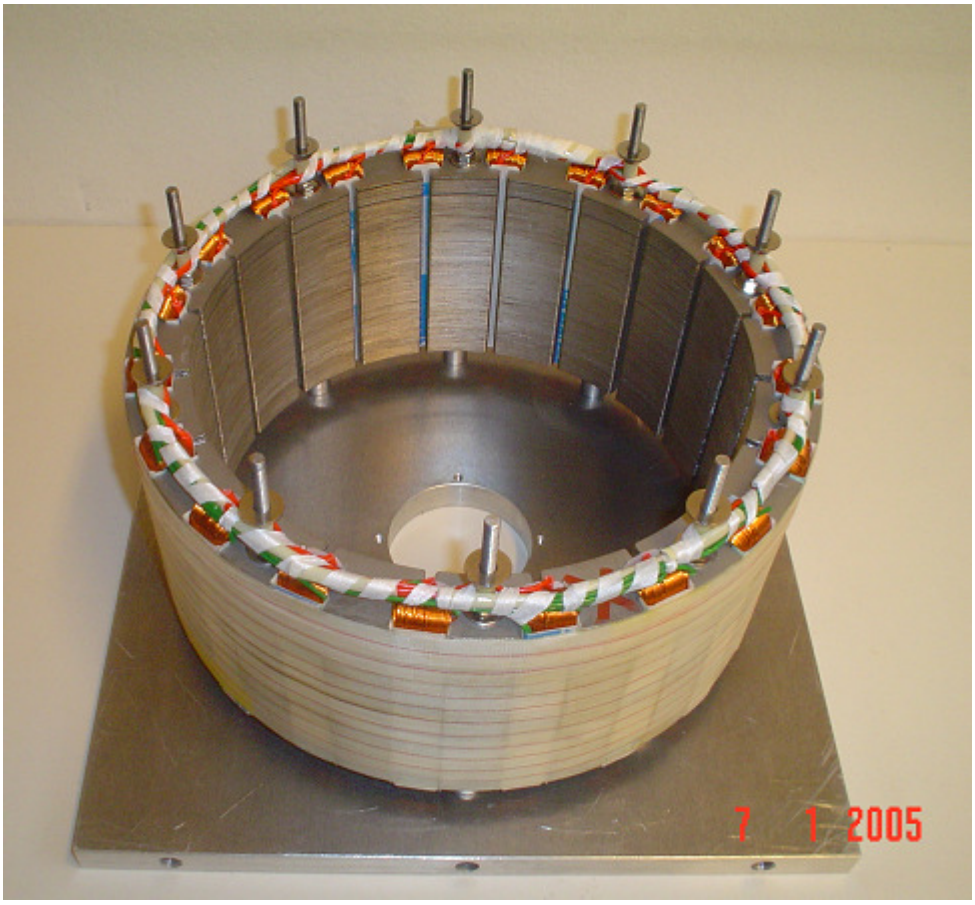

Figure 5.3: Stator with windings fixed on one Aluminum end shield

5.2 Rotor

The main parts of the rotor are permanent magnets, rotor iron pieces, rotor support structure and shaft. The permanent magnets and the iron pieces are glued on the surface of the rotor support structure. To increase the compactness of the rotor, screws are used to fix the iron pieces over the rotor support structure. The iron pieces are attached to both poles of the permanent magnets to produce an easy path for the flux penetration and therefore to reduce the leakage flux.

5.2.1 Permanent magnets

Figure 5.4 shows the output characteristics (B/H characteristics) of the NdFeB permanent magnets provided by the German company 'Vacuumschmelze'. The magnets were fully processed, corrosion coated, precisely cut and already magnetized. Their technical data are given in Table 5.1.

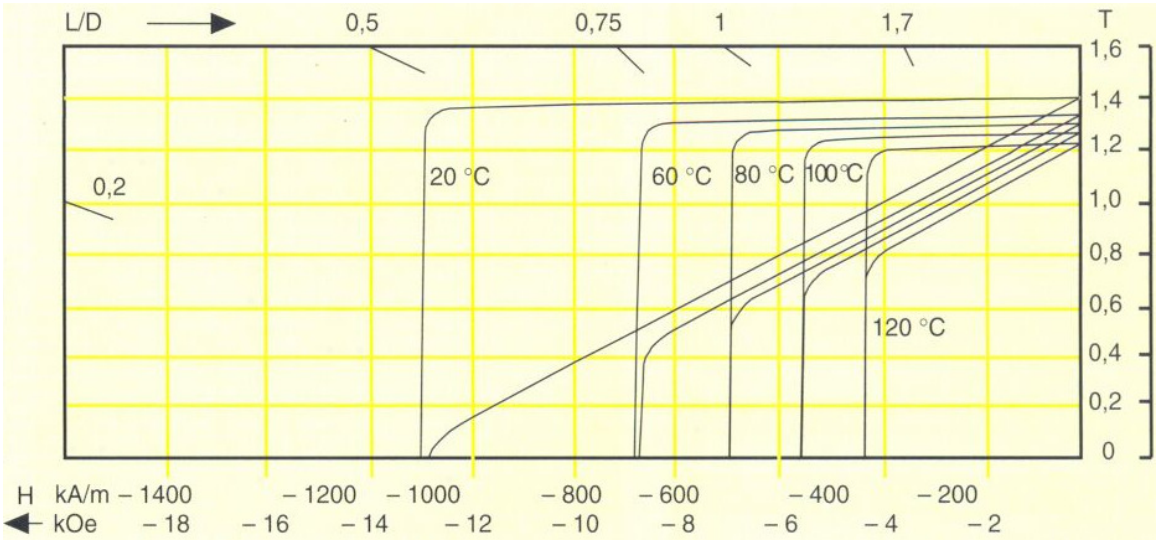

Figure 5.4: B/H characteristics of the used NdFeB Permanent Magnets (IBS)

Table 5.1: Technical data of the used NdFeB Permanent Magnets

Technical Data	**20** ^{o}C	**60** ^{o}C
Remanent Flux Density, B_r	1.41 T	1.35 T
Maximum Energy Product, $(BH)_{\max}$	385 kJ/m^3	Unknown
Apparent Coercivity, H_{ca}	1030 kA/m	640 kA/m
Actual Coercivity, H_c	1020 kA/m	635 kA/m

5.2.2 Rotor support structure

The rotor support structure was manufactured from light nonmagnetic material (Aluminum). Holes are excavated longitudinally to reduce the total weight of the machine and to reduce the moment of inertia and therefore to improve the dynamics of the machine, for example the starting time decreases. A picture for the rotor support structure is given in Figure 5.5.

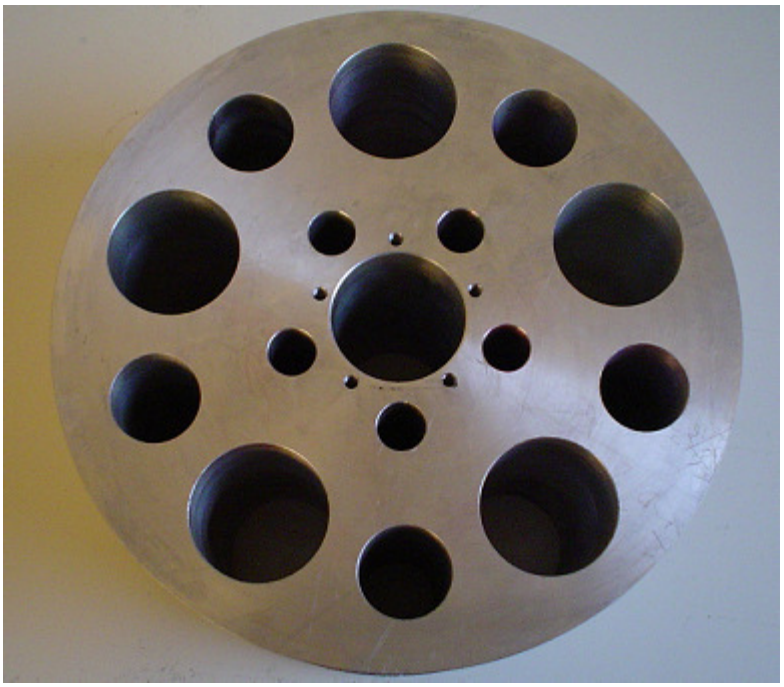

Figure 5.5: Rotor support structure

5.2.3 Shaft

A special shaft was neatly fabricated with an accuracy of ±0.01mm. The detailed dimensions of the shaft are shown in Figure 5.6 and its picture is given in Figure 5.7.

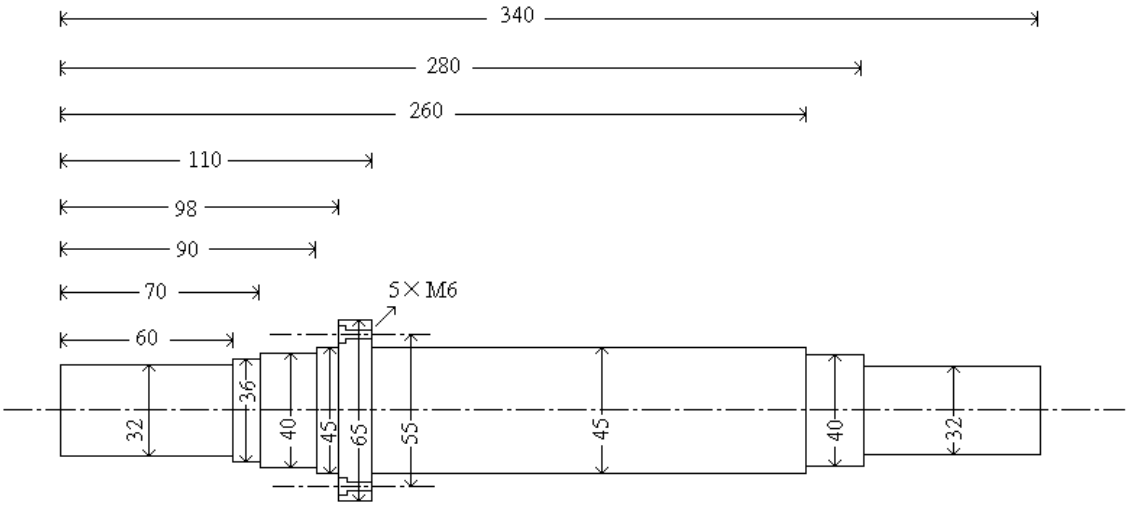

Figure 5.6: Detailed dimensions of the shaft

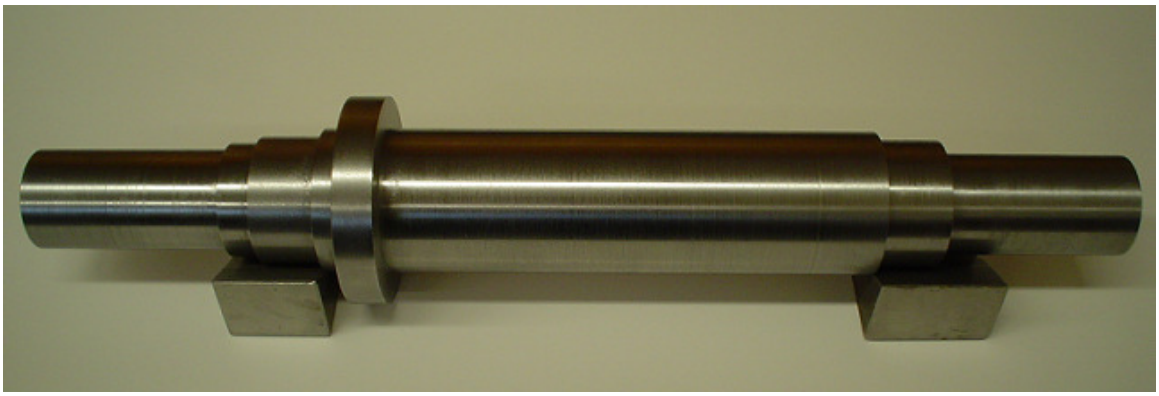

Figure 5.7: Shaft of the prototype machine

5.2.4 Glue

The permanent magnets and iron pieces were glued on the surface of the rotor support structure. The glue is a 1:1 mixture of two types. Their commercial names are EPOXY-Kleber Type 8601 Basis and EPOXY-Kleber Type Haerter. The technical data of the mixture are:

Operating Temperature : up to $300^{o}C$.

Density :1.31g/cm^{3} at $20^{o}C$.

Color :Gray

Viscosity :13500mPa.s at $20^{o}C$.

Working Time :about 2 hours at $20^{o}C$.

Tensile Strength :14.70N/mm^{2} .

Shearing Strength :19.60N/mm^{2} .

Hardening Age :24 hours at $20^{o}C$.

Saving Time :about 2 years.

The gluing area must be free of fat and oil. Figure 5.8 shows the complete construction of the rotor together with the permanent magnets, rotor iron pieces and the shaft.

5.2.5 Rotor iron

The commercial name of the rotor iron is St 60-1. The tensile strength is the range of 590 up to 710N/mm^{2} .

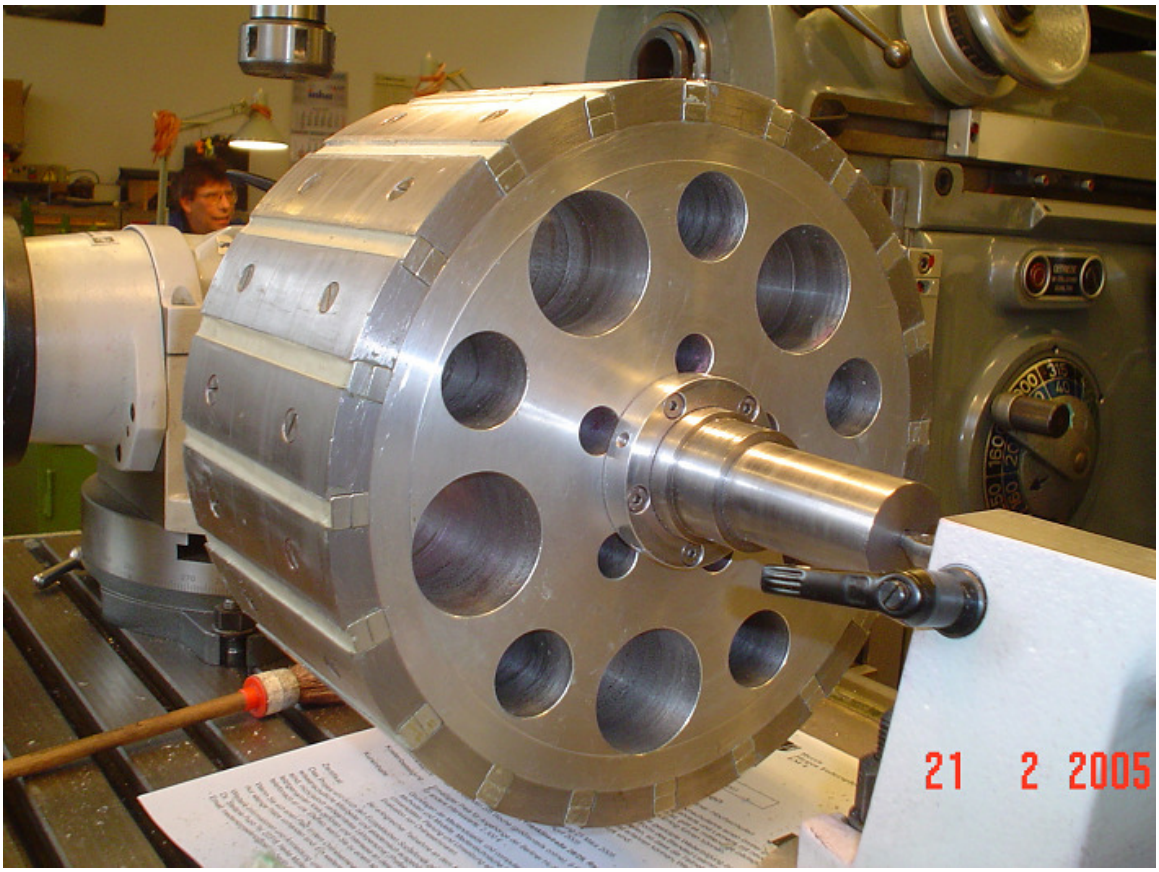

Figure 5.8: Rotor of the prototype machine

5.3 Total construction

Figure 5.9 shows longitudinal section of the complete machine with the detailed dimensions. The active length of the machine is 130mm and the active diameter is 320mm. 20mm is left axially between the two end shields and the machine. 25mm is left radially between the lowest part of the stator and the Aluminum base plate.

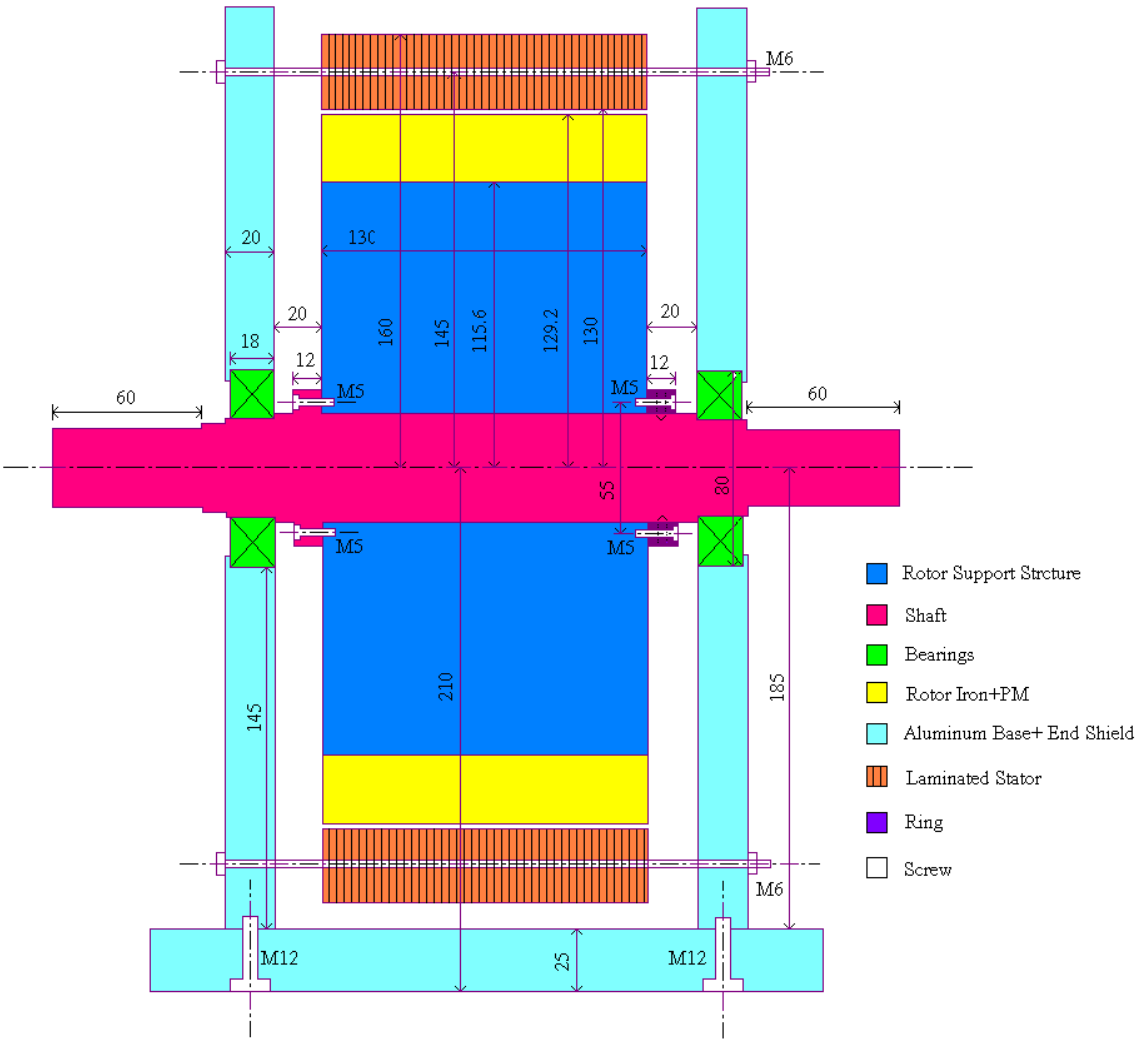

Figure 5.9: Longitudinal section of the prototype machine (windings are not shown)

The front and side views of the bearing holder with their detailed dimensions are presented in Figure 5.10 and Figure 5.11 shows the prototype machine picture.

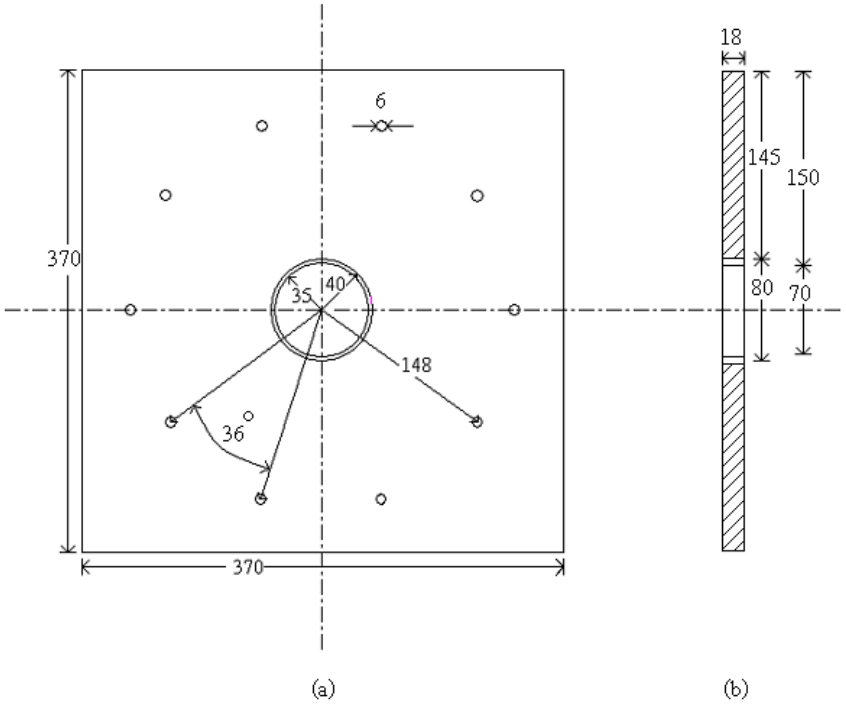

Figure 5.10: End shield (parallel plates), (a) front view and (b) side view

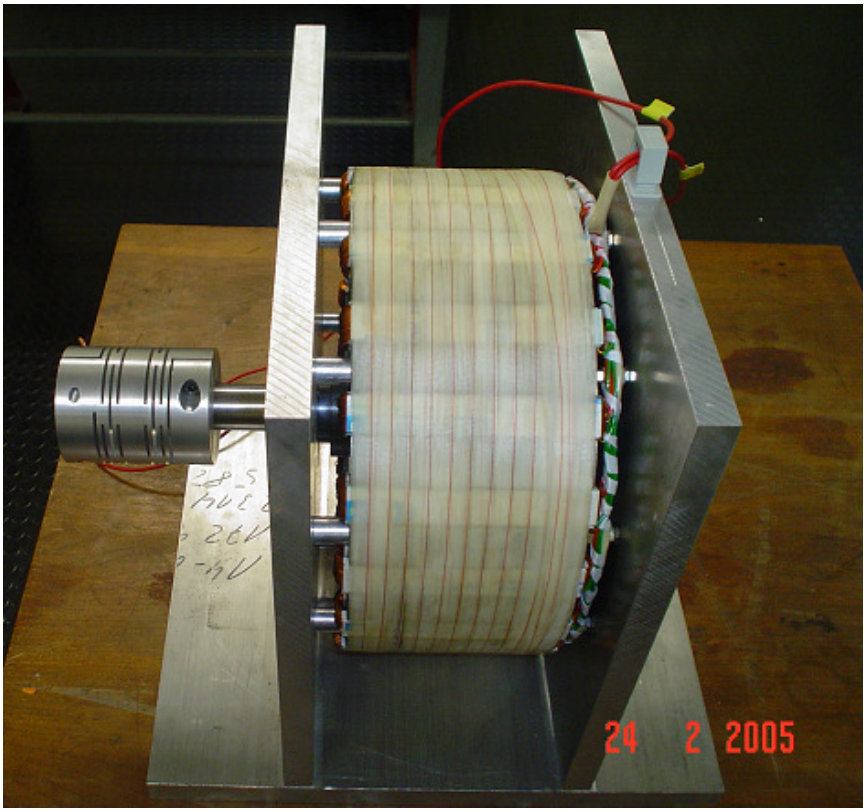

Figure 5.11: The prototype machine with the coupling unit

Chapter 6

Experimental Investigations

The developed machine was tested as a variable low-speed generator. Experimental investigations of the prototype machine together with some comparison between the theoretical and practical results are presented in this chapter. The prime mover is 19.5kW, 400V, 54A, 3020rpm separately excited DC motor with 180V and 2.7A for the excitation. The experimental set up of the prototype machine is shown in Appendix B.

6.1 No-load (open-circuit) characteristics

The open-circuit test is conducted at various speeds. Table 6.1 shows the measured and computed induced voltage, input power and torque at no load. The no-load voltage as function of speed is shown in Figure 6.1. The higher the rotational speed is, the larger the generated voltage tends to be, indicating a linear relationship. The constant of linearity is about 1.39V/rpm. Additionally, the good agreement between the theoretical and practical results is clear. The difference is less than 3%.

Table 6.1: No-load experimental data of the prototype machine

$n(rpm)$	59.4	81.3	100.4	120.5	140.2	160.0	180.9	200.5	220.5	250.5	**measured**
$V_{nl}(V)$	81.2	114	139.9	168.2	195.1	223.4	252.0	279.8	308.0	349.3	**measured**
$V_{nl}(V)$	84.9	116.3	143.6	172.3	200.7	229.0	259.0	287.0	315.6	358.6	**calculated**
$P_{in}(W)$	13.8	21.8	29.0	37.4	46.4	56.4	65.4	78.7	88.3	105.3	**measured**
$T_{in}(Nm)$	2.4	2.7	2.8	3.0	3.1	3.3	3.5	3.7	3.9	4.1	**measured**

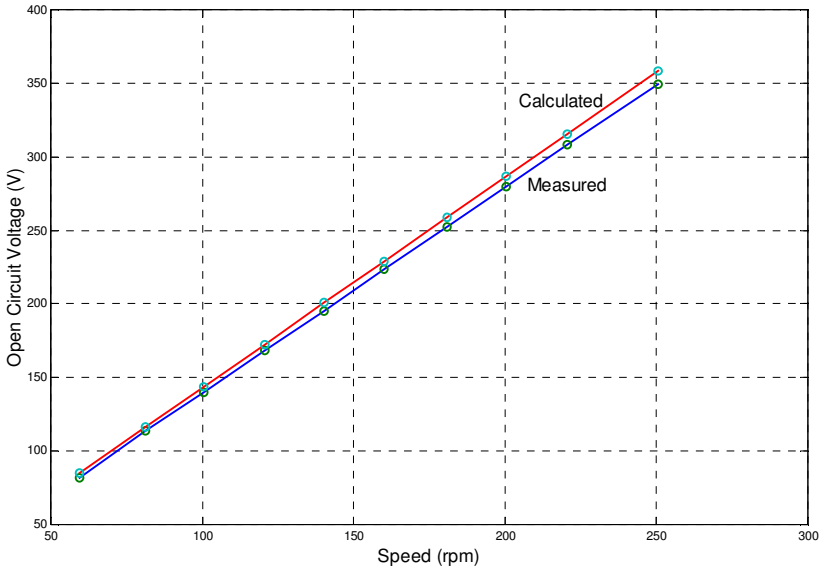

Figure 6.1: Open circuit (no-load) induced voltage as function of speed

Figure 6.2 shows the waveform of the induced voltage at a speed of 180rpm with counter clockwise (CCW) rotor rotation. The air-gap flux density predicted by finite element is shown in Figure 4.6. Apparently, the voltage of the machine is trapezoidal (nonsinusoidal) and the agreement between the calculated and measured waveforms is good.

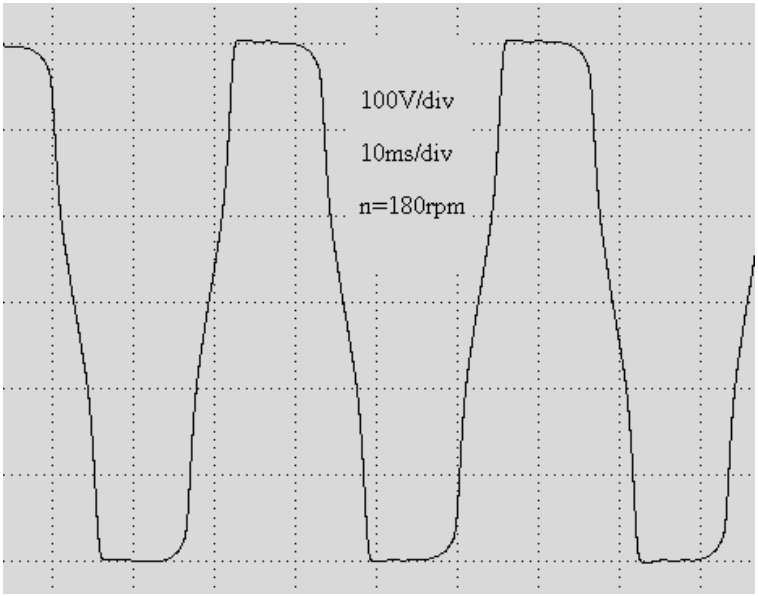

Figure 6.2: No-load voltage waveform with CCW rotor rotation at 180rpm

The no-load input power and the corresponding driving torque are measured at various rotational speeds. The results are shown in Figure 6.3, (a) and (b). This power represents the iron losses (eddy current and hysteresis losses) in the stator yoke & teeth and windage & friction losses (mechanical losses). As the rotational speed (frequency) increases, iron losses increase. The variation is nonlinear as the eddy current losses vary as function of the frequency squared. However, hysteresis losses vary linearly with the frequency.

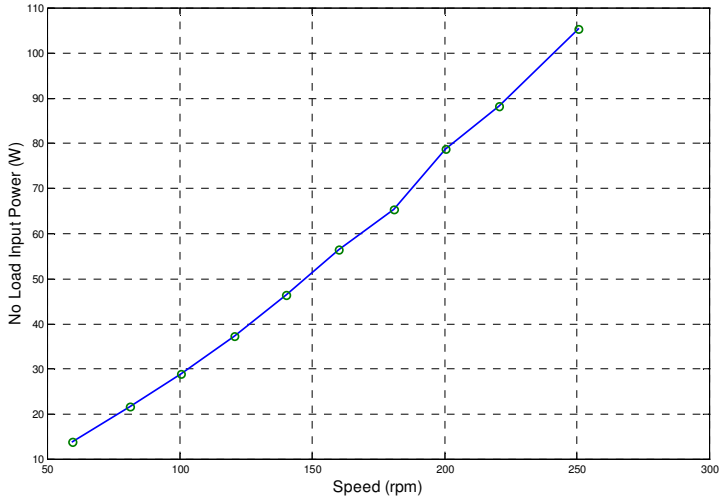

(a)

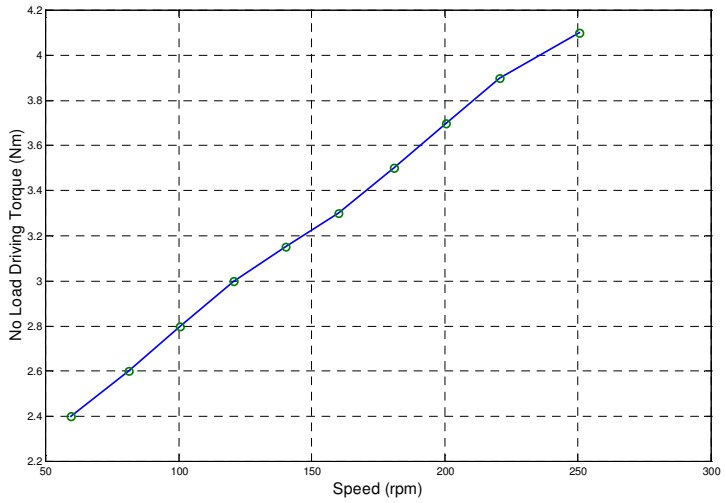

(b)

Figure 6.3: (a) No-load input power as function of speed and (b) the corresponding driving torque

6.2 Load characteristics

The prototype generator is tested with pure resistive load at different speeds. The tests include the output (terminal) characteristics and efficiency. The efficiency of the prototype is compared with other electrical machine types of close output power levels.

6.2.1 Output (terminal) characteristics

The output characteristic of a generator is the relation between the terminal voltage and the stator current when the load connected to the terminals of the generator varies. However, it is advantageous to focus on the terminal (load) voltage and stator current as function of speed with constant load. The terminal voltage, input power, driving torque, output power and efficiency at different rotational speeds and constant pure resistive load of $110\,\Omega$ are shown in Table 6.2. Figures 6.4 and 6.5 show the terminal voltage and stator current of the generator as function of speed when the pure resistive load of $110\,\Omega$ is kept constant. As the speed increases, the internal generated voltage increases. The terminal (load) voltage and stator current increase as a consequence, provided that the load resistance does not change.

Table 6.2: Load data of the prototype machine with a constant pure resistive load of $110\,\Omega$

$n(rpm)$	160.9	181.1	199.6	221.2	239.8	254.1	**measured**
$V_t(V)$	210.5	236.9	262.7	289.4	313.7	331.1	**measured**
$I(A)$	1.91	2.15	2.38	2.62	2.84	2.99	**measured**
$P_{in}(W)$	490	613	750	910	1066	1183	**measured**
$T_{in}(Nm)$	29.0	32.5	35.9	39.3	42.5	44.4	**measured**
$P_{out}(W)$	402	509.3	625.2	758.2	891	990	**calculated**
$\eta\%$	82	83.1	83.4	83.3	83.6	83.7	**calculated**

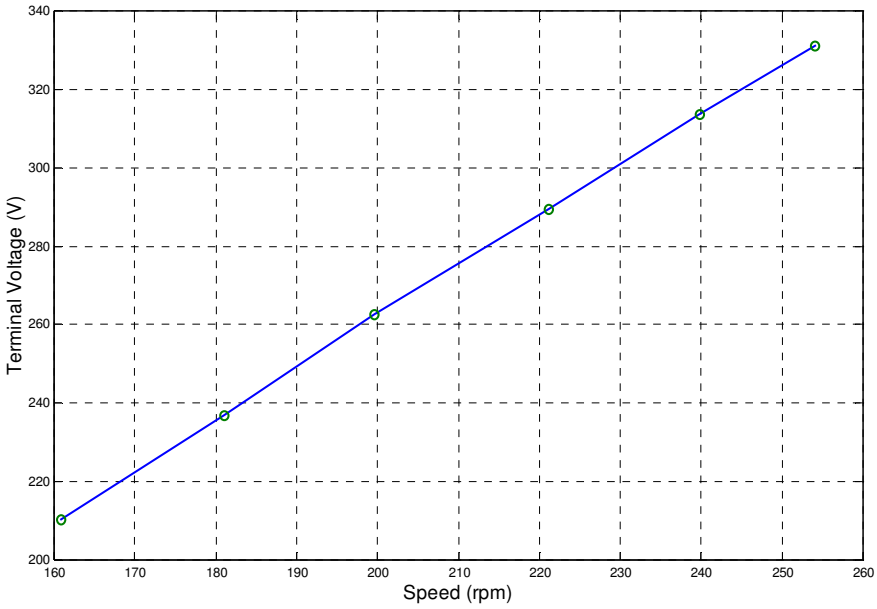

Figure 6.4: Terminal voltage as function of speed with a constant pure resistive load of 110 Ω

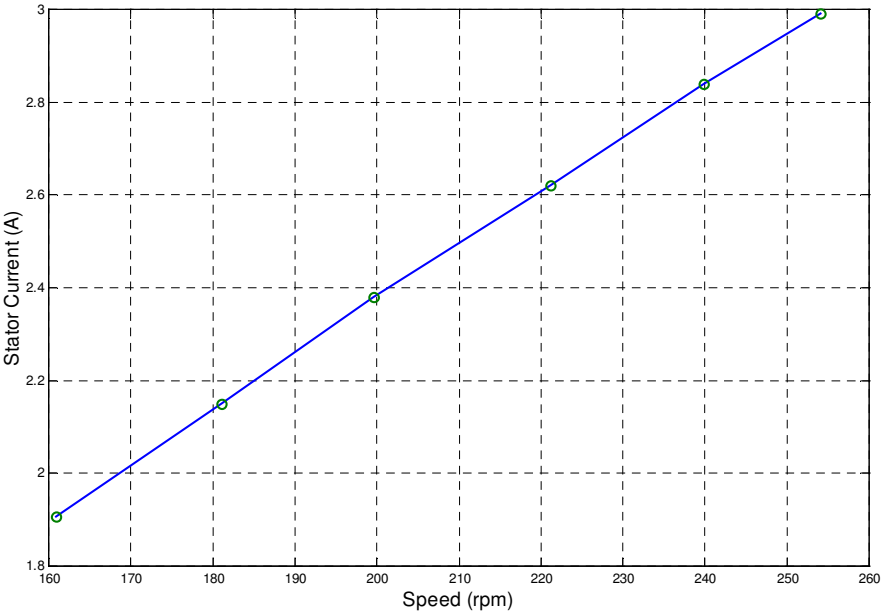

Figure 6.5: Stator current as function of speed with a constant pure resistive load of 110 Ω

The voltage drop across the stator winding resistance and inductance increases when the load current increases. For the same operating speed, the terminal voltage of the generator decreases as a result. Table 6.3 shows the terminal voltage at different stator currents at operating speeds of 120rpm, 180rpm and 250rpm. Figure 6.6 shows the variation of the terminal voltage as function of the stator current with pure variable resistive load at the three different speeds. It is well known that at low speeds (frequencies), the inductance has less effect on the voltage drop than at higher speeds. Therefore, the voltage variation at high speeds should be more visible. The difference between no-load (induced) and full-load (terminal) voltages at 120rpm is 28.2V, at 180rpm is 30V and at 250rpm is 32.3V. On the other hand, voltage regulation $VR\%$ of the generator is defined as:

$$VR\% = \frac{V_{nl} - V_{fl}}{V_{fl}} \times 100\% \qquad (6.1)$$

where V_{nl} : no-load induced voltage.

V_{fl} : full-load terminal voltage.

From Table 6.3, the voltage regulation at 120rpm is 20.2%, at 180rpm is 13.5% and at 250rpm is 10.2%.

Table 6.3: Stator current and terminal voltage at speeds of 120rpm, 180rpm and 250rpm

n=120rpm								
$I(A)$	0.00	0.74	0.98	1.45	2.00	2.69	3.20	3.90
$V_t(V)$	168.0	164.0	162.2	160.0	155.1	148.7	145.9	139.8
n=180rpm								
$I(A)$	0.00	1.00	1.50	2.15	2.60	3.10	3.60	4.00
$V_t(V)$	252.0	244.1	241.0	237.0	233.6	230.0	225.5	222.0
n=250rpm								
$I(A)$	0.00	1.02	1.40	2.03	2.41	2.97	3.40	4.00
$V_t(V)$	349.3	342.2	339.8	335.8	332.5	327.2	323.0	317.0

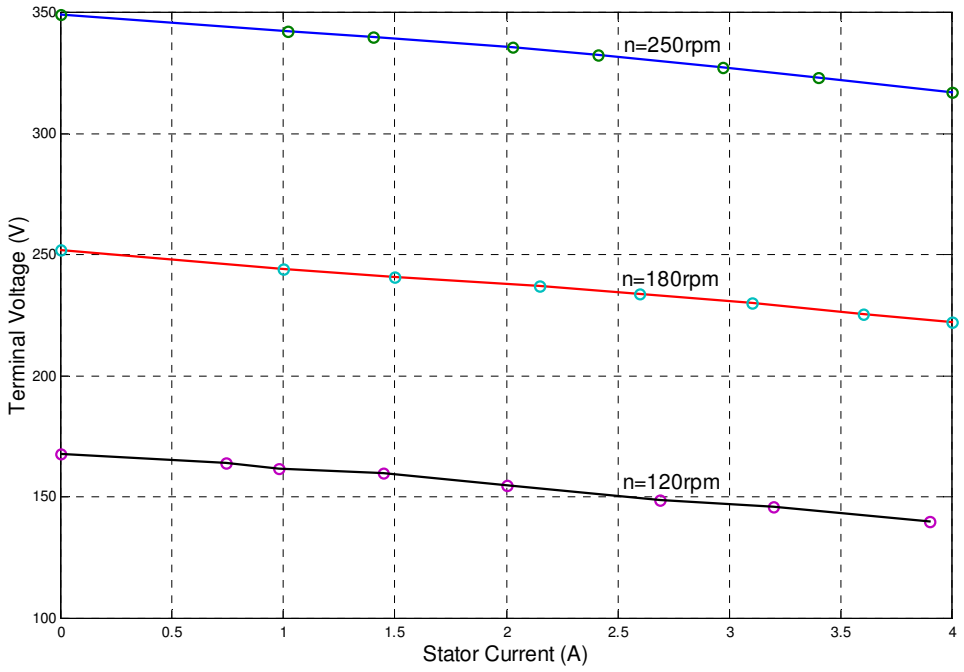

Figure 6.6: Terminal voltage as function of stator current in case of pure resistive load at 120rpm, 180rpm and 250rpm

6.2.2 Efficiency

The efficiency η of the machine is defined as the ratio between the output power of the machine and the input power as in the following equation:

$$\eta = \frac{P_{out}}{P_{in}} = \frac{P_{out}}{P_{out} + P_{loss}} \qquad (6.2)$$

where P_{out} : output power of the machine.

P_{in} : input power to the machine.

P_{loss} : total power loss in the machine.

The total power loss in the machine includes the iron losses of the stator yoke and teeth, copper losses due to the winding resistance, friction and windage losses and some additional stray losses resulted mainly from end leakage flux, iron losses in the rotor iron due to the flux harmonics as well as eddy current losses of the magnets. Figure 6.7 illustrates the power flow of an electric motor.

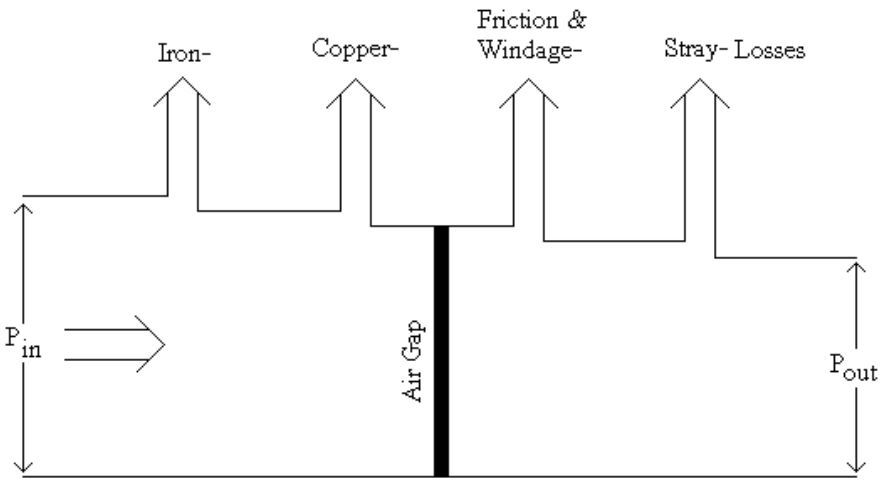

Figure 6.7: Schematic of power flow in an electrical motor

The input and output power of the machine as function of speed with a constant pure resistive load of about $110\,\Omega$ is shown in Figure 6.8. The difference between them represents the power losses of the machine, which increase as function of speed. As the speed (frequency) increases, the iron and copper losses increase.

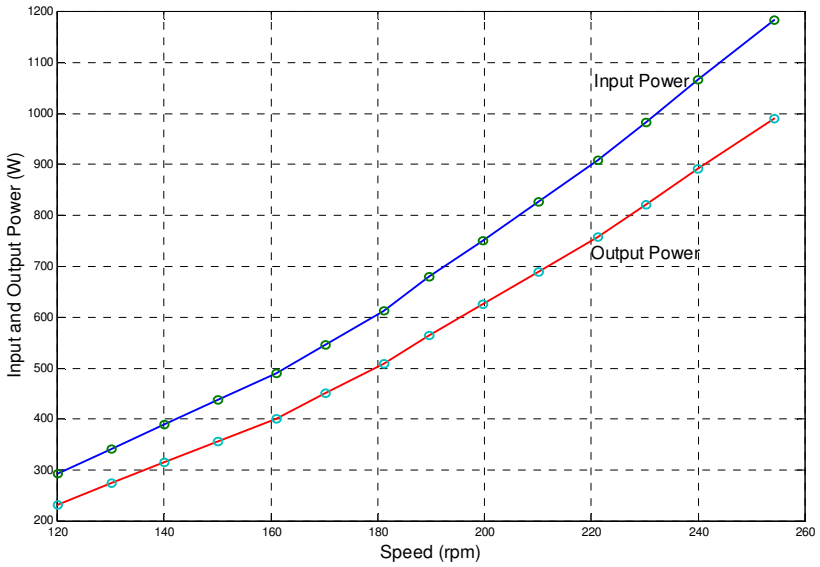

Figure 6.8: Input and output power as function of speed with a constant pure resistive load of $110\,\Omega$

The variation of the efficiency of the machine as function of speed with a constant pure resistive load of 110Ω is shown in Figure 6.9. The efficiency of the machine at a speed of 120rpm (232W) is about 79%, at a speed of 180rpm (509W) is about 83.1% and about 83.6% at a speed of 250rpm (990W).

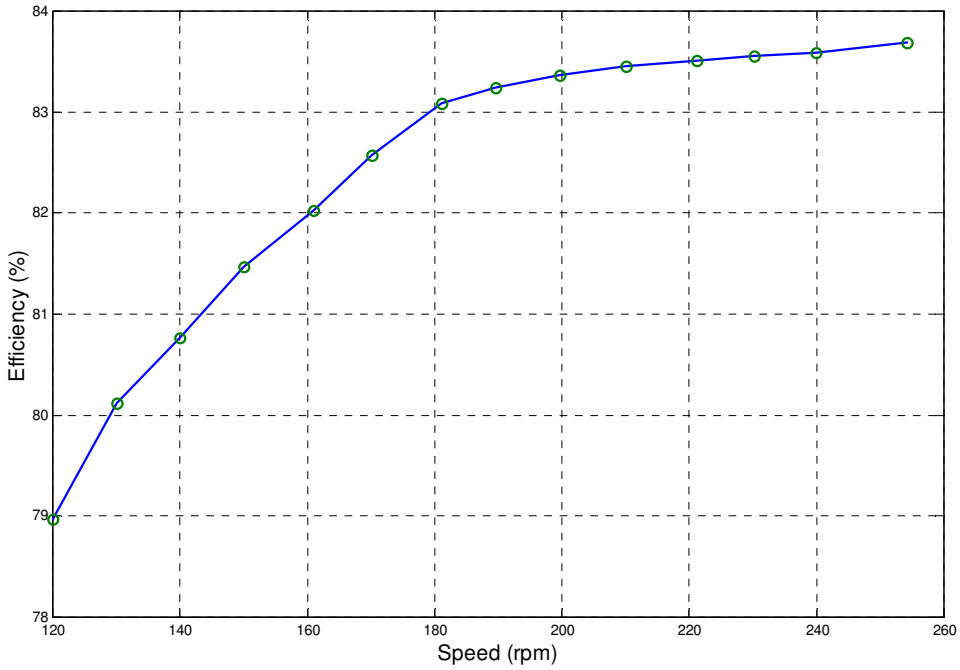

Figure 6.9: Efficiency as function of speed with a constant pure resistive load of 110Ω

Table 6.4 shows the efficiency of the machine and the stator current with a pure resistive load at speeds of 120rpm, 180rpm and 250rpm. The efficiency of the machine as function of stator current for the three different speeds and pure resistive load is shown in Figure 6.10. The maximum efficiency of the machine at 120rpm is about 80.2% and is related to an output power of about 310.2W and the maximum efficiency at 180rpm is about 83.2% and occurs at an output power of about 607.4W. The efficiency of the machine at a speed of 250rpm and output power of 1268W is about 84.6%. Figure 6.11 shows the efficiency of different types of electrical machines with close output power levels [45], [2] and [46]. It can be concluded that the developed prototype machine exhibits relatively better efficiency compared with other types of machines. This relative high efficiency came as a

result of the low copper losses resulting from the short endwindings and the presence of the permanent magnets in flux concentration arrangement for the field.

Table 6.4: Efficiency and stator current at speeds of 120rpm, 180rpm and 250rpm

n=120rpm							
$I(A)$	0.74	0.98	1.45	2.00	2.69	3.20	3.90
$\eta\%$	74.3	78.4	79.7	80.2	79.6	79.0	77.0
n=180rpm							
$I(A)$	1.00	1.50	2.15	2.60	3.10	3.60	4.00
$\eta\%$	75	80.1	83.1	83.2	82.9	82.3	81.7
n=250rpm							
$I(A)$	1.02	1.40	2.03	2.41	2.97	3.40	4.00
$\eta\%$	74.1	78.8	82.5	83.0	83.6	84.0	84.6

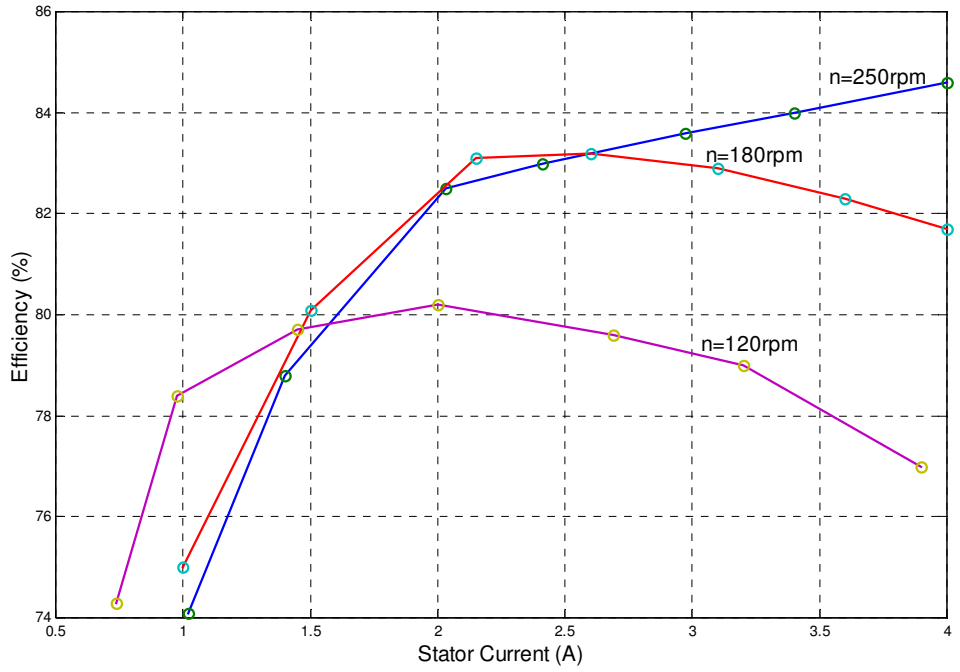

Figure 6.10: Efficiency as function of stator current with pure resistive load at 120rpm, 180rpm and 250rpm

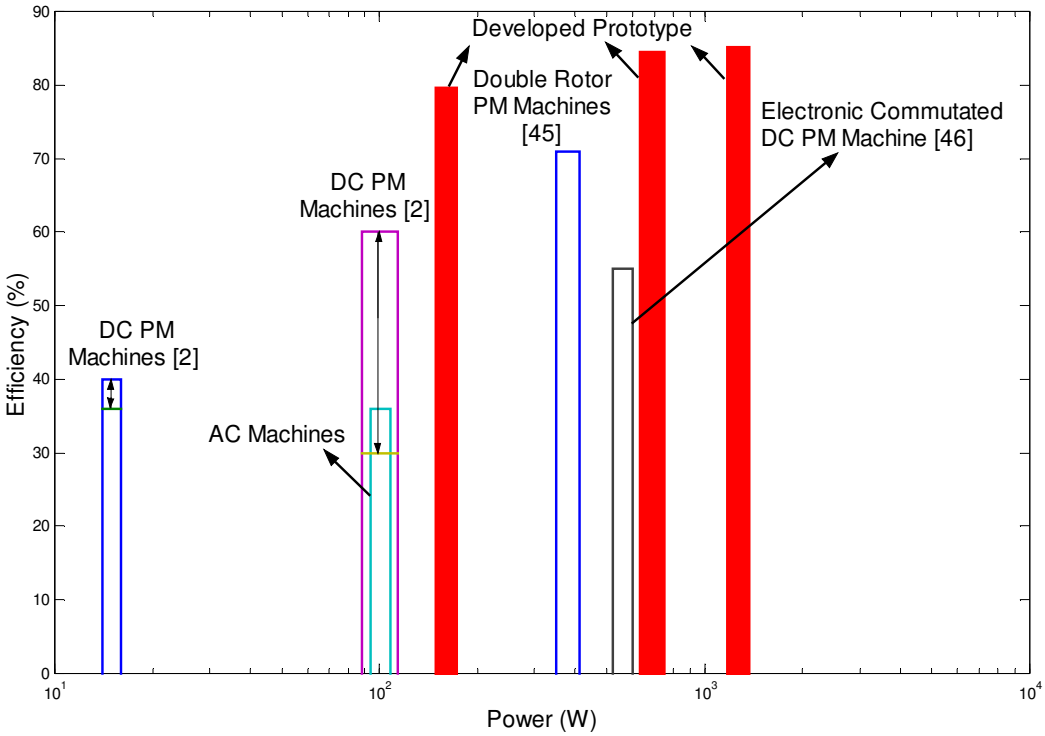

Figure 6.11: Efficiency of different types of machines at close output power levels

6.3 Torque ripple

The electromagnetic instantaneous torque of an electrical machine has two components, constant or average component and periodic component. The periodic component is function of time or rotor position and superimposed on the constant component. The periodic component causes *torque pulsation* also called torque ripple. This *torque ripple* is caused by both the construction of the machine and power supply. There are three sources of torque ripple coming from the construction of the magnetic and electric circuits of a machine:

1) Cogging effect, which is the interaction between the rotor magnetic flux and variable reluctance of the air gap due to the geometry of the stator slots.
2) Distortion of the sinusoidal or trapezoidal distribution of the magnetic flux density in the air gap.
3) Differences between reluctances of the air gap in the d- and q-axes.

The cogging effect produces the so-called *cogging torque*, higher harmonics of the magnetic flux density in the air gap produce the *field harmonic electromagnetic torque*, and the unequal reluctances in the d- and q-axes produce the *reluctance torque*. The torque ripple caused by the power supply is due to the current ripple resulting from the pulse width modulation (PWM) and/or phase current commutation.

The torque ripple of the machine was measured using a torque transducer of 600Hz, 100Nm and 10Nm/V. Figure 6.12 shows the torque response of the machine with a load of 2.79A (82.8Ω) at 180rpm. The zoomed torque ripple is shown in Figure 6.13. The maximum value of the steady state torque ripple is about 0.2Nm. The nominal torque of the machine is 53Nm.

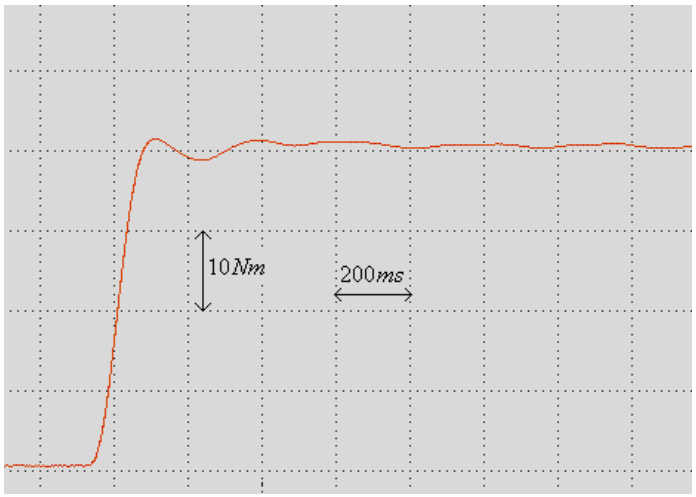

Figure 6.12: Torque response with a load of 2.79A (82.8Ω)

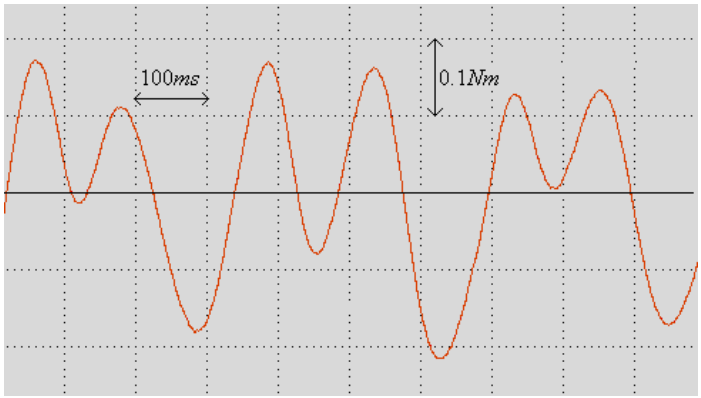

Figure 6.13: Torque ripple with a load of 2.79A (82.8Ω)

6.4 Parameter measurements

The resistance of the stator winding and d- and q-axes inductances are measured and compared with the computed values.

6.4.1 Resistance

The circuit shown in Figure 6.14 is used for measuring the resistance of the stator winding. DC power supply is used to eliminate the effect of the inductance. Different readings for the voltage and current are taken. The slope of the V-I line represents the ohmic resistance of the stator winding. Table 6.5 shows the obtained values and Figure 6.15 shows the voltage as function of the current. It is seen that the stator windings of this single-phase generator have a total resistance of $6.545\,\Omega$.

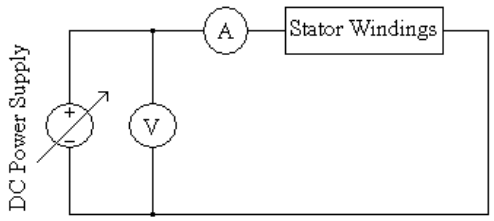

Figure 6.14: Circuit for measuring the resistance of the stator windings

Table 6.5: Data for measuring the stator winding resistance ($T = 25^{o}C$)

$V(V)$	$I(A)$	$R = \frac{V}{I}(\Omega)$
0.735	112.5×10^{-3}	6.533
1.138	174.1×10^{-3}	6.536
1.425	0.217	6.567
1.952	0.298	6.550
2.226	0.340	6.547
2.678	0.409	6.548
3.017	0.461	6.544
3.281	0.502	6.536
3.948	0.603	6.547
4.263	0.652	6.538

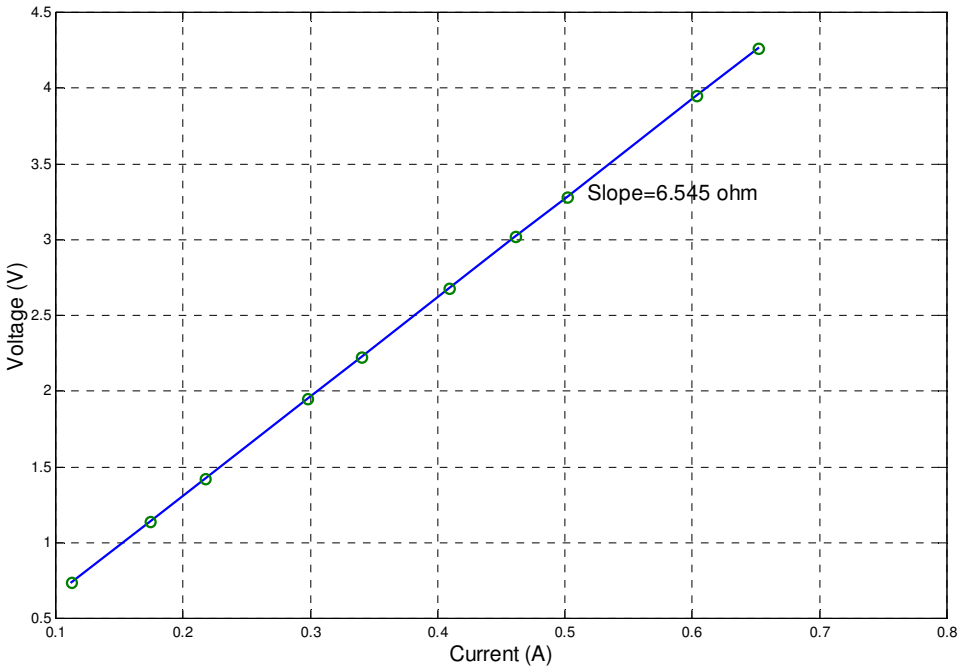

Figure 6.15: Voltage as function of current of the stator windings

The above measurement data have been carried out at a temperature of $20^{o}C$. To take the effect of temperature into account, the following equation should be used:

$$R = R_{20}(1+\alpha_{20}(T-20)) \qquad (6.3)$$

where R: resistance at certain temperature T.

R_{20}: measured resistance at room temperature.

α_{20}: temperature coefficient of copper resistance at $20^{o}C$, equals $4.3\times10^{-3}\ K^{-1}$.

6.4.2 Inductances

Of the steady state parameters of the single-phase synchronous generators are the direct-axis synchronous reactance X_d and the quadrature-axis synchronous reactance X_q. To determine X_d (or X_q), the mmf axis of the stator winding is aligned with the direct-axis (or quadrature axis) of the rotor. X_d (or X_q) is then computed as the ratio of the flux linkages of the winding to its current. The flux linkage ψ in the coil in the d-axis (or q-axis) winding is defined as:

$$\psi = N\phi \tag{6.4}$$

where N : number of turns of the winding.

ϕ : stator yoke flux.

The corresponding total direct-axis inductance L_d or quadrature-axis inductance L_q will be:

$$L_d \text{ (or } L_q) = n_c \frac{N\phi_{d(or,q)}}{I} = n_c \frac{NB_{yoke}h_{yoke}l_{stk}}{I} \tag{6.5}$$

where n_c : number of coils connected in series.

$\phi_{d(or,q)}$: d or q-axis flux linkage.

B_{yoke} : stator yoke flux density.

h_{yoke} : height of the yoke.

l_{stk} : active length of the machine

I : the winding current which produces the flux.

The direct-axis and quadrature-axis inductances are predicted using the finite element method. Figure 6.16 shows the d-axis flux lines distribution for one coil with a stator current of about 4.35A and zero remanent magnet flux density and Figure 6.17 shows the corresponding stator yoke flux density. It can be concluded that the average stator yoke flux density is about 0.136T. Consequently, the total d-axis inductance L_d will be:

$$L_d = 20 * \frac{(60)(0.136 * 8\times10^{-3} * 130\times10^{-3})}{4.35} = 39.02\times10^{-3} = 39.02mH$$

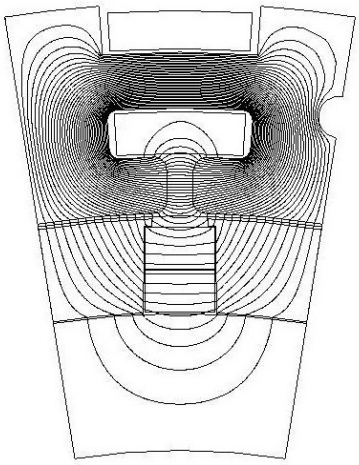

Figure 6.16: D-axis flux lines distribution with only stator MMF acting alone (permanent magnet remanent flux density equals zero)

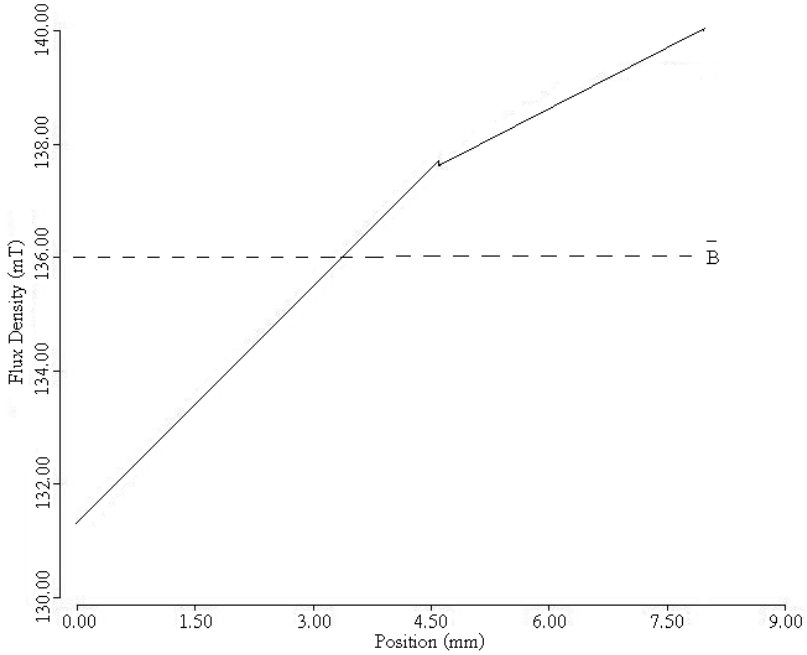

Figure 6.17: D-axis stator yoke flux density with only stator MMF acting alone (permanent magnet remanent flux density equals zero)

As for the q-axis inductance, Figure 6.18 shows the q-axis flux lines distribution for one winding with a stator current of about 4.35A and zero remanent magnet flux density and Figure 6.19 shows the corresponding stator yoke flux density. It can be noticed that the

average stator yoke flux density is about 0.36T. Consequently, the total q-axis inductance L_q will be:

$$L_q = 20 * \frac{(60)(0.36 * 8 \times 10^{-3} * 130 \times 10^{-3})}{4.35} = 103.3 \times 10^{-3} = 103.3mH$$

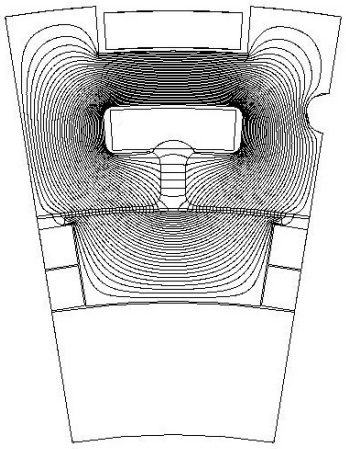

Figure 6.18: Q-axis flux lines distribution with only stator MMF acting alone (permanent magnet remanent flux density equals zero)

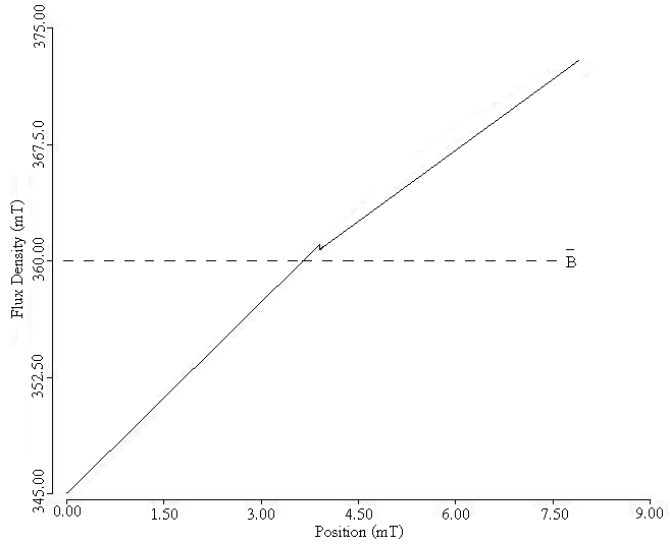

Figure 6.19: Q-axis stator yoke flux density with only stator MMF acting alone (permanent magnet remanent flux density equals zero)

The d- and q-axes inductances are also measured. Figure 6.20 shows the circuit used for this task. Different readings are taken in both cases. The first one is carried out for the d-

axis inductance with the mmf axis of the stator winding aligned with the direct-axis of the rotor. The second one is carried out for the q-axis inductance with the mmf axis of the stator winding aligned with the quadrature-axis of the rotor. The supply frequency is 100Hz. Table 6.6 shows the measured voltage and current for the two rotor positions together with the inductances that have been calculated from the following equation:

$$L_d \ (\text{or}\, L_q) = \frac{\sqrt{Z^2 - R^2}}{2\pi f} \qquad (6.6)$$

where Z: magnitude of the winding impedance, R: stator winding resistance and f: frequency of the supply voltage.

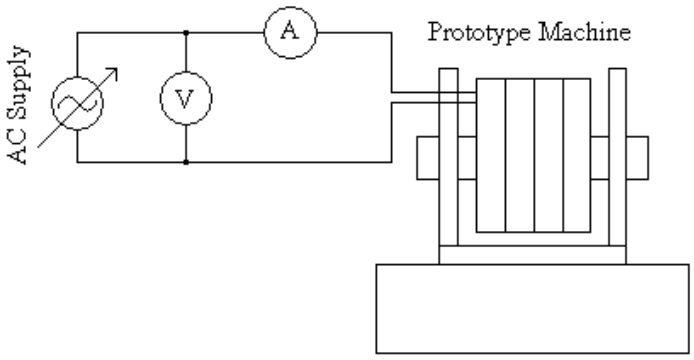

Figure 6.20: Circuit for measuring the d- and q-axes inductances

Table 6.6: Data for d- and q-axes inductance measurements with a supply frequency of 100Hz

d-axis measurements				**q-axis measurements**			
$V(V)$	$I(mA)$	$Z = \frac{V}{I}(\Omega)$	$L_d(mH)$	$V(V)$	$I(mA)$	$Z = \frac{V}{I}(\Omega)$	$L_q(mH)$
0.8640	33.6	25.71	39.6	1.485	23.3	63.73	100.9
1.2782	49.5	25.82	39.8	2.184	33.8	64.62	102.3
1.6282	62.8	25.93	39.9	3.096	47.3	65.45	103.6
2.0690	79.2	26.12	40.2	3.812	57.9	65.84	104.3
2.4380	93.2	26.16	40.3	4.487	67.8	66.18	104.8
$L_{d,av}$			40.0	$L_{q,av}$			103.2

From Table 6.6, the measured values of the d- and q-axes inductances are very close to that of the already computed values using FET.

6.5 Non-electrical characteristics of the prototype machine

The developed prototype is a low speed machine. Low-speed machines are characterized by the small active length compared with their diameter as the number of pole pairs is relatively high. Additionally, low speed machines are heavy and have usually lower efficiency. The following table shows some of the non-electrical characteristics of the developed machine:

Table 6.7: Non-electrical parameters of the prototype machine

Parameter	Value
Weight of the rotor support structure	9.62 kg
Weight of the shaft	3.50 kg
Total weight of the stator laminations	19.62 kg
Total weight of the permanent magnets	5.08 kg
Weight of the copper	3.76 kg
Weight of the rotor iron pieces	7.79 kg
Total weight of the rotor	25.99 kg
Total weight of the stator	23.38 kg
Weight of active material	36.25 kg
Power to weight ratio	27.59 W/kg
Torque to weight ratio	1.46 Nm/kg
Slot fill factor	42.04%
Diameter to active length ratio	2.46
Rotor diameter to shaft diameter ratio	4.04

Chapter 7

Effect of Slot Opening Filling on the Cogging Torque and Performance of the Machine

Cogging torque is an inherent characteristic of slotted permanent-magnet electrical machines caused by the geometry of the machine. The cogging torque effects are maximum when the number of the slots equals the number of poles. Cogging torque affects self-starting ability and produces noise and mechanical vibrations. Minimizing cogging torque is important in applications where reducing torque ripple, vibration and noise is an essential requirement. This chapter presents the effects of filling the slot openings with bonded soft magnetic material (magnetic wedges) on the torque response, cogging torque and performance of the machine.

7.1 Finite element analysis

Figure 7.1 shows the configuration of the machine with the magnetic wedges placed in the slot openings. They are filled with bonded soft magnetic material with relative permeability $\mu_r = 10^*$. The no-load flux lines distribution is shown in Figure 7.2. The leakage flux between the poles has increased and therefore the stator yoke flux density will decrease. As shown in Figure 7.3, the average stator yoke flux density is about 1.49T. The average stator yoke flux density with empty slot openings was 1.55T (Figure 4.4). Thus, the induced voltage will decrease by a factor of about 4%. The full-load flux lines distribution is shown in Figure 7.4. Obviously, the flux distortion increases once the machine is loaded and the leakage flux between the magnet poles and across the filled slot openings increases as well.

* as given by the manufacturer.

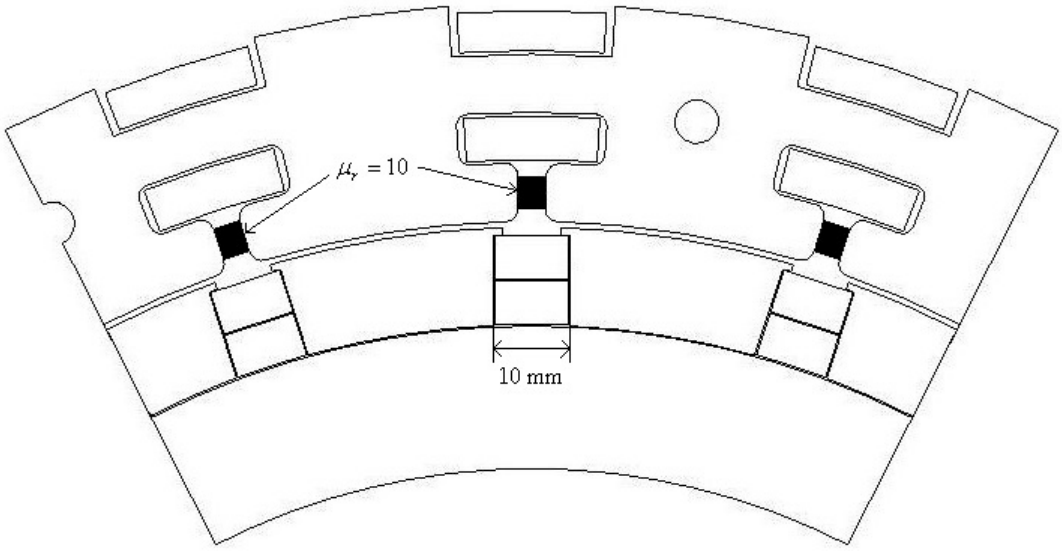

Figure 7.1: The configuration of the machine with magnetic wedges filling the slot openings

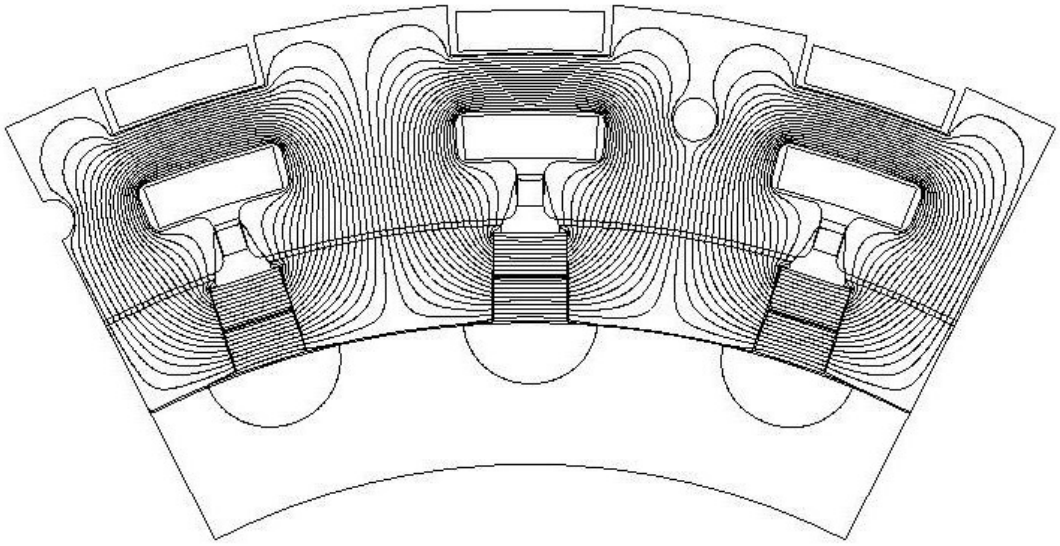

Figure 7.2: No-load flux lines distribution

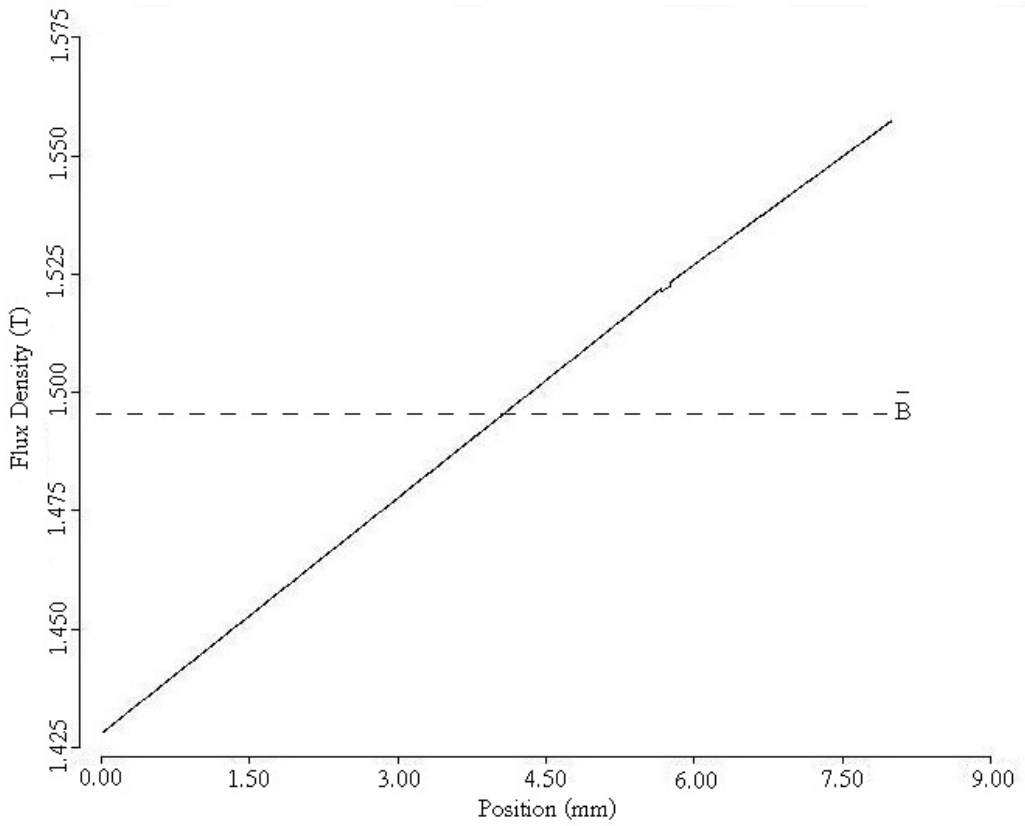

Figure 7.3: No-load stator yoke flux density with filled slot openings

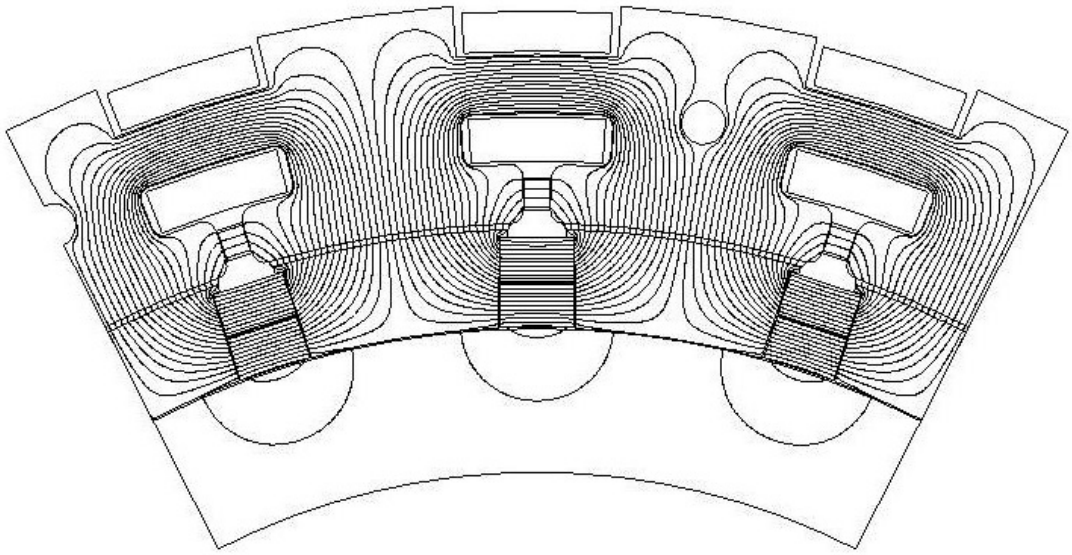

Figure 7.4: Full-load flux lines distribution with filled slot openings

The cogging torque with filled slot openings is estimated. Figure 7.5 shows the flux lines distribution at different rotor positions. The variation of the co-energy of the permanent magnets with the rotor position and the nearest polynomial function representing them are shown in Figure 7.6 (a). The corresponding cogging torque compared with the previous case is shown in Figure 7.6 (b). Interestingly, the maximum value of the cogging torque in this case is reduced. It is about 80% of the case when the slot openings were empty.

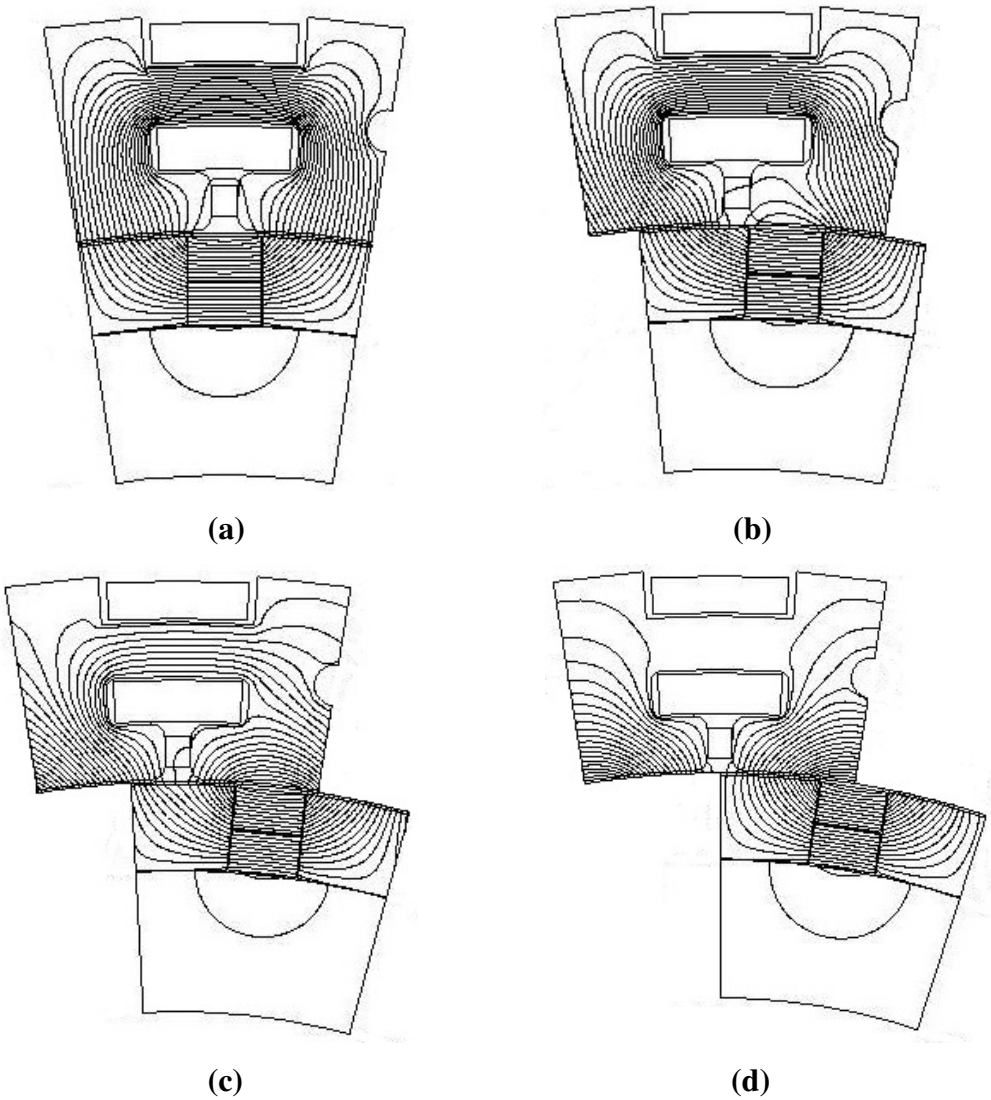

Figure 7.5: Flux lines distribution at no load with, (a) 0, (b) 3, (c) 6 and (d) 9 mechanical degrees rotor angles, the slot openings are filled with bonded soft magnetic material with μ_r=10

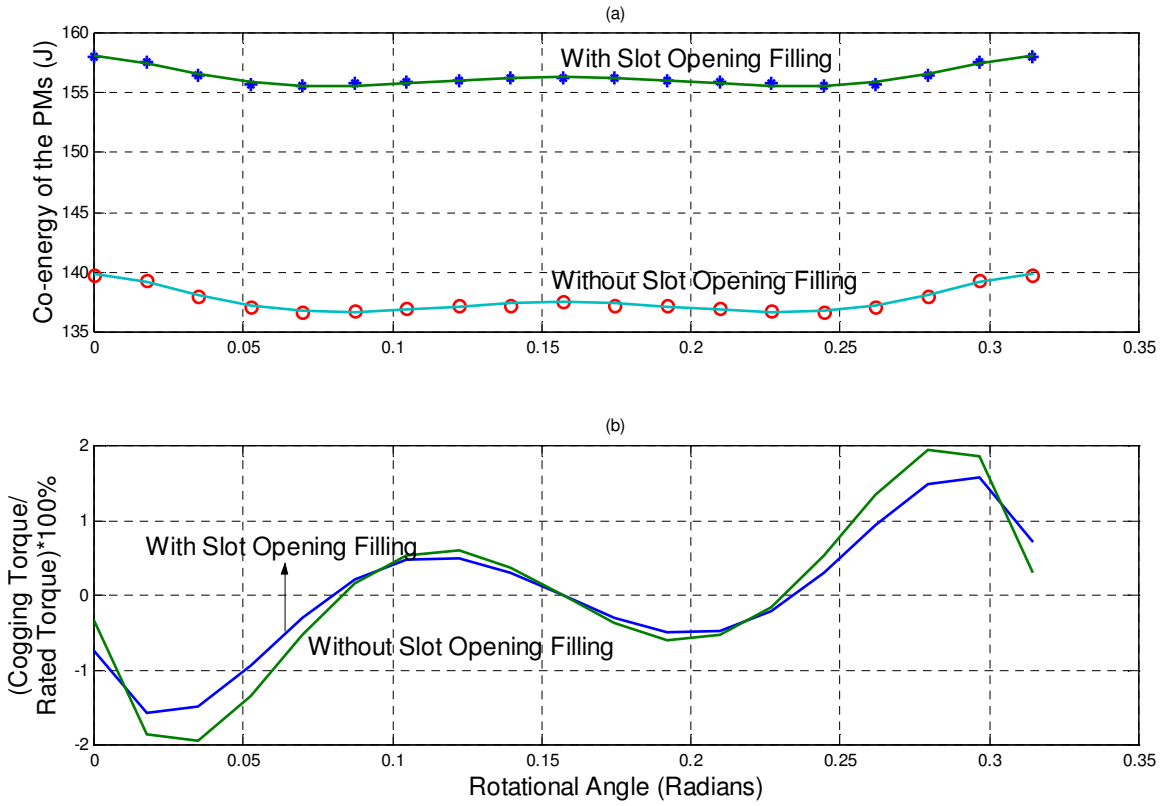

Figure 7.6: (a) Co-energy of the PMs for one pole pitch with and without slot openings filling and (b) the corresponding cogging torque

7.2 Experimental study

The torque response of the machine in both cases of empty and filled slot openings and the performance of the generator are outlined experimentally in this section. The measurements were carried out by a torque transducer of 600Hz, 100Nm and 10Nm/V.

7.2.1 Torque response

The inertia of the rotor together with the cogging torque necessitated a relatively high starting torque. Figure 7.7 shows the torque response with empty slot openings at no load. The maximum value of the torque response is about 34Nm, 64% of the rated torque of the machine. However, once the machine runs steadily, the torque ripple decreases to a very small value compared with the rated torque. The torque response of the machine

with filled slot openings is presented in Figure 7.8. The maximum value of the torque response is about 23Nm, 43% of the rated torque of the machine.

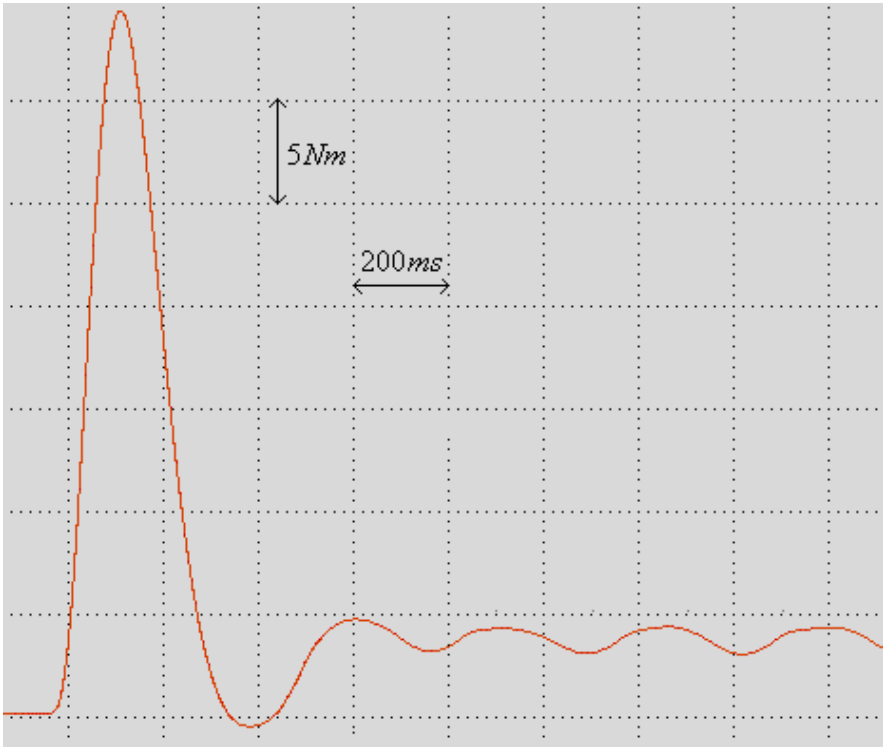

Figure 7.7: Torque response with empty slot openings

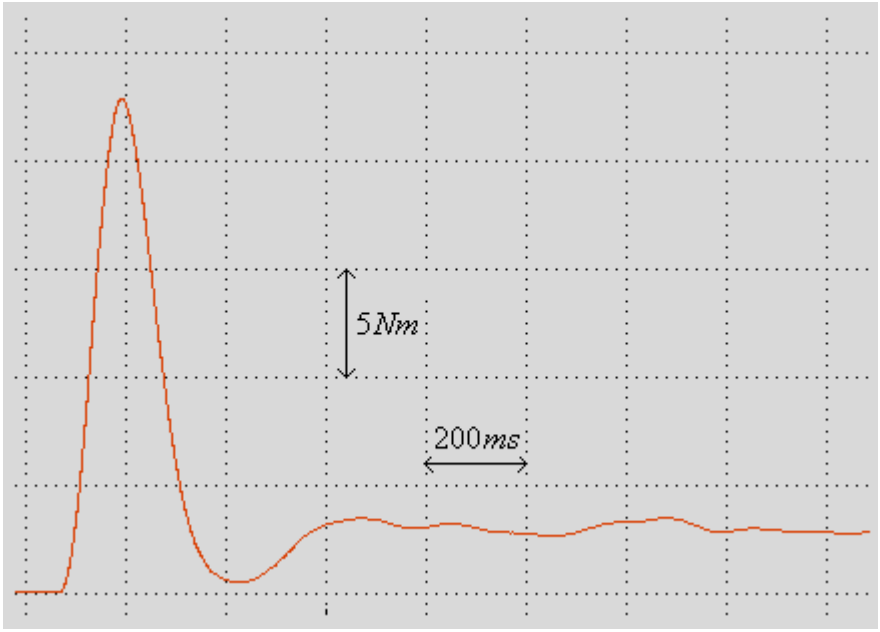

Figure 7.8: Torque response with filled slot openings

7.2.2 Generator performance

It is shown in this chapter that filling the slot openings with bonded soft magnetic material (magnetic wedges) with relative permeability higher than that of the free space can reduce the torque ripple of the machine and improve the torque response. However, the effect of these improvements is some modest changes in machine performance. The terminal characteristics corresponding to the two cases (empty and filled slot openings) are shown in Figure 7.9 at a rotational speed of 180rpm when a pure variable resistive load is connected at the terminals of the generator. It is clear that the magnetic wedges have an influence on the performance of the generator. The terminal voltage at a stator current of 4A is reduced by a factor of about 5.4% and the voltage regulation increased from 12% to 14.3%. The reason is that the magnetic wedges reduce the induced voltage and increase the d- and q-axes inductances.

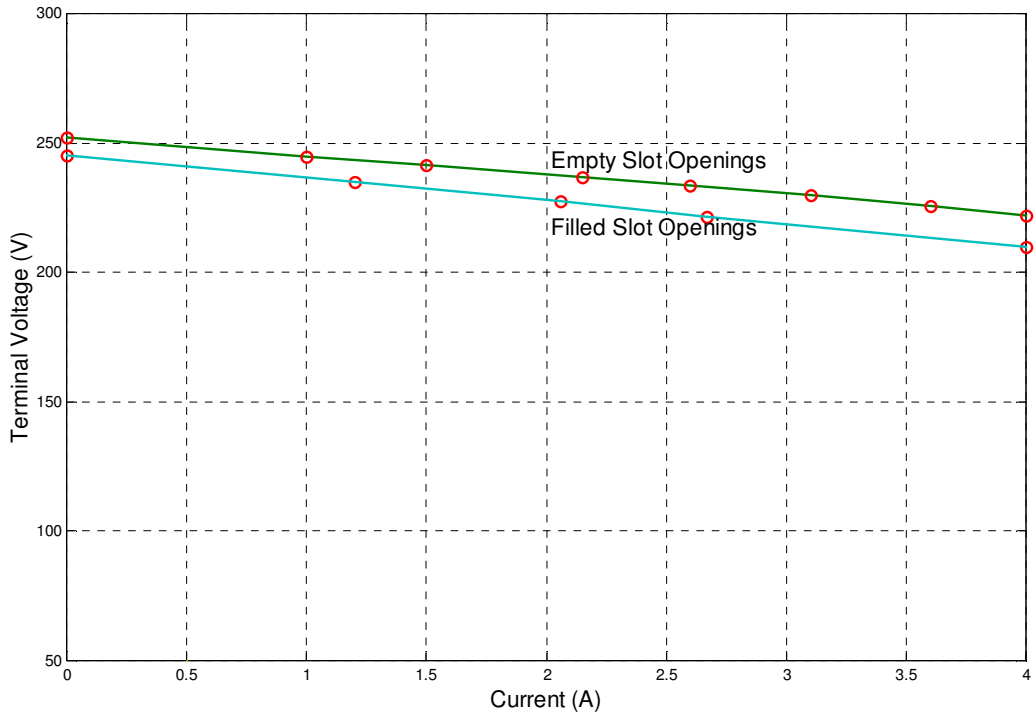

Figure 7.9: Terminal characteristics at 180rpm for empty and filled slot openings

Chapter 8

Finite Element Design of Three-Phase Machines

Due to the unique set of advantages of permanent magnet electrical machines like unsurpassed efficiency, increased reliability, high power density and reduction in the total usage space & weight, the applications of these types of machines are continuously increasing. Battery charging, remote areas and islands electricity supplying, relay stations activating and automotive generators are some of their applications. This chapter deals with the finite element design and theoretical study of two three-phase machines of the same topology as the previously designed, built and tested single-phase machine. The first machine is four-pole three-slot type while the second is of ten-pole and six-slot design.

8.1 Four-pole three-slot machine

This section presents the finite element design of the four-pole three-slot three-phase permanent-magnet electrical machine. The magnets are NdFeB with a remanent flux density B_r of about 1.41T, coercivity H_c of about –700kA/m and maximum energy product $(BH)_{\max}$ of about 370kJ/m^3 at room temperature. Their flux concentration is tangential on the rotor support structure, the slots are flat, one slot per phase and Y-connected stator.

The complete machine has been modeled. Figure 8.1 shows the topology of the machine. The direction of magnetization and the arrangement of active materials are presented. The no-load flux lines distribution is shown in Figure 8.2. Apparently, the leakage flux between the magnet poles is negligibly small. The main dimensions of the machine are given in Table 8.1.

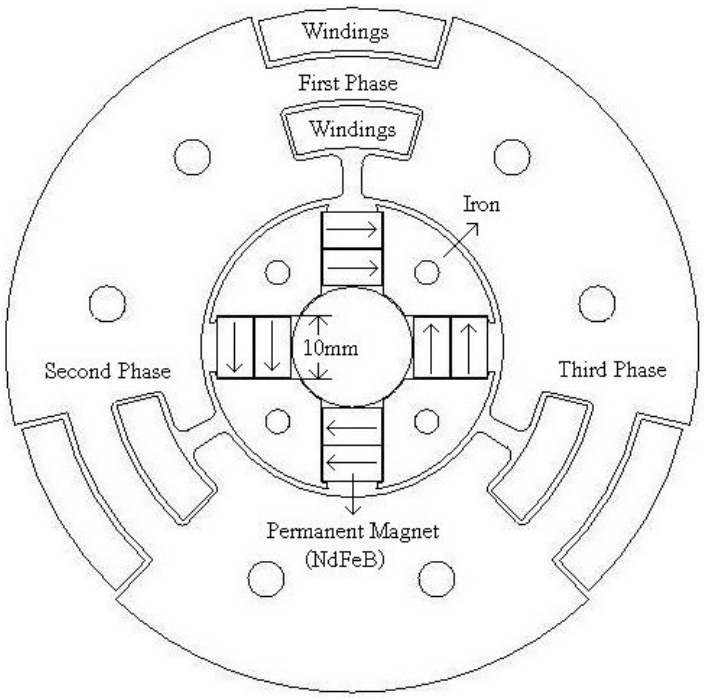

Figure 8.1: Arrangement of active material of the three-phase four-pole three-slot machine

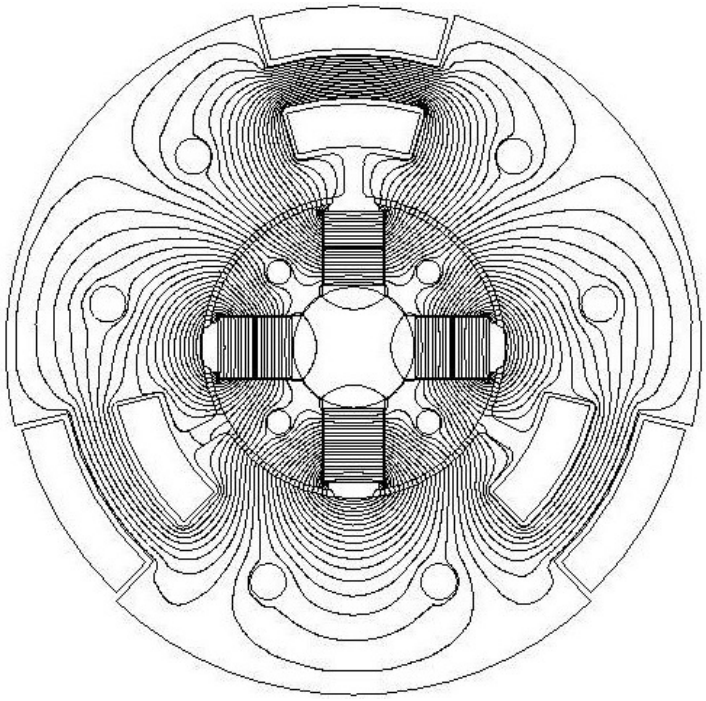

Figure 8.2: No-load flux lines distribution

Table 8.1: Main dimensions of the three-phase three-slot four-pole machine

Inner radius of the stator, r_s **(mm)**	25.0
Width of the slot, W_{slot} **(mm)**	21.8
Height of the slot, h_{slot} **(mm)**	9.0
Height of the yoke, h_{yoke} **(mm)**	7.2
Length of PM in direction of magnetization, l_M **(mm)**	10.0
Height of PM, h_M **(mm)**	6 (two are used)
Air gap length, g **(mm)**	1.0
Total radius of the machine, r_o **(mm)**	57.4
Active length of the machine, l_{stk} **(mm)**	400

The air gap flux density distribution is shown in Figure 8.3. The maximum value is about 0.65T. The higher the value of the air gap flux density is, the smaller the size and cost of the machine tends to be for the same output. However, the value of operating flux density in the teeth and yoke increases with increased value of air gap flux density. Normally, flux densities of the teeth and yoke should not exceed 1.8T. It is found from the finite element design that the average stator yoke flux density B_{yoke} is about 1.55T. The number of turns N is 40 turns per phase with four parallel coils per winding. With a machine active length l_{stk} of 400mm, the rms value of the fundamental component of the induced no-load phase voltage E_{rms} at 1200rpm (frequency f = 40Hz) will be:

$$E_{rms} = 4.44Nf\phi_m = 4.44NfB_{yoke}h_{yoke}l_{stk} = 4.44*40*40*1.55*7.2\times10^{-3}*400\times10^{-3} = 31.7V.$$

where ϕ_m is the maximum value of the stator yoke flux.

The rms value of the induced no-load line voltage $E_{rms,L}$ will be:

$$E_{rms,L} = \sqrt{3}E_{rms} = 54.9V.$$

With a current density of 6A/mm^2 and a conductor diameter of 0.8mm, the output power of the machine will be about 1000W at 1200rpm and pure resistive load (assuming that the full load terminal voltage is 90% of the no-load induced voltage).

At a speed of 1200rpm and full load the terminal voltage will be about 48V, which makes it suitable for battery charging. In case of renewable energy applications a gearbox has to be implemented.

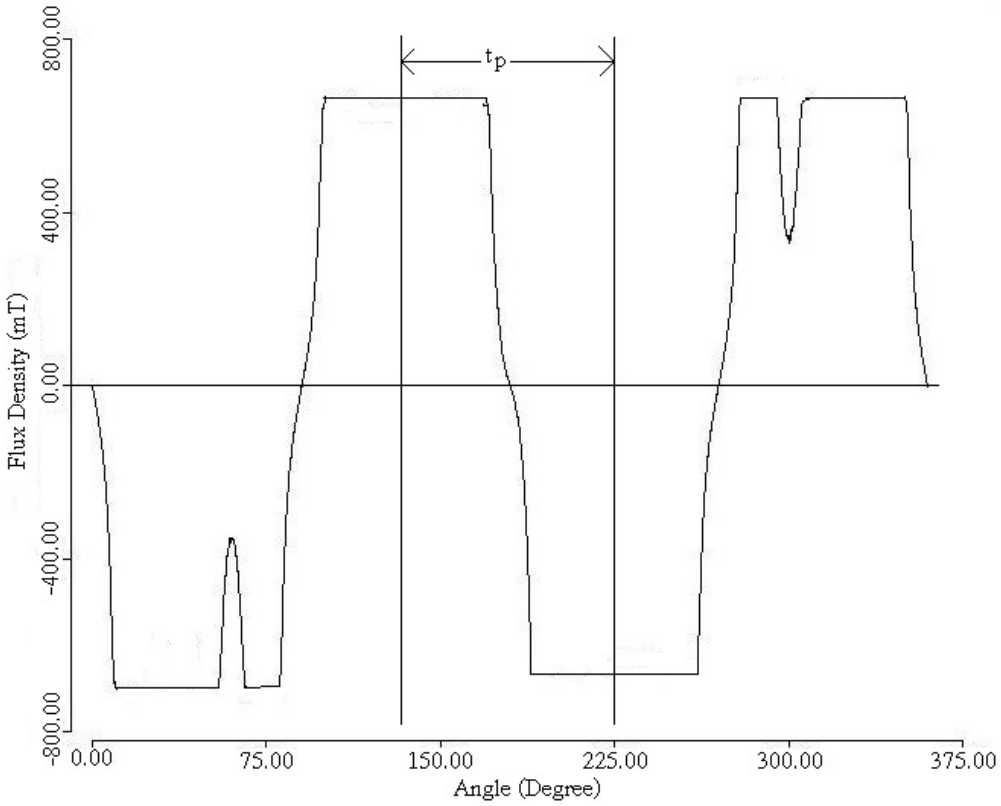

Figure 8.3: No-load air gap flux density distribution

8.2 Ten-pole six-slot machine

This section presents the finite element analysis of the ten-pole six-slot three-phase permanent-magnet electrical machine. The design has to be within 180mm diameter. The magnets are NdFeB with a remanent flux density B_r of about 1.41T, coercivity H_c of about -700kA/m and maximum energy product $(BH)_{\max}$ of about 370kJ/m^3 at room temperature. Their flux concentration is tangential on the rotor support structure, the slots

are flat, two slots per phase and Y-connected stator. Table 8.2 presents the main dimensions of the machine. The construction and the arrangement of active material are shown in Figure 8.4. The no-load flux lines distribution is shown in Figure 8.5 and the air gap flux density is shown in Figure 8.6.

Table 8.2: Main dimensions of the three-phase six-slot ten-pole machine

Inner radius of the stator, r_s **(mm)**	59.0
Width of the slot, W_{slot} **(mm)**	27.1
Height of the slot, h_{slot} **(mm)**	8.0
Height of the yoke, h_{yoke} **(mm)**	7.5
Length of PM in direction of magnetization, l_M **(mm)**	10.0
Height of PM, h_M **(mm)**	6 (two are used)
Air gap length, g **(mm)**	1.0
Total radius of the machine, r_o **(mm)**	90.0
Active length of the machine, l_{stk} **(mm)**	70

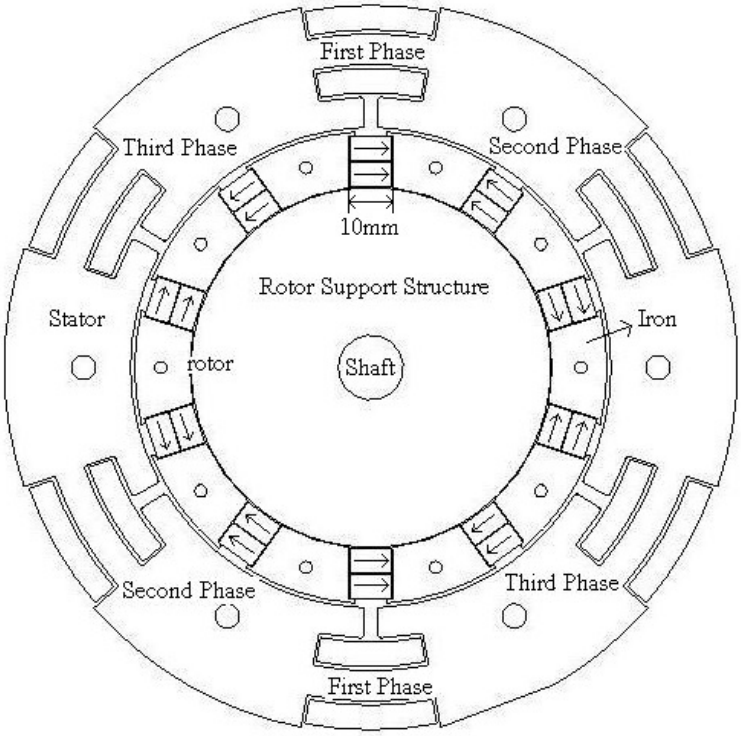

Figure 8.4: Arrangement of active material of the three-phase ten-pole six-slot machine

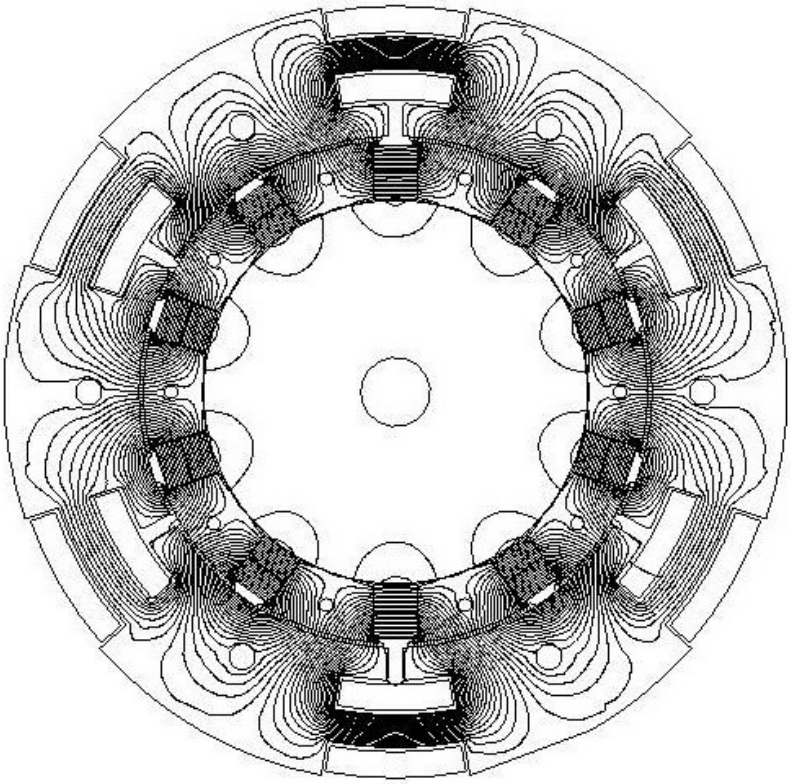

Figure 8.5: No-load flux lines distribution

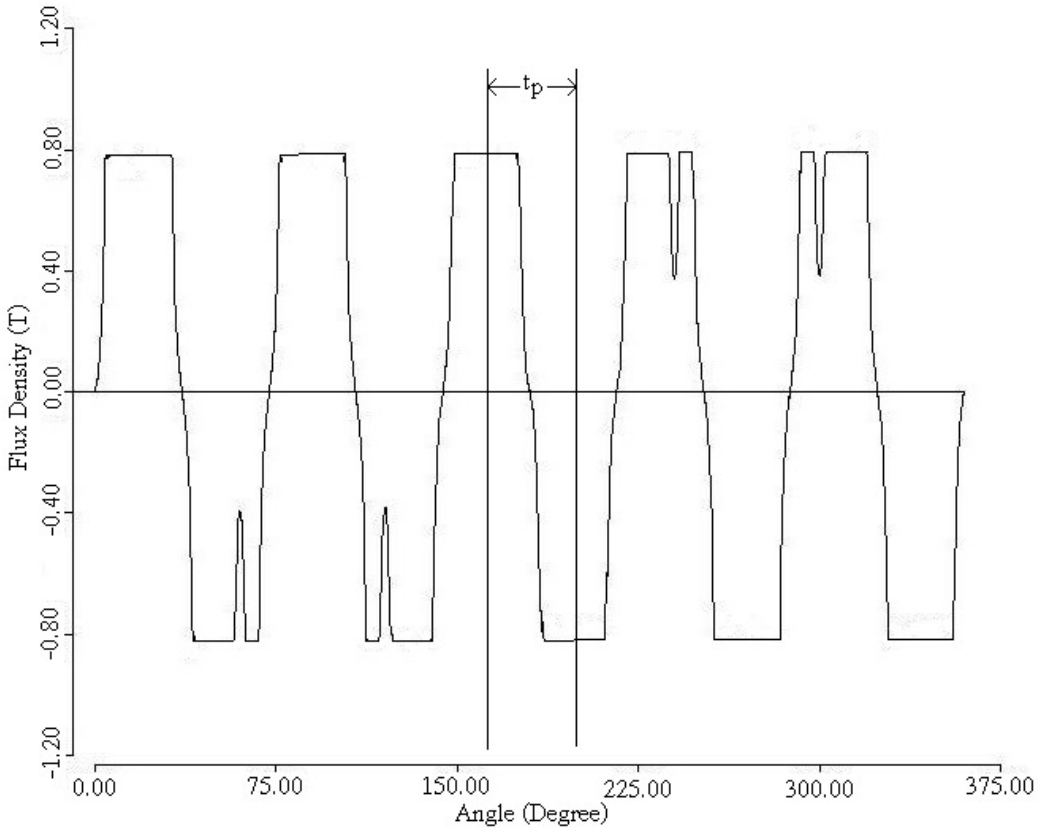

Figure 8.6 No-load air gap flux density distribution

It is found that the average stator yoke flux density B_{yoke} is about 1.55T. The number of turns N is 180 turns per phase with two parallel coils per winding. With a machine active length l_{stk} of 70mm, the rms value of the fundamental component of the induced no-load phase voltage E_{rms} at 200rpm (frequency f =16.7Hz) will be:

$$E_{rms} = 4.44Nf\phi_m = 4.44NfB_{yoke}h_{yoke}l_{stk} = 4.44*180*16.7*1.55*7.5\times10^{-3}*70\times10^{-3}$$
$$= 10.9V.$$

where ϕ_m is the maximum stator yoke flux.

The rms value of the induced no-load line voltage $E_{rms,L}$ will be:

$$E_{rms,L} = \sqrt{3}E_{rms} = \sqrt{3}\times10.9V = 18.9V.$$

With a current density of 6A/mm^2, a conductor diameter of 0.8mm and a unity power factor load, the output power at 200rpm will be about 177W (assuming that the full load terminal voltage is 90% of the no-load voltage).

According to the company 'Ropatec', a generator of a nominal speed in the range of 100rpm up to 250rpm can be directly coupled with a wind turbine [47]. The rated speed of the six-slot ten-pole machine is 200rpm. Khan and Pillay (2005) have presented the radius of the turbine blades as function of the rated power for a wind speed range of 6m/s up to 12m/s. They have also outlined the speed of the generator as function of the rated power for the same speed range. It is also found that there is a good agreement between the several design parameters of the developed prototype and the design data of their machine [48].

Chapter 9

Conclusions and Future Work

A low-speed radial-flux rare-earth permanent-magnet machine with a new topology was designed, optimized, built and tested. The machine can be used as directly driven wind-energy generator. The design was carried out using high-energy NdFeB permanent magnets with flux concentration. Design principles and important equations were fully developed and used. An iterative preliminary design was firstly carried out and optimized based on the equivalent magnetic circuit approach and the load line characteristics of the permanent magnet. The finite element analysis was then used for detailed investigations and final adjustments. The topology allows for toroidal design (torus) with short endwindings. This contributes to higher efficiency, lower active material cost and higher power to weight ratio. The high flux concentration of the permanent magnets is tangential on the rotor support structure, which must consist of nonmagnetic material. To produce an easy path (low reluctance) for the flux penetration, soft magnetic material pieces were attached to both poles of the permanent magnets. The rotor support structure was manufactured from a light material (Aluminum) where better dynamical performance can be achieved i.e. the starting time will decrease. To further reduce the cost of active material, the effective air-gap length is reduced by slotting the stator laminations where the toroidal windings were placed. The slots are flat and the laminations were cut using laser technology methods. The cogging torque of the machine was estimated using the flux-MMF method. The configuration of the rotor corresponding to the lowest cogging torque was selected.

The prototype machine was manufactured and tested as a variable low-speed generator. Good agreement between theoretically predicted and experimentally obtained results has been achieved. The prototype machine exhibits relatively high efficiency, low active material cost and a typical ‘rule of thumb’ value for the leakage flux coefficient. Table 9.1 presents the efficiency of the developed prototype along with that of different electrical machine types with close output power levels.

Table 9.1: Efficiency of different electrical machine types including that of the developed prototype

Machine Type	Power (W)	Efficiency (%)
DC Permanent Magnet Motor [2]	100	55-82
Induction Motor [2]	100	57
Electronic Commutated DC permanent Magnet Motor [46]	650	55
Double Rotor Permanent Magnet Machine [45]	480	72
Developed Prototype Generator	300-1250	80-84.6

To further reduce the effects of the cogging torque and hence to have a smoother machine operation, the slot openings were filled with bonded soft magnetic material with a relative permeability μ_r=10. The cogging torque of the filled slot openings machine were again computed and compared with the case of empty slot openings. The practical results show that the starting torque was reduced from about 64% to 43% of the rated torque. However, the machine was de-rated by about 5.4%.

The developed prototype machine is single phase where the good agreement between the theoretically predicted and laboratory test results, the relatively high efficiency and the typical 'rule of thumb' value of the leakage flux coefficient, which were achieved, demonstrate the success of the topology in its original design and the validity and correctness of the design methodology. Additionally, finite element analysis and theoretical study were carried out on two three-phase machines of the same topology. One of them is four-pole three-slot and the other is ten-pole six-slot.

Further research work on developing analytical methods for cogging torque estimation of this topology, predicting the load characteristics of trapezoidal (nonsinusoidal) voltage waveform machines, testing the developed machine as a motor and manufacturing the designed three-phase generators with skewed stator slots and/or rotor permanent magnets are suggested.

References

[1] Anon., Product description leaflets from the Enercon Company, Germany, 1994.

[2] J. M. D. Coey, "Rare-earth iron permanent magnets," Oxford, Clarendon Press, 1996.

[3] E. Spooner and A. Williamson, "Direct-coupled, permanent magnet generators for wind turbine applications," *IEE Proceeding of Electric Power Applications,* 1996, vol. 143, no. 1, pp. 1-8.

[4] A. Grauers, "Design of direct-driven permanent-magnet generators for wind turbines," Chalmers Univeresity of Technology, School of Electrical and Computing Engineering, Technical Report, no. 292, Göteborg, Sweden, 1996, 133p., Doctoral Thesis.

[5] A. Grauers, O. Carlson, E. Högberg, P. Lundmark, M. Johnsson and S. Svenning, "Test and evaluation of a 20 kW direct-driven permanent-magnet generator with frequency converter," *Proceedings of the European Wind Energy Conference (EWEC'97)*, Dublin, Ireland, 1997, pp. 686-689.

[6] E. Spooner, A. Williamson and G. Catto, "Modular design of permanent-magnet generators for wind turbine," *IEE proceedings of Electric Power Applications*, vol. 143, No. 5, September 1996.

[7] S. A. Papathanassiou, A. G. Kladas and M. P. Papadopoulos, "Direct-coupled permanent magnet wind turbine design considerations," *Proceedings of the European Wind Energy Conference (EWEC'99)*, Nice, France, 1999.

[8] P. Lampola, "Directly-driven, low-speed permanent-magnet generators for wind power applications," Laboratory of Electromechanics, Helsinki University of Technology, Finland, 2000, 62p. Doctoral Thesis.

[9] J. Chen, C. Nayar and L. Xu, "Design and finite-element analysis of an outer-rotor permanent-magnet generator for directly-coupled wind turbine applications," *Proceedings of the IEEE Trans. on Magnetics,* vol. 36, no. 5, September 2000, pp. 3802-3809.

[10] R. Hanitsch and D. Schulz, "Wind energy converters: some aspects of power quality and emissions," *International Scientific Conference*, Technical University of Gabrovo, Bulgaria, 20-21, November 2003, pp. 43-46.

[11] Q. Ronghai and A. Thomas, "Dual-rotor radial-flux toroidally wound permanent-magnet machines," *IEEE Trans. on Industrial Applications*, vol. 39, No. 6, November/December 2003, pp.1665-1673.

[12] R. Hanitsch and G. Korouji, "Design and constructing of a permanent magnet wind energy generator with a new topology," *KOMEL Conf.*, Poland, May 2004, pp. 63-66.

[13] L. Weissensteiner, "Electrical synchronous machine comprising a toroidal winding," Patent, WO 02/089291 A2, 2002.

[14] L. Soederlund and J-T. Eriksson, "A permanent-magnet generator for wind applications," *IEEE Trans. on Magnetics*, vol. 32, No. 4, pp.2389-2392, 1996.

[15] M. Stiebler and O. Okla, "A permanent-magnet toroid wind generator," *Proceedings of the International Conference on Electrical Machines (ICEM'92)*, Manchester, U.K., vol. 3, pp.1043-1047, 1992.

[16] E. Muljadi, C. P. Butterfield and Y-H. Wan, "Axial flux modular permanent-magnet generator with a toriodal winding for wind-turbine applications," *IEEE Trans. on Industrial Applications*, vol. 35, No. 4, pp. 831-836, 1999.

[17] H. Weh, "Transverse-flux machines in drive and generator applications," in *Proceedings of the IEE Symposium on Electric Power Engineering* (Stockholm Power Tech), Stockholm, Sweden, Invited Speakers's session, pp. 75-80, 1995.

[18] W. M. Arshad, T. Baeckstroem and C. Sadarangani, "Analytical design and analysis procedure for a transverse flux machine," *IEEE International Conference on Electric Machines and Drive 2001, (IEMDC'2001)*, pp. 115-121, 2001.

[19] F. Jacek, "Performance characteristics of a transverse flux generator," *IEEE International Conference on Electric Machines and Drives 2005, (IEMDC'2005),* pp. 1293-1299, May 15, 2005.

[20] E. Schmidt, "Design studies on transverse flux machines by using 3D finite element analysis," *6th International Symposium on Advanced Electromechanical Motion Systems (ELECTROMOTION 2005)*, Lausanne, Switzerland, September 27-29, 2005.

[21] W. Gribnau and J. Kursten, "Electrical flexibility versus mechanical complexity through direct conversion," *European Wind Energy Conf. (EWEC'91),* Amesterdam, Netherlands, Proceedings Part I, P.809-813, 14-18 October 1991.

[22] W. Deleroi, "Linear induction motor in generator use for windmills," *Symposium on Power Electronics Electrical Drives Advanced Electrical Motors (SPEEDAM)*, Positano, Italy, Proceedings pp.71-76, 19-21 May 1992.

[23] J. Hendershot and T. Miller, "Design of brushless permanent-magnet motors," Oxford, Clarendon Press, 1994.

[24] www.udri.udayton.edu/UDRI_Extranet/News/news0696.htr, UDRI News-June 1998–Magnetic Materials.

[25] R. P. Deodhar, D. A. Staton, T. M. Jahns and T. J. Miller, "Prediction of cogging torque using the flux-MMF diagram technique," *IEEE Trans. on Industry Applications*, vol. 32, no. 3, pp. 569-576, 1996.

[26] Z. Q. Zhu and D. Howe, "Analytical prediction of the cogging torque in radial-field permanent magnet brushless motors," *IEEE Trans. on Magntics.*, vol. 28, no. 2, pp.1371-1374, March, 1992.

[27] J. F. Gieras, "Analytical approach to cogging torque calculation of permanent magnet motors," *IEEE Trans. on Industry Applications*, vol. 40, no. 5, pp.1310-1316, September 2004.

[28] R. Hanitsch, R. Belmans, L. Walkoff and W. Geysen, "Brushless DC motor with air gap windings-influence of back iron material on motor efficiency," *in Prceedings IEE International Conference on Electric Machines and Drives (IEMDC' 91)*, pp. 126-130, 1991.

[29] T. Li and G. Slemon, "Reduction of cogging torque in permanent magnet motors," *IEEE Trans. on Magnetics.*, vol. 24, no. 6, pp. 2901-2903, Nov. 1988.

[30] A. Miraoui, L. De Fang and J. Kauffman, "Performance analysis of permanent magnet brushless DC motor", *in Proceedings IEE International Conference on Electric Machines & Drives (IEMDC' 93)*, Oxford, pp. 371-375, 1993.

[31] T. Ishikawa and G. Slemon, "A method of reducing ripple torque in permanent magnet motors without skewing," *IEEE Trans. Magnetics*, vol. 29, no. 2, pp. 2028-2031, Mar. 1993.

[32] J. De La Ree and N. Boules, "Torque production in permanent magnet synchronous machines," *IEEE Trans. on Industry Applications*, vol. 25, no. 1, pp. 107-112, Jan./Feb. 1989.

[33] R. Carlson, A. A. Trvares, J. P. Bastos and M. Lajoie-Mazenc, "Torque ripple attenuation in permanent magnet synchronous motors," *IEEE Conference on Industry Applications Society Annual Meeting*, pp. 57-62, vol. 1,1-5 Oct. 1989.

[34] M. Lajoie-Mazenc, B. Nogarede and J. C. Fagundes, "Analysis of torque ripple in electronically commutated permanent magnet machines and minimization methods," *in Proceedings on IEE International Conference on Electric Machines and Drives (IEMDC' 89)*, London , U.K., pp. 85-89, 1989.

[35] T. Sebastian and V. Gangla, "Analysis of induced EMF and torque waveforms in a brushless permanent magnet machine," *in Record of IEEE Industry Applications Society Annual Meeting*, Denver, pp. 240-246, 1994.

[36] M. Jug, J. Jiang, G. Chen, X. Wang, and K. Chau, "A novel poly-phase multi-pole square-wave permanent magnet motor drive for electric vehicles," *IEEE Trans. Industry Applications*, vol. 30, no. 5, pp. 1258-1266, Sept./Oct. 1994.

[37] M. Markovic, M. Jufer and Y. Perriard, "Reducing the cogging torque in brushless DC motors by using conformal mappings," *IEEE Trans. on Magnetics*, vol. 40, no. 2, March 2004, pp. 451-455.

[38] B. Ackermann, J.H.H. Janssen, R. Sottek and R.I. Van Steen, "New technique for reducing cogging torque in a class of brushless DC motors," *IEE Proceedings-B,* vol. 139, No. 4, July 1992, pp.315-320.

[39] S. Hwang and D. Lieu, "Design techniques for reduction of reluctance torque in brushless permanent magnet motors," *IEEE Trans. on Magnetics,* vol. 30, No. 6, November 1994, pp. 4287-4289.

[40] E.R.B. Filho and A.M.N. Lima, "Reducing cogging torque in interior permanent magnet machines without skewing," *IEEE Trans. on Magnetics,* vol. 34, No. 5, September 1998, pp.3652-3655.

[41] R. Richter, "Electrical Machines I," 2nd Eddition, Basel, Germany: Verlag Birkhäuser, 630 p, (in German).

[42] P. Lampola, J. Perho and J. Väänänen, "Analysis of a low-speed permanent-magnet wind generator," *European Union Wind Energy Conference (EUWEC'96)*, Göteborg, Sweden, Proceedings, 20-24 May 1996.

[43] D. G. Fink and J. M. Carroll, "Standard Handbook for Electrical Engineers," McGraw-Hill, 10th Eddition,1969.

[44] http://www.ibs-magnet.de

[45] G. Korouji, "Design, construction and test study of a wind energy generator with dual permanent magnet excitation," Ph.D. Thesis, Berlin University of Technology, Berlin, Germany, 2004 (in German).

[46] J. Chang, "Theoretical and experimental study of an electronic commutated DC motor with double cylinder rotor," Ph.D. Thesis, Berlin University of Technology, Berlin, Germany, 1984 (in German).

[47] http://www.ropatec.com

[48] M.A.Khan and P. Pillay, "Design of PM Wind Generator, Optimised for Energy Capture over a Wide Operating Range" *IEE International Conference on Electric Machines and Drives,* May 15, 2005, pp. 1501-1506.

Appendix A: Carter's Coefficient

The Carter's coefficient k_c of the following configuration:

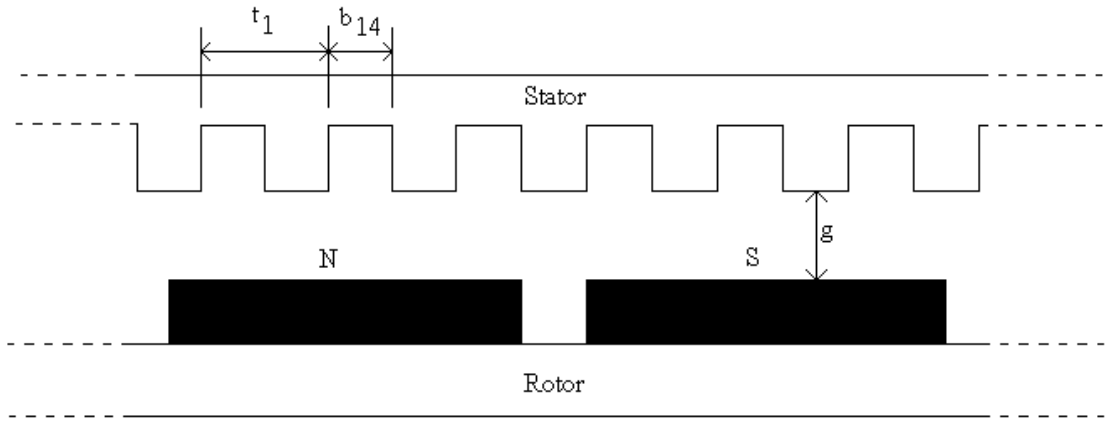

$$k_c = \frac{t_1}{t_1 - \gamma.g}$$

where

$$\gamma = \frac{4}{\pi}\left[\frac{b_{14}}{2g}\tan^{-1}\left(\frac{b_{14}}{2g}\right) - \ln\sqrt{1+\left(\frac{b_{14}}{2g}\right)^2}\right]$$

For the proposed topology, the Carter's coefficient parameters are considered as:

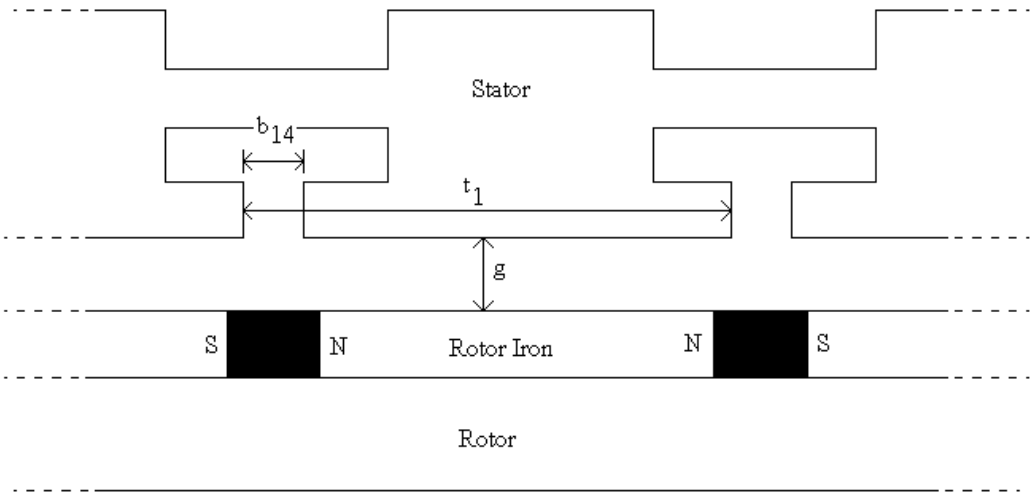

Appendix B: Experimental Set up

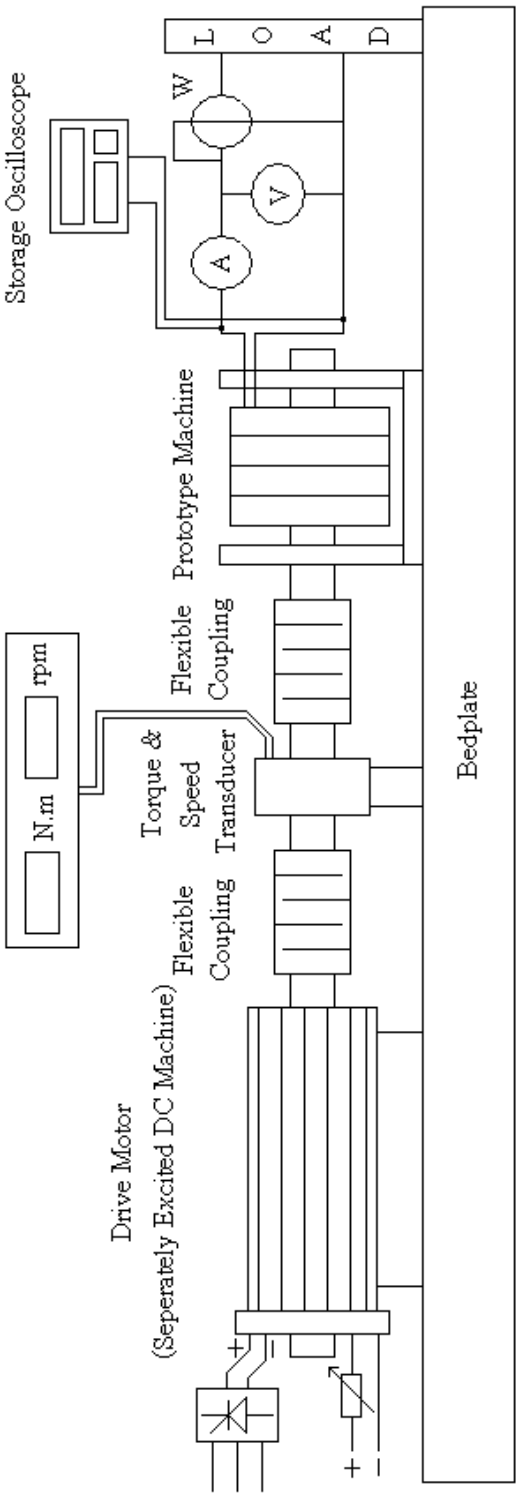

Figure B.1: Schematic of the test facility

Appendix C: Wind Energy Turbines

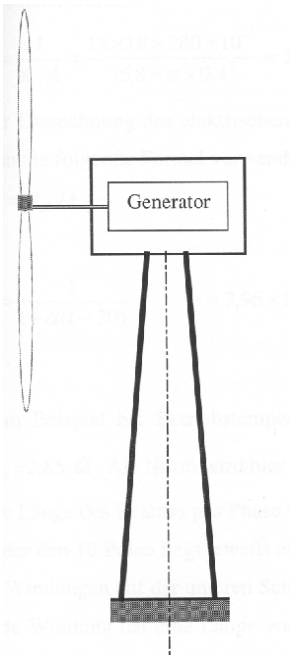

Horizontal wind energy system

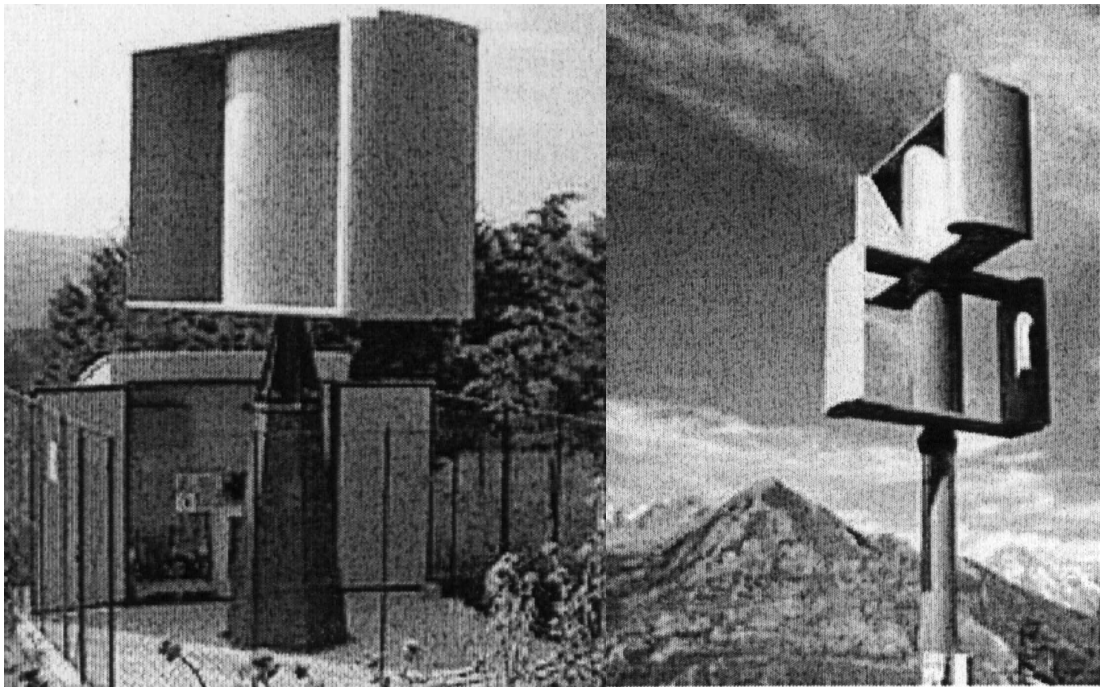

Vertical wind energy systems [47]

Shrouded rotor

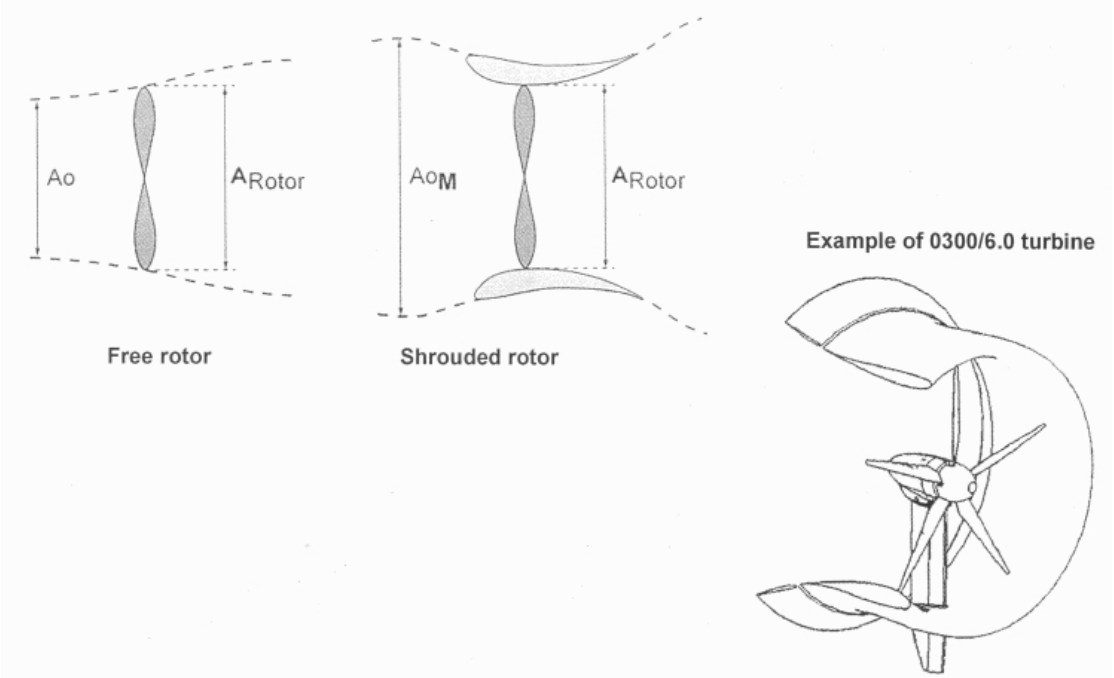

Free and Shrouded rotor